Applications of microfabrication in biosensor technology

A thesis for the degree of

Doctor of Philosophy

submitted to the Faculty of Engineering

University of Glasgow

by

Alun wyn Griffith

September 1996

ProQuest Number: 11007682

All rights reserved

INFORMATION TO ALL USERS
The quality of this reproduction is dependent upon the quality of the copy submitted.

In the unlikely event that the author did not send a complete manuscript
and there are missing pages, these will be noted. Also, if material had to be removed,
a note will indicate the deletion.

ProQuest 11007682

Published by ProQuest LLC (2018). Copyright of the Dissertation is held by the Author.

All rights reserved.
This work is protected against unauthorized copying under Title 17, United States Code
Microform Edition © ProQuest LLC.

ProQuest LLC.
789 East Eisenhower Parkway
P.O. Box 1346
Ann Arbor, MI 48106 – 1346

Zeii
10894
Copy 1

GLASGOW
UNIVERSITY
LIBRARY

to my mother

Something mysteriously deep and meaningful

Abstract

This thesis investigates the application of microfabrication techniques in biotechnology, embracing two major methodologies: biosensing and dielectrophoresis.

In the first instance, the miniaturisation of biosensors for use in aqueous solutions was explored, focusing on the issues of insulator deposition and metal multilayer adhesion. Two different immobilisation strategies were used. The first involved the binding of the electroactive protein, cytochrome *c*, to a self-assembled monolayer in order to measure the cellular production of superoxide. The second was the entrapment of an enzyme, glucose oxidase (EC 1.1.3.4), within a polypyrrole film as the core of an amperometric sensor for glucose. In the latter case, a novel analytical technique was developed for characterising the sensor interface involving the use of XPS and FTIR. The technique was used to demonstrate the efficiency with the which enzyme could be bound within the film, and indicated a non-linear relationship between the concentration of entrapped enzyme and the its concentration in the polymerisation solution.

To complement these studies, work in dielectrophoresis centred on methods for trapping and measuring single cell function within microfabricated electrode arrays. Although it was possible to hold a cell in close proximity to a biosensor array, difficulties concerning the sensitising of the electrochemical devices precluded measurements on single cells. However, by using a related technique it was possible, for the first time, to observe the dynamic activation of a single human neutrophil. The electrorotation technique was used to monitor changes in the physical character of the cell in order to identify the effects of chemotactic stimulation. Studies involving electrochemical and chemiluminescent measurements were performed to corroborate these findings.

Acknowledgements

My last words at our first meeting were; "Do you think you can sort out funding for a PhD in a month?". Well, he did, and this is it. It is Dr. Jon Cooper, my supervisor, that I must first thank for his resourcefulness, support and encouragement throughout my time at Glasgow University.

Now for the unacknowledged stars of the biolab: Bill Monaghan and Mary Robertson. Bill was a mine of information on microfabrication and Mary gave me invaluable training and advice on the cell culture work. The project work involved assistance and advice from a large number of technicians in the cleanrooms, dry etch, and in fact, most of the department, and I would like to take this opportunity to thank them all.

I would also like to thank: Pam Foreman, Dr. Hywel Morgan and Dr. Steffi Krause for their advice on thesis content; Andrew Gliddle for being seriously knowledgeable; John Young, Manus Maclean and many others in the Cell Biology department for their help with the neutrophil work; Philip Manning and Dr. Calum McNeil at Newcastle University for their help with the superoxide sensor; Chris Cotton, Paul Coyle, Jorg Papendick, Brendan Casey, Dr. Li Jiang, Dr. Li Li Ciu, Dr. Tom Flynn, Dr. Marcus Swann, Steffan Archer, Nick Green, Dr. Mike Hughes, Dr. Steve Britland, Dr. Simon Hicks, Dr. Karl Ryder, Dave Pritchard and Mary McGoldrick for their help, advice, drinks and good company.

To my family - my thanks for their support and encouragement; and finally, to Steph, for her love and tolerance, and for correcting my writing even when she would much rather be reading a good book.

Contents

1. Introduction

The rapid expansion of the biotechnology sector has generated significant cost reductions in the biological components of biosensors. Increasingly, microfabrication is regarded as another avenue to financial savings in biosensor manufacture. The sector is attempting to exploit the economies of scale and technological developments used so effectively in the electronics industry. Importantly, microfabrication can offer the possibility of dramatically increased functionality at little added cost. For example, in the use of 'on-chip' signal processing[1] and remote sensing/telemetry.[2]

The potential for exploiting the benefits offered by microfabrication is particularly apparent in the field of electrochemical biosensors. The basic electrochemical requirements, such as external connection and conductive tracking, are easily provided using standard microfabrication techniques. The increased performance offered by additional developments such as microelectrode arrays[3] and micromachining[4] present exciting opportunities for the future. Nonetheless, the successful integration of microfabrication techniques and electrochemical analysis using these novel sensor structures will present many new challenges.

This thesis addresses the issues associated with the fabrication and use of microfabricated biosensors. A variety of sensor arrays have been fabricated and investigated using a range of analytical techniques.

1.1 Biosensors

A biosensor is an analytical device which uses biomaterials to directly detect biological or chemical species without the need for complex signal processing. A more general definition would categorise a biosensor as a sensing device that contains a biological component. The key function of the biological component is to provide selectivity and sensitivity. The term biosensing encompasses a wide variety of sensing mechanisms including: electrochemical, acoustic, optical and immunological techniques. The biological component of a biosensor can take many forms. Enzymes and antibodies are commonly used, although other elements such as membranes, whole cells and the use of mammalian tissue have been reported in the literature.[5-7]

The majority of the work in this thesis has concentrated on the use of amperometric biosensors and their basic function is described in figure 1.1. Signal transduction is accomplished by the use of mediators which are small electroactive molecules that shuttle electrons between the biological component and the electrode. An important consideration, omitted from figure 1.1, is the mechanism by which the sensor components are fixed relative to the electrode. For example, the components can be held by a covalent bond to the electrode surface,[8] entrapped in a polymer matrix,[9] mixed into a dried layer,[10] or enclosed by a membrane.[11] The nature of the matrix will have a dramatic effect on the characteristics and performance of the biosensor.

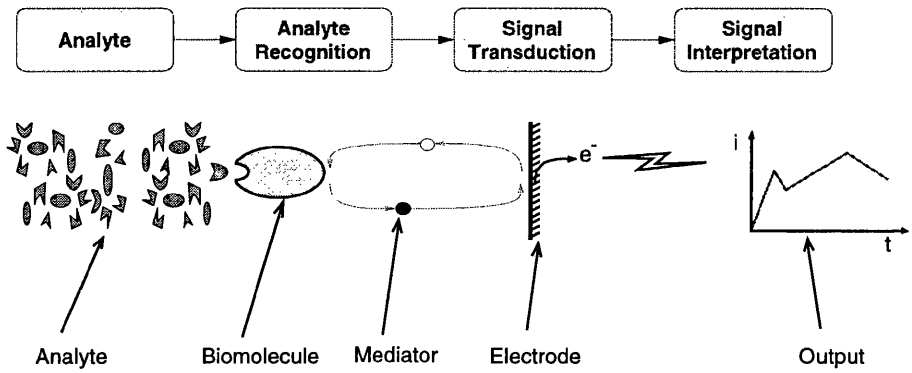

Figure 1.1: A schematic diagram illustrating the operation of an amperometric biosensor.

1.2 Biosensor Fabrication

The commercial manufacture of biosensors exploits a wide range of techniques. Many are based upon techniques modified from those developed within the electronics industry, for example, screen printing, lithographic methods and silicon micromachining. However, some have been developed specifically for biosensors, for example, the biomaterial spray-deposition unit marketed by Biospot Inc. and novel large-scale manufacturing methods for enzyme-linked immunosorbent assays (ELISA).[12]

Factors such as biocompatability and stability in aqueous solution are issues specific to biosensor design and fabrication. For example, the mediator ferrocene has been used for 'in vitro' glucose biosensors, however, this mediator could present a toxic hazard for 'in vivo' applications. The issue directly addressed in this thesis was the reliability of microbiosensors in aqueous media. Figure 2.2 in chapter 2 shows a sample of the microfabricated biosensors developed during the project. The devices were all designed for electrochemical sensing and were fabricated on inert substrates using lithographic techniques. The planar nature of the devices necessitates the use of insulating layers to define active electrode area. The adhesion of the component layers is a crucial factor in sensor reliability and performance.

1.3 Biosensors Investigated in the Project

Investigations of superoxide and glucose biosensors formed the core of the experimental work and are described in detail in chapters 3 and 5. The sensors were fabricated using different immobilisation techniques, these provide illustrations of the range of methods available for the microfabrication of biosensors.

1.3.1 Superoxide Biosensor

The superoxide free radical (O_2^-) has been shown to have a principal role as a bacterial killing agent in the mammalian immune defence system[13] and is strongly implicated in the pathology of rheumatoid arthritis.[14] In addition, research has been conducted on its activity in various cancers[15] and recently novel work has been conducted into its role in cell signalling.[16,17] An initial target for the project was the development of a microfabricated sensor for the measurement of superoxide release from a single human neutrophil. The superoxide radical has a short lifetime in aqueous media and the ability to measure its release close to the cell would provide valuable data on both the mechanism of release and the nature of its activity.

The concept of the microfabricated superoxide biosensor is demonstrated in figure 1.2. The electrode array has two separate elements. The four outer (circular) electrodes exploit the phenomenon of dielectrophoresis (see section 4.3.2) to generate a force that directs the particle (in this case, a polystyrene bead) towards the centre of the electrode array. The central ring electrodes surrounding the particle can be activated in order to detect the release of superoxide. By the use of multiple ring electrodes, measurements at an increasing radius from the superoxide source could permit the accurate determination of parameters such as diffusion and dismutation rates.

Superoxide can be measured using a variety of techniques, such as: luminol chemiluminescence,[18] nitroblue tetrazolium reduction,[19] EPR spin-trapping[20] and spectrometric measurement of the reduction of the protein cytochrome *c*.[21] Whilst these methods are well characterised, they remain limited to macroscopic applications and cannot be used in the analysis of the release of superoxide from single cells. The use of an electrochemical method in combination with precise control of cell position can potentially overcome this limitation. The principle of the electrochemical detection of superoxide is outlined in figure 1.3.

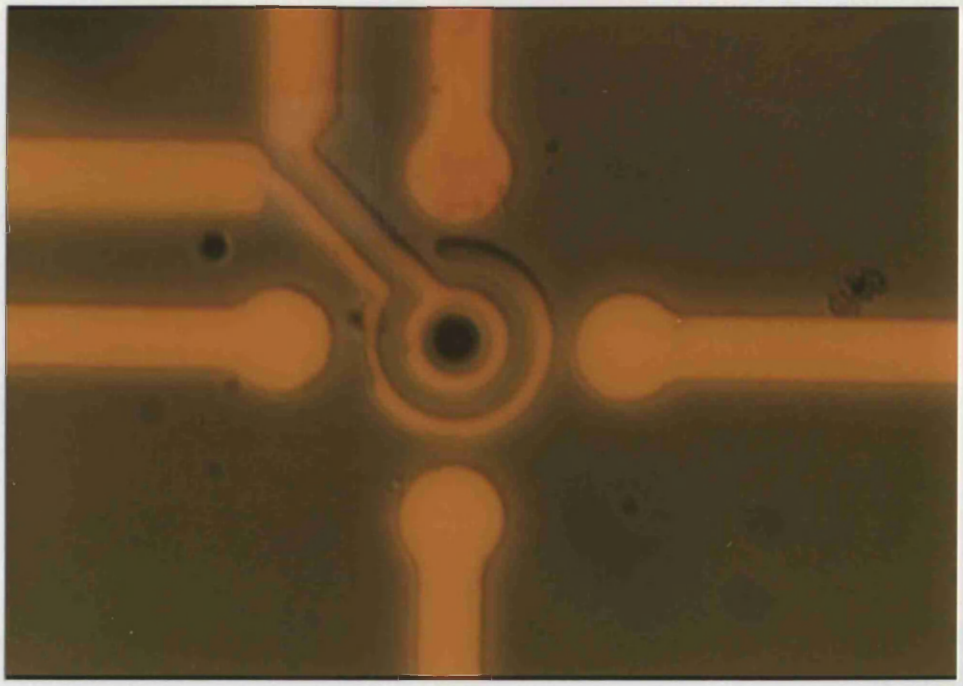

Figure 1.2: A microfabricated sensor array that demonstrates the principle of detecting the release of superoxide from a single cell. The disc electrode separation is 40μm.

The detection of superoxide ions is achieved using the direct electron transfer reaction of covalently immobilised cytochrome *c*:

$$cytochrome\ c\ (III) + O_2^- \rightarrow cytochrome\ c\ (II) + O_2 \quad \text{(cytochrome } c \text{ reduction)} \qquad (1.1)$$

$$cytochrome\ c\ (II) \xrightarrow{Modified\ Electrode} cytochrome\ c\ (III) + e^- \quad \text{(cytochrome } c \text{ oxidation)} \qquad (1.2)$$

The main competing reaction in aqueous solution is the dismutation of superoxide according to the following reaction

$$O_2^- + O_2^- \xrightarrow{2H^+} H_2O_2 + O_2 \qquad (1.3)$$

The cytochrome *c* that is reduced by superoxide is re-oxidised by maintaining a working electrode at potential of +100mV (*vs.* Ag/AgCl).[22] The quality of the immobilisation (and hence oxidising current measured) is highly dependent on immobilisation method and the nature of the gold surface. Developing an efficient electrochemical couple for detecting the superoxide ion on a microfabricated electrode was one of the most challenging aspects of the project.

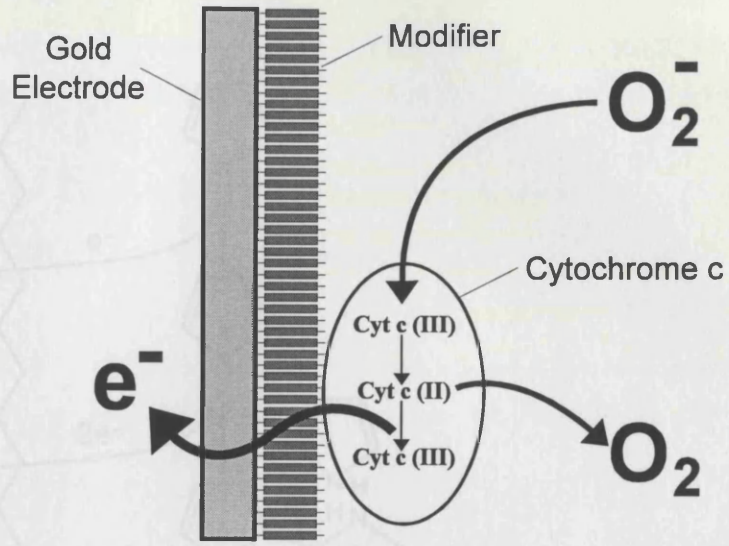

Figure 1.3: An electrochemical superoxide sensor. The operation is based upon the reduction of the cytochrome *c* protein immobilised at a modified gold electrode. The subsequent re-oxidation of the cytochrome *c* generates an electrical current related to the concentration of superoxide in solution.

1.3.2 Glucose Biosensor

The glucose biosensor has received much attention since the principle of an enzyme-electrode was first described by Clark and Lyons in 1962.[23] The basic sensing element is based on the oxidation of the hydrogen peroxide at *ca.* +0.65V (*vs.* Ag/AgCl) produced as a product of the reaction of the glucose oxidase (GOx) with the glucose substrate.[24]

Much of the subsequent work focused on the optimisation of the sensor for use in whole blood and *in vitro* measurements. The major problems encountered include: biocompatability, durability, oxygen sensitivity and the elimination of interferent effects. Numerous approaches have been investigated such as the use of polymer films, membrane coatings and mediators. For example, the use of cellulose acetate film provides a good biocompatible surface which can also minimises the effects of specific electrochemical interferents. Mediators such a ferrocene or ferricyanide allow the assay potential to be lowered, further reducing the current contribution from interferents.

Progressing from the early "enzyme sandwich" methodology of Clark and Lyons, much work has been conducted into novel methods of enzyme entrapment. It is desirable to achieve maximal enzyme loading as close as possible to the electrochemical surface. This reduces diffusional loses and maximises the current response. The function of some commercially available screen-printed glucose sensors is based on the crude, but effective, immobilisation of GOx in a carbon

paste, in contrast, much recent academic work has concentrated on enzyme entrapment in polymers.

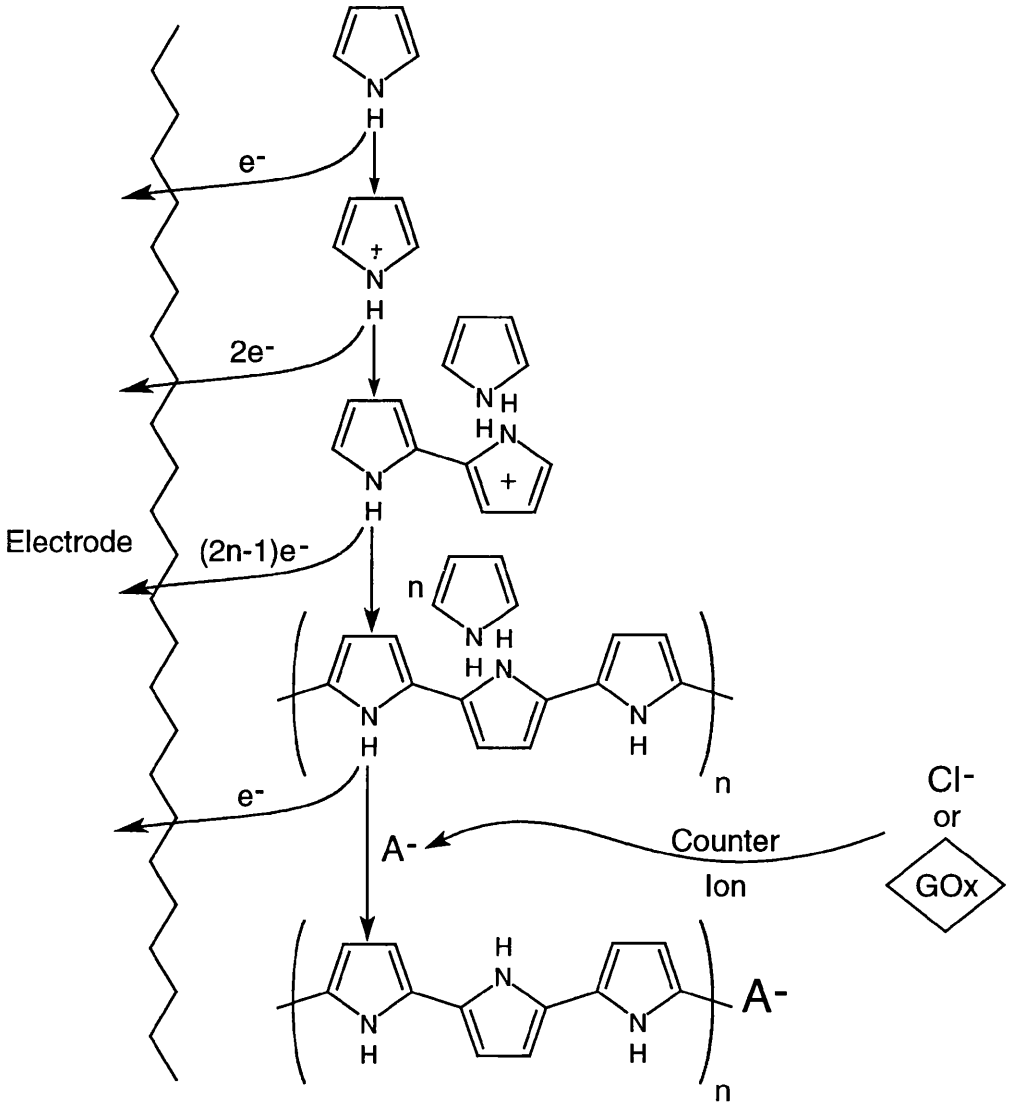

Figure 1.4: The entrapment of enzyme by the electrolytic oxidation of the pyrrole monomer. *Modified from Hall.*[12]

Successful entrapment of GOx within a variety of polymer films is classically demonstrated using an electrochemical assay. However, determination of the amount of active enzyme in the film requires a more complex analysis. The work on glucose biosensors presented in this thesis has concentrated on the physical characterisation of the biosensor interface, with the aim of characterising the distribution of enzyme within the film. An original technique has been developed based on the determination of the relative ratios of enzyme to binding matrix. The model system employed was a polypyrrole (PPy)/GOx based sensor, the enzyme being entrapped within the polymer matrix during its electropolymerisation in an aqueous solution of monomer and enzyme (figure 1.4).

The catalytic oxidation of glucose is a two stage compulsory ordered mechanism. First, glucose reacts with the enzyme, followed by the oxidation of the flavin adenine dinucleotide (FAD) redox centre by dissolved molecular oxygen, as shown below (equations 1.4 and 1.5):

$$GOx_{(FAD)} + \beta\text{-D-Glucose} \rightarrow GOx_{(FADH_2)} + \text{D-Gluconolactone} \quad (1.4)$$

$$GOx_{(FADH_2)} + O_2 \rightarrow GOx_{(FAD)} + H_2O_2 \quad (1.5)$$

Mediators compete with the molecular oxygen reaction, but when they are not used, the H_2O_2 generated provides an intrinsic mediator that can be oxidised at the electrode surface (equation 1.6):

$$H_2O_2 \rightarrow O_2 + 2H^+ + 2e^- \quad (1.6)$$

Keilin and Hartree[25] demonstrated that GOx is highly specific for the β-anomer of glucose. The other product, gluconolactone, is a weak competitive inhibitor which rapidly hydrolyses to gluconic acid.

When the polymer film is thin, it can be assumed that there is no substrate concentration polarisation within the film,[26] and the electrochemical response can be analysed accordingly, using a simple mathematical model. The original motivation for this research was to try to determine total enzyme concentration (e_Σ) at the biosensor interface, as used in the expression below (equation 1.7):

$$\frac{nFA\alpha}{i_{obs}} = \frac{K_M}{k_{cat}K_s s_\infty e_\Sigma l} + \frac{1}{k_{cat}e_\Sigma l} + \frac{1}{kK_A a_\infty e_\Sigma l} \quad (1.7)$$

For the example where GOx is entrapped in a polymer film, the terms used in this model represent the following: i_{obs} is the current response, n is the number of electrons transferred (two), F is the Faraday constant, A is the area of the electrode, and l is the thickness of the polymer film. K_M and k_{cat} are the enzyme kinetic parameters and k is the rate constant for the reaction of dioxygen with GOx. K_A and K_S are the partition coefficients into the polymer film for oxygen and glucose, respectively - with a_∞, and s_∞ representing the bulk concentrations. The parameter α describes the balance between the detection of H_2O_2 at the electrode surface and its loss to the bulk solution, previously it has been estimated as 0.5.[26,27]

Of the variables used in this model, the terms for l and e_Σ are determined by the polymerisation conditions chosen during biosensor construction. So, for example, at a given film thickness, it would *seem* to be possible to vary e_Σ at the biosensor surface by altering the ratio of enzyme to monomer in solution prior to polymerisation. To date, however, it has not been possible to measure e_Σ. It has therefore only been practicable to infer that the concentration in the film has changed by measuring the sensor's response and correlating this to the polymerisation conditions (pre-supposing that all of the enzyme present is equally active). As a consequence, further detailed kinetic analysis of enzyme-polymer films using equation 1.7 has proved difficult.

Of the many of the interfacial techniques available in biosensor surface characterisation (e.g. ellipsometry,[28] surface plasmon resonance[29] or quartz crystal microbalance[30]), none can be readily used to measure e_Σ, as they do not apportion the relative amounts of polymer and protein. Two studies based upon labelled enzymes have attempted to determine e_Σ entrapped in non-conducting polymers. In the first instance, Bartlett *et al.* have used "*hot*" GOx entrapped in poly(N-methylpyrrole) to show, through competition studies, that different amounts of enzyme can be entrapped in films under different polymerisation conditions.[27] More recently, Wang *et al.* have entrapped fluorescently labelled proteins in non-conducting polymers and have measured intensity as a function of distribution at the electrode surface.[31] However, in the latter case, if the enzyme is not orientated within the film there may be quenching of the fluoroprobe at the metal electrode.

In this project, X-ray photoelectron spectroscopy (XPS) was used to provide elemental analysis and quantification of the enzyme concentration at the interface of the polymer film. Electrochemical assays were performed in parallel to assess the response of the active enzyme in the film. Further parallel studies using Fourier transform infra-red (FTIR) spectroscopy were performed as a bulk sensitive means of monitoring the total enzyme concentration throughout the thickness of the biosensor film.

1.4 Dielectrophoresis

The phenomenon of dielectrophoresis was used in this project for positioning and rotating micrometer-sized particles. The applications of dielectrophoresis included: cell sorting and guidance,[32,33] the measurement of fundamental electrical properties of cells,[34,35] the creation of bio-repellent surfaces[36] and the analysis of bacterial contamination.[37] The fundamental advantage of dielectrophoresis is the non-invasive manner by which it exploits subtle electrical differences to discriminate between similar particles, without the need for chemical modification or labelling. Microfabrication is ideally suited to the manufacture of a variety of

electrode geometries required for the generation of the non-uniform electric fields necessary for dielectrophoretic particle manipulation.

The name dielectrophoresis was coined by Pohl[38] - the first person to investigate the phenomenon in depth. He defined it as the motion imparted to a polarisable (but electrically neutral) particle when subjected to a non-uniform electric field. In a uniform electric field a neutral particle will experience no net force due to its polarisation (figure 1.5a). However, when the same particle is placed in a non-uniform field (figure 1.5b), the regions of greater electric field strength induce a differential force acting on the opposite sides of the particle. This results in a net translational force. The direction of the force depends on the relative polarisabilities of the particle and the medium. If the particle is of greater relative polarisability, the net force will be directed towards the region of greatest field strength (the 'pin' electrode), and the motion is termed 'positive dielectrophoresis'. In contrast, a lesser polarisability will result in a net force away from pin electrode, and is termed 'negative dielectrophoresis'.

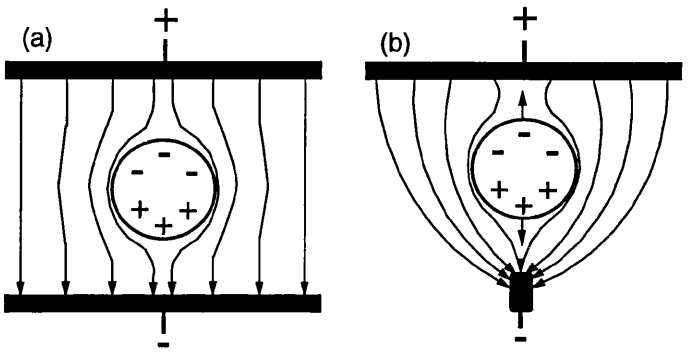

Figure 1.5: A particle being polarised in a uniform (a) and a non-uniform (b) electric field. It is only in the non-uniform field that there can be is a resultant translational force acting on the particle. The direction of the force can be either towards or away from the pin electrode.

The relative polarisabilities of the particle and the medium are frequency dependent. Their ratio influences the nature of the dielectrophoretic response. Hence, under certain conditions, the generation of translational and rotational dielectrophoretic forces can be controlled by the appropriate selection of experimental parameters. The ability to adjust the forces acting on particles by variation of frequency, applied field and suspension medium provides the basis for the majority of applications exploiting the phenomenon of dielectrophoresis.

1.4.1 Particle Positioning

The non-uniform electric fields were generated using planar electrode arrays fabricated using photolithography. The experimental conditions were adjusted to generate a negative dielectrophoretic force in order to move the particles into an electric field minimum created at the centre of the electrode array (figure 1.6). This method of particle positioning proved to be

both convenient and accurate and has been previously demonstrated in figure 1.2. Little particle pre-treatment was required and positional tolerances reflected the precision of photolithographic process.

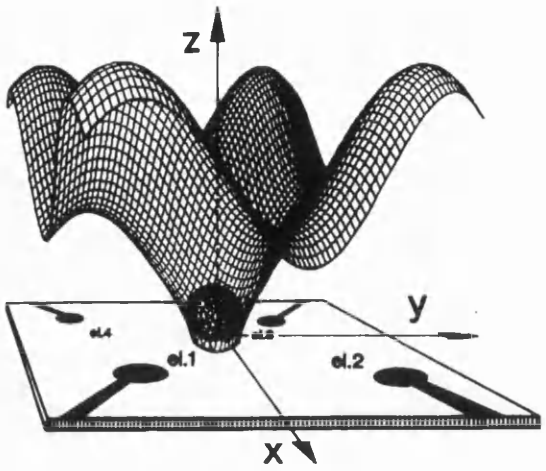

Figure 1.6: A simulated quadropole electric field trap for a single particle. The parameters have been set to model the experimental conditions necessary for negative dielectrophoresis. Particles initially within the 'funnel' of the electric field will eventually come to rest at the field minimum located at the centre of the electrode array. *Reproduced from the work of* Fuhr *et al.*[39]

The use of dielectrophoresis provides an excellent method for particle confinement and will readily indicate dramatic differences in cellular properties. An excellent example is the measurement of the differences in membrane conductivity between live and dead yeast cells.[40]

1.4.2 Electrorotation

Electrorotation occurs as a result of the induced torque exerted on particles in rotating electric fields. The use of the technique has gained recent popularity as a means of observing more subtle changes in both external and internal cellular properties. For example, physiological changes in oocytes[41] upon fertilisation.

In this study, electrorotation was also used to analyse the changes in the electrical properties of human neutrophils upon activation by chemotactic reagents. Neutrophils are cells in the bloodstream that play a crucial role in the function of the immune system. They are responsible for processes such as phagocytosis[42] and free radical release.[43,44] Upon activation, the cells undergo rapid physiological changes as part of the 'respiratory burst'.[45] The changes were characterised by the variation in the electrorotational response of individual cells.

1.5 Thesis Structure

The work has been sub-divided into four main chapters, these are: microfabrication, microbiosensors, dielectrophoresis and biosensor interfaces. Due to the scope of the work and

the range of techniques, 'methods' and 'theory' sections have not been given separate chapters but immediately precede the work for which they were employed.

Chapter 2 provides a summary of the microfabrication techniques developed during the project, and elaborates upon the issues specific to the manufacture of reliable multilayer sensor structures.

Chapter 3 describes the range of electrochemical techniques used in the project and concentrates on the preparation and performance of the cytochrome *c* based superoxide biosensor. In addition, there is the description of the use of chemiluminescence as a companion technique for superoxide detection.

Chapter 4 is concerned with the use of dielectrophoresis for particle positioning and rotation. The dielectrophoretic properties of human neutrophils are investigated and physical changes in the cell wall during chemotactic stimulation are identified and discussed.

Chapter 5 presents the analysis of the interface of a PPy/GOx glucose biosensor using amperometry, FTIR and XPS. The three techniques are used in parallel to determine the activity and relative ratios of polymer and enzyme in the sensor matrix.

The conclusions and recommendations for further work are found in Chapter 6. References, appendices and a list of abbreviations appears at the end of the thesis.

2. Microfabrication

This chapter provides a brief summary of the fabrication methods used in this project. The results presented provide a detailed analysis of the dominant issues identified in the successful manufacture of microfabricated biosensors. The particular focus is on the development of durable microbiosensors, hence factors such as metallisation and insulator adhesion have been investigated in greater depth.

2.1 Methods & Materials: Microfabrication

The basic lithographic process for the fabrication of an insulated planar electrode structure is shown in figure 2.1. Both photolithography and electron-beam (e-beam) lithography were used during the course of the project; the practical resolution limit of photolithography is 2μm, for smaller features e-beam lithography was necessary. When a choice was available, the photolithographic process was the preferred fabrication method since it has a higher yield and a shorter turnaround time. Etch depths and resist/insulator thickness were determined using a Dektak ST^3 (Veeco Instruments Inc.) surface profiler

2.1.1 Substrate Cleaning

All the work presented in this thesis was performed on either glass or polished quartz substrates. The standard cleaning procedure is as follows:

1) Sonicate the substrate for 20 min in Decon 90 (Decon Labs Ltd.), mixed in a 1:1 ratio with reverse osmosis (RO) water.
2) Thoroughly rinse in RO water.
3) Sonicate the substrate in RO water for 10 min.
4) Blow dry using nitrogen.

If the substrates are visibly coated with contamination, step 1 (above) should be preceded by a 10 minute sonication in Opticlear(G&S Inc.). Any residual resist remaining from previous lithographic steps is best removed by sonication in acetone, again, if required, this should precede step 1 in the above procedure.

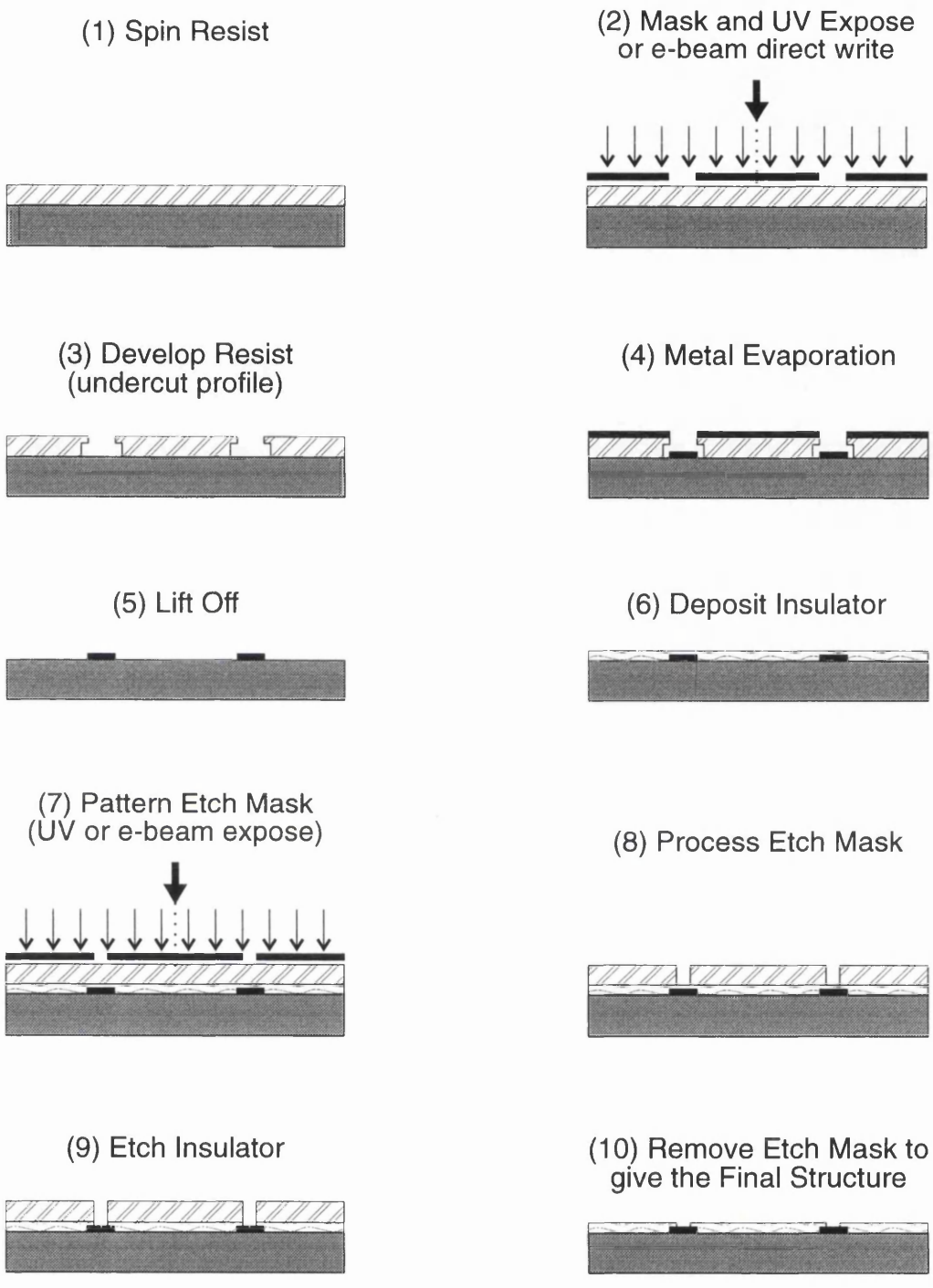

Figure 2.1: The fabrication sequence for an insulated electrode structure manufactured using either photo and/or e-beam lithography.

2.1.2 Photolithography

The standard photoresist used in the project was S1818 (Shipley Inc.). It was purified by filtering through a 0.25μm particle filter. Spinning parameters of 4000rpm for 30s produce a resist layer of *ca.* 1.85μm thickness. Spin speed is the dominant parameter that controls resist thickness, spin time has a less significant effect. It is important to fully coat the upper surface of the substrate with resist before spinning. A slightly thicker rim of resist will always form at the edges of the substrate, hence for reproducible lithography the pattern should be placed in the central portion of the substrate. For the very smallest features (close to the practical limit of 2μm) a thinner resist layer is recommended. Thin resist coverage can be achieved using faster spin speeds or a low viscosity resist such as Shipley '1400-17' (*ca.* 0.45μm thick spun at 4000rpm for 30s). The full photolithographic procedure is as follows:

1) Spin S1818 resist (typically 4000rpm, 30s; to give a thickness of *ca.* 1.85μm).
2) Bake for 15 min at 90°C.
3) Soak in chlorobenzene for 10 min.
4) Blow dry and bake at 90°C for a further 15 min.
5) UV Expose for 14s (Hybrid Technology mask aligner, 32J cm^{-2}, 364nm)
6) Develop in Microposit developer (1:1 mix with RO water) for *ca.* 80s.
7) Wash in RO water and blow dry.

The undercut resist profile desirable for an effective lift-off step (see section 2.1.4) is illustrated in figure 2.1 (step 3). If this profile is not required step 3 above can be omitted and the resist should be baked for 30 min. The chlorobenzene soak[46] hardens the upper portion of the resist causing it to develop at a slower rate, thus allowing an undercut resist profile to be formed.

2.1.3 E-Beam Lithography

The majority of e-beam lithography requires a bi-layer resist structure. This is created by the spinning of two separate layers of resist of different sensitivity to e-beam exposure. The resists are made by dissolving poly(methyl methacrylate) (PMMA) in o-xylene. The upper layer is a higher molecular weight (MM > 400,000) version of the polymer, which when exposed to an e-beam is degraded at a slower rate that the low molecular weight variety (MM *ca.* 90,000). As a result, it will develop at a slower rate. As for the chlorobenzene soak procedure described in section 2.1.2, the resultant undercut profile is tailored for use in the metal lift-off process. The full procedure is as follows:

1) Spin lower molecular weight resist (5000rpm, 60s are typical spinning parameters).
2) Bake at 180°C for 60 min.

3) Spin higher molecular weight resist (5000rpm, 60s).

4) Bake at 180°C for 120 min.

5) Evaporate a 50nm layer of Cr onto the sample (necessary for charge dissipation).

6) E-beam expose (Leica EBPG-5, HR).

7) Remove the Cr layer using a wet etch (see section 2.1.5.1.1).

8)Develop in methyl isobutyl ketone (MIBK)/isopropyl alcohol (IPA) solution for *ca.* 35s.

9) Wash in RO water and blow dry.

The higher the concentration of dissolved polymer, the more viscous the resist layers produced. High resolution patterns require thinner layers of resist. The ratio of MIBK:IPA required for resist development (step 8 above) is determined by the thickness of the bi-layer resist structure.

2.1.4 Metal Evaporation and Lift-Off

The majority of metal evaporation in this project was performed on the Plasyss QD1 automated e-beam evaporation system. The low pressure ($3x10^{-7}$Torr) and reduced chamber contamination of this system are important factors in guaranteeing both the quality and reproducibility of the resultant metal layer. The most common metal layer used was Ti/Pd/Au (10/10/100nm) although solitary layers of Ti and Cr were required at certain stages of the fabrication procedure.

The lift-off procedure is performed following metal evaporation and involves the dissolving of the resist pattern in acetone to leave the metal in the regions defined by the lithographic process. An undercut profile is necessary to provide a good break between the metal layer deposited on the resist and the layer deposited on the substrate (see figure 2.1, step 4-5). Poor lift-off can be caused by a non-ideal resist profile and will result in rough electrode edges and short-circuits between closely spaced features. It is important to carefully wash the substrate as it is removed from the lift-off solution so as to ensure that none of the metal particle re-adhere to the substrate.

2.1.4.1 Gold Metallisation

Work was performed on the deposition of gold electrodes, i.e. without the need for a Ti/Cr based underlayer.[47,48] This procedure required the deposition of a [3-mercaptopropyl] trimethoxysilane (MPS) underlayer prior to metallisation. The procedure used is as follows:

1) Clean the substrates

2) In a fume hood, reflux the substrate in a solution of 400ml IPA, 10ml RO water and 10g MPS.

3) Wash the substrates in IPA and blow dry in nitrogen.

4) Bake at 105°C for 10 min.

5) Repeat steps 2-4 above a total of three times.

2.1.5 Electrode Insulation

Insulating layers on planar structures can be created by the deposition of an insulator followed by its patterning using either wet or dry etch techniques. The two insulators investigated were polyimide and silicon nitride. Manual insulation of large features (e.g. contact wires) was performed using silicone adhesive (Dow Corning, RTV 3140) or epoxy adhesive.

2.1.5.1 Polyimide

The standard procedure for the deposition and patterning of polyimide (Hitachi, PIQ 13) is as follows:

1) Clean the substrates.

2) Spin PIQ 13 primer layer at 5000rpm for 30s.

3) Bake at 350°C for 30 min.

4) Spin on PIQ 13 polyimide, typical film thickness was 1.35μm (5000rpm, 30s).

5) Bake at 350°C in a N_2 atmosphere for 60 min.

6) Spin resist layer and pattern (see section 2.1.2).

6) Evaporate a 30nm layer of Ti or Cr as the etch mask.

7) Perform lift-off to provide a photo-negative mask.

8) Reactive ion etch (RIE) etch the polyimide in O_2/CF_4 (see section 2.2.2.1.1).

9) Remove the etch mask using a wet etch (see section 2.1.5.1.1).

2.1.5.1.1 Titanium and Chromium Wet Etching

The Ti etch is composed of 0.1M ethylenediamine tetraacetic acid (EDTA) dissolved 30% H_2O_2 solution.[49] The etch should be stored in the refrigerator when not in use, it will maintain a consistent etch rate for about one week. The etch is highly specific for Ti (at least 20 times faster than with Ni or Cr) and the etch rate is 10nm min^{-1}.

The Cr etch (100ml) is made from 3.5ml glacial acetic, and 20g ammonium ceric nitrate dissolved in 100ml of RO water. The etch rate is *ca.* 20nm min^{-1} and the etch will last for up to three months when stored at room temperature.

2.1.5.2 Silicon Nitride

The procedure for patterning of silicon nitride deposited by plasma enhanced chemical vapour deposition (PECVD) is as follows:

1) Clean the substrates.

2) Deposit silicon nitride using an Oxford Plasma Technology μP-80, the routine deposition rate is *ca.* 10nm min^{-1}.

3) Spin resist layer and pattern (see section 2.1.2), the etch mask is a photo-positive.

4) RIE etch the silicon nitride in C_2F_6 (see section 2.2.2.1.2), the standard etch rate is 50nm min^{-1} at 100W (Oxford Plasma Technology BP-80, 30sccm flow rate, 10mT).

5) Remove residual etch mask using acetone.

2.2 Results and Discussion

In this section, aspects of microbiosensor metallisation and insulator patterning will be discussed. Effective metallisation of sensor structures must satisfy a number of requirements such as: adhesion, durability and electrochemical stability. The work also addresses the issues of gold metallisation and the fabrication of multilayer structures. Polyimide and silicon nitride were the insulators used in the project, and results are presented on the influence of factors such as adhesion, etching method and insulator integrity. Samples of the sensor structures fabricated using the range of techniques described in this chapter are shown in figure 2.2.

2.2.1 Sensor Metallisation

The main goal of the work on sensor metallisation was the formation of an electrochemically stable and adherent structure. The need for a gold electrochemical surface presented the first limiting factor since evaporated gold alone does not adhere well to the majority of substrates. Limited success has been observed by gold evaporation onto heated mica,[50] however, in general, an underlayer of Ti or Cr is necessary to promote gold adhesion.

Due to the need for an underlayer, most sensor structures were fabricated using a recipe of first 10nm Ti followed by 100nm gold. Providing the evaporation was performed at low pressure in a low contamination chamber (an advantage afforded by the automated Plasyss evaporation system), the adhesion of the metal film using this recipe was good. The adhesion was tested using the 'Scotch' tape test. While this metallisation method was suitable for most electrochemical experiments conducted at low positive potentials, the Ti/Au structure demonstrated poor long term stability at voltages >0.9V (*vs.* Ag/AgCl) necessary for procedures such as acid cycling (see section 3.1.3.1.1) and polymer oxidation (see section 5.1). The failure mechanism was the de-lamination of the metal layer due to the oxidation of the Ti underlayer.

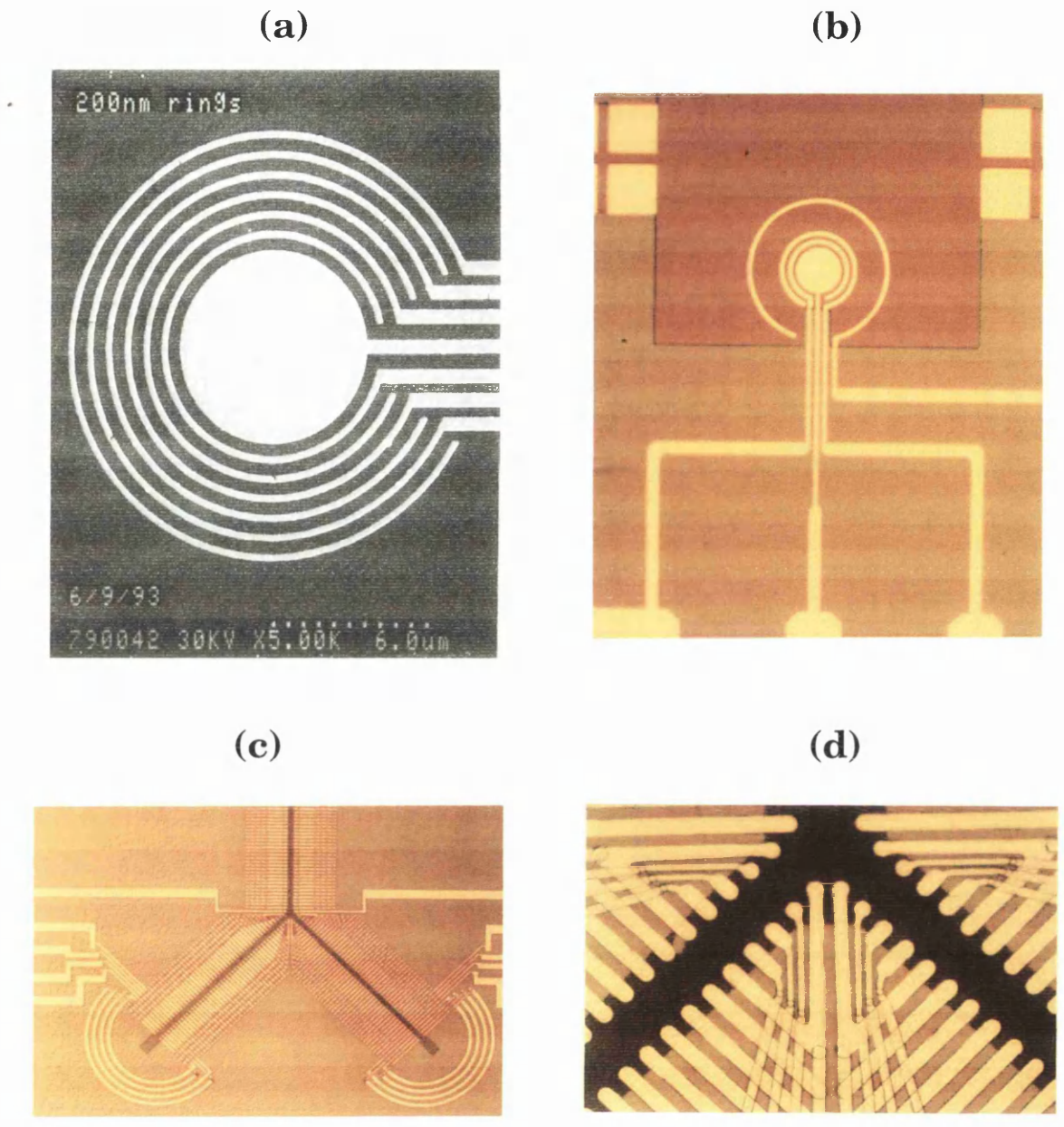

Figure 2.2: Samples of the microfabricated electrode structures produced during the course of the project. (a) A ring array fabricated using e-beam lithography (200nm wide rings). (b) A ring electrode array fabricated using photolithography, (10μm wide rings); the insulator has been patterned so as to only cover the tracking to the array. The 'Y-shaped' TWD electrode structure (c). The electrode has three channels and can be used for cell sorting applications (see section 4.4.1); The individual gold finger electrodes are 120nm tall, 10μm wide and on a 10μm pitch, there is a 50μm gap across the channel. The close-up photograph (d) highlights the thru-holes etched in the silicon nitride insulator (200nm thick).

In an attempt to improve the stability of the metallisation, a Pd intermediary layer (10nm) was introduced between the Ti and the Au following the method of Lambrechets *et al.*[1] This method was successful, and the electrode structure provided a stable electrochemical response during repetitive cycling for up to 60 min in 1M $HClO_4$ (100mV s^{-1}, 0 to +1.5V *vs.* Ag/AgCl). The precise mechanism by which the Pd improves the stability of Ti/Pd/Au structure is not clear, although according to Sharp[51] the Pd forms an diffusion barrier to oxygen that reduces the rate of underlayer oxidation. An additional benefit gained from the use of the Pd layer is the minimisation of the undesirable electrochemical currents caused by Ti or Cr diffusion along grain boundaries to the surface of the gold layer.[48]

2.2.1.1 Gold Metallisation

Exploratory work was performed on the use of the method of Goss *et al.*[52] to form an gold-only metallisation layer to eliminate any potential effects from underlayer metal contamination. The procedure relied on the use of MPS, which contains siloxane and thiol terminating groups. The siloxane group bonds to the glass/quartz substrate and the thiol group bonds to the evaporated gold layer. The procedure was very successful, and while a quantitative measurement of adhesion could not be made, due to the lack of suitable equipment, the metallisation did survive the benchmark 'Scotch' tape test.

It was not necessary to immediately evaporate the gold layer, and excellent adhesion was achieved on substrates metallised within three days of formation of the MPS adhesion layer (samples were kept in a sealed container). It was also possible to perform photolithography on a treated substrate before evaporation of the gold layer. This result provides a simple way to fabricate gold-only structures while maintaining excellent metal adhesion. A similar experiment using e-beam lithography was unsuccessful, suggesting that the high energy electrons destroy the integrity of the MPS layer while the UV energy used in photolithography does not have a similar effect.

The final test of the MPS/Au structure was to determine its electrochemical stability during acid cycling at high positive potentials (1M $HClO_4$, 100mV s^{-1}, 0 to +1.5V *vs.* Ag/AgCl). Stability was better than observed for the Ti/Au metallisation method (*ca.* 5-10 cycles), however, the gold-only structure did eventually begin to de-laminate after about 30 cycles. The adhesion failure was most likely caused by the oxidation of the thiol underlayer..

2.2.1.2 Multilayer Structure Metallisation

The need for a multilayer metallisation was driven by the work on the fabrication of the travelling-wave dielectrophoresis (TWD) electrode design shown in figure 2.2c. However, the procedures described could be applicable to the fabrication of any multilayer microbiosensor structure. The TWD electrode required two layers of metallisation that were connected by

'thru-holes' in the first layer of insulator. The first base metal layer was Ti/Pd/Au, the second layers investigated were either Ti alone, Ti/NiCr or Ti/Pd/Au. The insulator layer was PECVD silicon nitride (200nm) patterned using photoresist masking and C_2F_6 etching (see section 2.2.2.1.2).

There are two standard methods of 'thru-holing' used in microfabrication, either electroplating (be it electrochemical[53] or electroless[54]) or profiled metal-layer evaporation.[55] Electroplating methods deposit metals such as Ni, Cu or Au on regions exposed in the base metal layer following the etching of thru-holes in the insulator layer. The procedure completely fills the etch holes and subsequent thru-hole interconnection is achieved by evaporated/sputtered deposition of a metal layer. Work on the mechanism of gold electroplating was investigated and figure 2.3a illustrates the porous nature of the surface produced. Whilst electroplating can be a reliable and well characterised process[53,56] within the electronic industry, it was found to be difficult to control in the laboratory. The main difficulties were the poor electrochemical surface produced, solution degradation, and the variation in deposition rates associated with different shapes and areas in the exposed base metal layer. Further work is required on this topic to develop a consistent process. Electroplating is very cost effective in relation to metal evaporation/sputtering and an excellent method for the metallisation of high aspect ratio structures.

The key to successful 'thru-holing' by metal evaporation is the etching of thru-holes with walls at an angle of *ca.* 60°,[54] which is a compromise between a high hole density and reliability. The shallower the angle the more space each thru-hole feature occupies on the substrate. In comparison, steep angle thru-holes occupy less space but promote track breaks. The thru-holes produced using a C_2F_6 etch in the silicon nitride had an angle of *ca.* 80°, as measured by the observation of scribed substrate using a scanning electron microscope. This angle was rather higher than optimal and the available methods for reducing the angle, such as lowering etch power or increasing gas flow rate had little significant effect. A thorough analysis[57,58] concludes that thru-holes are best formed using either an isotropic wet etching or by using a low power RIE etching mechanism that is highly 'chemical' in nature (i.e. less anisotropic). Unfortunately, wet etching using HF acid was unreliable and the facilities for alternative RIE procedures were not available during this project. Nevertheless, for the TWD electrodes, the 80° angle thru-holed samples (Ti/Ni metallisation) resulted in a 66% (n=6) success rate as measured by using a simple continuity test.

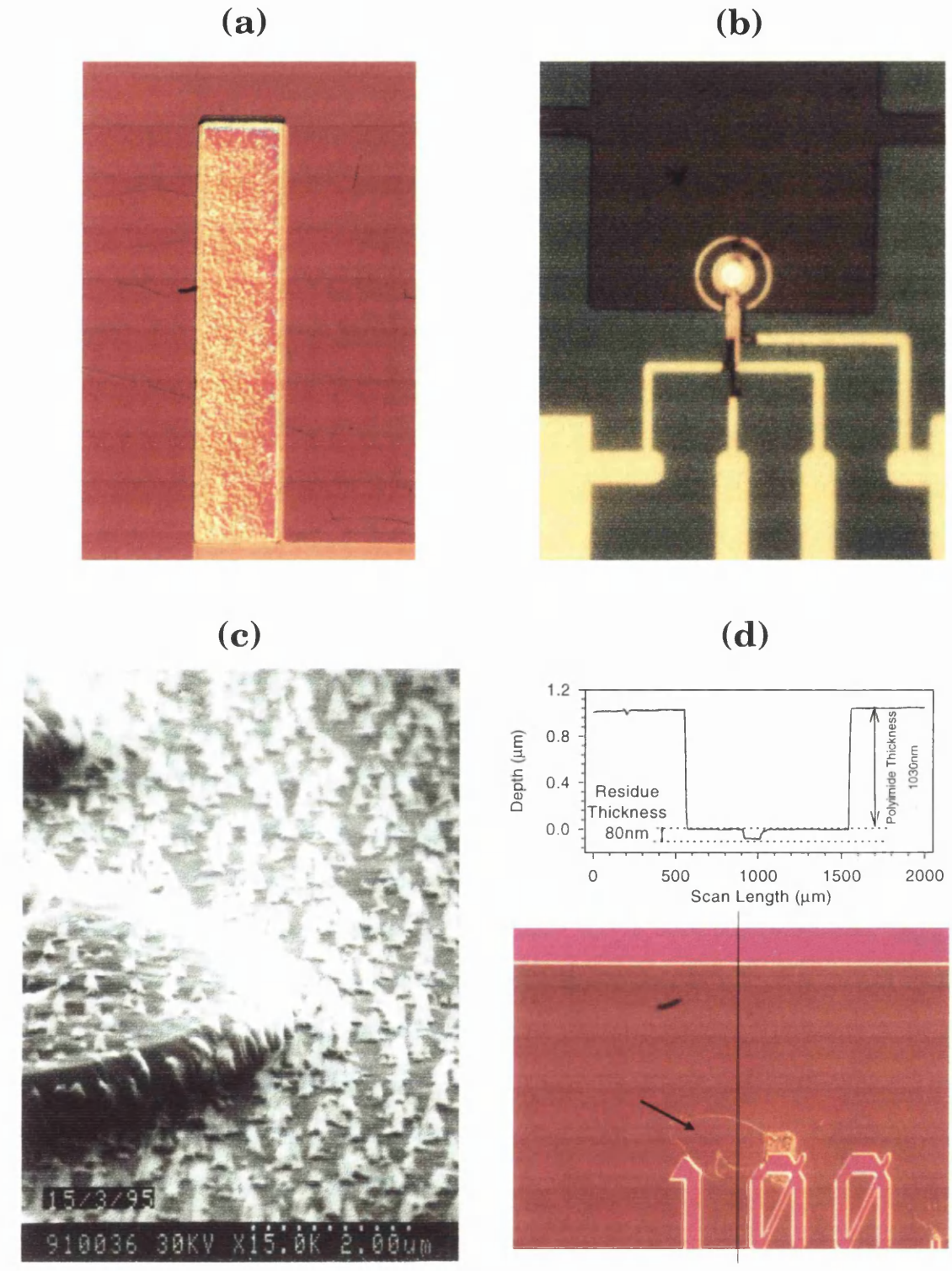

Figure 2.3: (a) An electroplated gold electrode, the photograph illustrates the rough nature of the plated surface. (b) A 'burnt out' ring electrode, the failure was caused by seepage of electrolyte between the poorly adhered insulator and substrate layers. (c) A dramatic example of the RIE etch residue ('polyimide grass'), *photograph courtesy of* F. Pottier. (d) An instance where the etch residue/resistant area (severely over-etched sample) has formed a uniform covering. A small region of residue (arrowed) in the centre of the sample has broken free, the surface profile (vertical line) provides an indication of thickness.

In addition, the choice of evaporated metal and its thickness had a significant effect on fabrication success. The initial method used was the e-beam evaporation of a 240nm thick layer of metal so as to fill the thru-holes etched in the 200nm thick insulator layer. The alternative method of evaporating a thinner layer (i.e. 50nm), to metallise the profile of the thru-hole was unreliable, probably due to track breaks caused by the high 80° thru-hole angle (see figure 2.4). Using a 240nm Ti layer alone was unsuccessful, due to the stress that existed within the evaporated metal film. This caused the metallisation to de-laminate during the lift-off process. This prompted the investigation of alternative 'low stress' metal films, such as, Ti/Pd/Au (20/20/200nm) and a mixed layer of Ti/Ni (60/20 in three consecutive layers). Both methods produced working thru-hole structures. The Ti/Ni option being preferred due to the prohibitive cost of evaporating 200nm of gold. The Ti/Ni mixed layer is thought to be successful for thick evaporated metallisation due to the counteracting effect[59] of the opposing stresses in the individual metals, this results in an combined film that is low stress in nature.

Whilst a satisfactory yield could be obtained using the above metallisation procedure, the performance of the TWD electrode structures was poor when used in solution. In a saline solution under the application of high AC potentials, the structure rapidly disintegrated. Failure was ascribed to the de-lamination of the silicon nitride from the substrate, a process seen previously in similar non-multilayer structures used in work on neural networks.[60] The failure mechanism of the silicon nitride has been identified as poor adhesion and latent stress within the insulator film. This problem is discussed in greater detail in section 2.2.2.2.

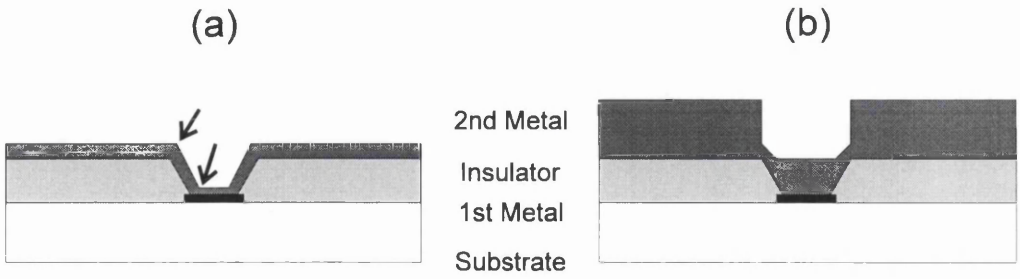

Figure 2.4: An illustration of the alternative 'thru-holing' methods investigated in the project. (a) A thin layer of metal coating the top surface of the insulator and the wall of the thru-hole. Probable location of track breaks are indicated by arrows. (b) A thick layer of metal that completely fills up the thru-hole

2.2.2 Sensor Insulation

The work on planar deposition and patterning of insulator layers focused on two materials: polyimide and silicon nitride. Polyimide is an organic polymer deposited by spin coating followed by curing at 350°C. Silicon nitride is deposited as an amorphous material using chemical vapour deposition (CVD). In this project PECVD was used, since the alternative CVD

method is a high temperature method[56] conducted at 900°C which is above the melting point of the gold used in the sensor metallisation. Polyimide can be deposited at a thickness from 0.5-20μm by adjustment of viscosity and/or spin speed. In contrast, silicon nitride is deposited as a thinner layer due to the slower rate of deposition (*ca.* 10nm min^{-1}) - standard film thickness ranged from 50-1000nm.

2.2.2.1 Patterning of Insulator Layers

Polyimide and silicon nitride can be patterned using both wet and dry etching techniques. The wet etch for polyimide is high temperature KOH[61] but this method was discovered late in the project, and was not investigated. The wet etch for silicon nitride is Hydrofluoric acid. This etching mechanism is inconsistent and was little used, since it would also etch the glass or quartz used as substrates for the electrode structures. For both insulators, the dominant patterning technique is RIE, using an O_2/CF_4 mixture for polyimide and either C_2F_6, CHF_3 or SF_6 for silicon nitride.

2.2.2.1.1 Polyimide - RIE Etching

Figure 2.5 provides details of the etch rate of PIQ13 polyimide using O_2 at a range of powers. The variation of etch rate with power is linear over the range 25-100W. Photoresist is an unsuitable etch mask, since it etches at a faster rate than polyimide.[62] The etch mask used was a 30nm layer of Ti that was subsequently removed using the procedure described in section 2.1.5.1.1. To promote a more isotropic etch for applications such as the shallower wall profiles required for thru-holes, the use of CF_4 has been recommended.[63] Whilst the structures fabricated in this project using polyimide did not require specific aspect ratios, the use of 5% CF_4 increased the etch rate by *ca.* 10% and improved the quality of the etching process by reducing the amount of deposited etch residue (termed 'polyimide grass' in the literature[54]).

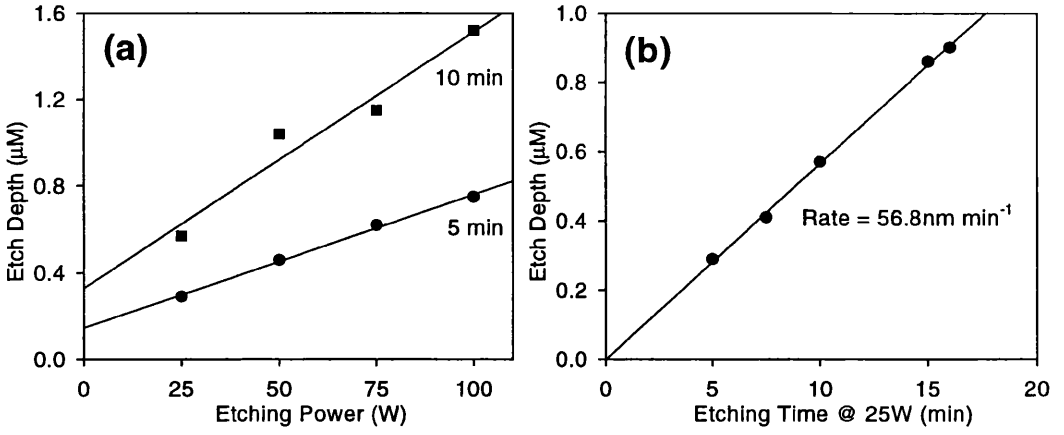

Figure 2.5: A comparison of the PIQ 13 polyimide etch rate (25W) at a range of powers (a), and the variation of etch depth with time (b). The polyimide was prepared as described in section 2.1.5.1 and was etched with oxygen (20sccm, 22mT) using an Oxford Plasma Technology BP-80 RIE machine.

The deposition of etch residue was a persistent and intractable problem encountered throughout the studies on polyimide and examples are shown in figure 2.3c&d Any residue remaining on the etched surface severely inhibited subsequent electrochemical studies due to fouling of the electrode surface. Over-etching the polyimide, in an attempt to remove the residue, only compounded the problem. It is suggested[64] that residue formation is based on the formation of metallo-organic compounds from reactions of RIE products with metal sputtered from the electrode structures. The residue components are resistant to the etching gases and form a permanent coating on the substrate. Hence, successful RIE etching is a very sensitive process requiring the minimal degree of over-etching necessary to form a viable electrode structure.

The methods used to reduce the amount of etch residue produced include: the reduction of etching power (to minimise metal sputtering) and the careful control of etch depth to ensure only a 2-5% over-etch. Whilst attempts were successful, the majority of electrodes were scrapped due to either excessive residue or under-etching. A interactive step-wise approach to the etching procedure was difficult to implement since the optimal etch-stop point was impossible to determine without an electrochemical test.

Polyimide is a flexible insulator with many advantages over silicon nitride. For example, it has a greater thickness range, excellent planarisation properties and improved adhesion. However, the difficulties with etch residue deposition need to be overcome before it can be used as a reliable element in electrochemical microbiosensors. Attempts in the literature at minimising the residue deposition have focused on the use of complex process control,[65] minimal etch power[66] and partial 'de-grassing' using a dilute HF acid wet etch.[67] Alternative methods include the use of photosensitive polyimide,[65] hence avoiding the need for RIE. Furthermore, the use of a thick hardened photoresist etch mask (instead of the standard Ti, Ni or Cr mask) is an option, the reduced surface area of exposed metal will limit the amount of sputtered metal particles within the RIE chamber atmosphere.

2.2.2.1.2 Silicon Nitride - RIE Etching

Silicon nitride etching using a photoresist mask was less sensitive to the residue deposition problems encountered during the patterning of polyimide (see section 2.2.2.1.1). However, excessive over-etching can result in similarly poor electrochemical surfaces. Etching in C_2F_6 was preferred to CHF_3 purely in terms of speed: 50nm min^{-1} in comparison to 30nm min^{-1}. The dominating difficulty encountered using silicon nitride was poor adhesion.

2.2.2.2 Insulator Adhesion

Insulator adhesion is a crucial factor in the stability of an aqueous biosensors. For devices such as integrated circuits, manufactured using standard microfabrication techniques, insulator

adhesion has only a minor effect on device reliability. However, the majority of microbiosensors are designed for use in an aqueous environment and hence reliable substrate/tacking adhesion becomes a crucial factor in controlling their performance and reliability. Poor adhesion leads to rapid device failure (see figure 2.3b) and a time-dependent electrochemical response determined by the rate of liquid seepage between the substrate and insulator layers.

Polyimide shows good adhesion to glass and quartz substrates, as tested using the 'Scotch' tape test. Its adhesion has been investigated in detail by other authors.[68,69] Silane based adhesion promoters (either spun-on as an initial step or included in the un-cured polyimide) can be used to form a firm chemical bond to the substrate. An area of significant concern is the adhesion of polyimide to the metal tracking. Any silane based promoters is unlikely to aid the metal to insulator adhesion (particularly for gold), a novel solution to this problem has been proposed by Cloud *et al.*[70] and was replicated during this study. The method required the use of a very thin (1nm) Ti layer deposited above the base metallisation (i.e. the final structure was Ti/Pd/Au/Ti). The upper Ti layer will be immediately oxidised to TiO_2 upon exposure to air. It is proposed that a thin layer TiO_2 will not contaminate the gold layer to the same extent as a thicker layer of partially oxidised Ti. Once the insulator has been deposited (adhering much better to TiO_2 than Au) the active gold surface can be exposed using a Ti etch (see section 2.1.5.1.1). Comparative 'Scotch' tape tests on glass slides coated Ti/Pd/Au-polyimide and Ti/Pd/Au/Ti-polyimide exhibited a dramatic improvement in insulator adhesion. Furthermore, macroelectrode samples prepared using the Ti/Pd/Au/Ti recipe, and subsequently wet etched to remove the top Ti layer, still demonstrated excellent thiol immobilisation characteristics found to be indicative of a pure gold surface (this was tested using cytochrome *c* electrochemistry, see section 3.1.3.3).

In contrast to polyimide, the PECVD silicon nitride available during the project had poor adhesion to glass and quartz. The use of adhesion promoters was impossible since the deposition process was performed at 300°C - a temperature that would destroy the majority of potential promoters. A major contribution to the poor adhesion has been identified as the residual stress in the PECVD film, this influence is exaggerated by the different thermal expansion properties of the substrate and the silicon nitride.[71] More recently, work has identified a procedure for the growth of a lower stress film.[72] The new procedure is based upon the careful control of helium content within the film. Initial trials[60] suggest that adhesion is markedly improved and further tests are in progress.

2.3 Summary

This chapter has described the many microfabrication methods investigated during the course of this project. The work on insulator patterning and adhesion was valuable although

problematic and the limitations of the process hindered the successful fabrication of functioning microbiosensor structures. A potential method for overcoming the formation of polyimide etch residue is the use of a combination of dry and wet etching. The insulator could be first etched using RIE to 90-95% of the desired depth and then the residual 5-10% could be removed using a brief wet etch. Once the process has been proven, the use of 'low stress' silicon nitride will present a improved method for sensor insulation

The further development of the MPS based system for the metallisation of gold-only structures presents exciting possibilities for precision electrochemistry using microbiosensors. The demonstrated use of a Ti 'top-layer' to improve metal to insulator adhesion will aid the fabrication of stable and durable microfabricated microbiosensors.

3. Microfabricated Biosensors

This chapter provides an insight into the response of sensors manufactured using previously described microfabrication techniques (see section 2.1). An electrochemical superoxide sensor (see figure 1.3, chapter 1) was chosen as the basis for the research. The sensor used the phenomenon of dielectrophoresis (see chapter 4) as a method of trapping a single human neutrophil that could act as a localised source of superoxide. The results are compared to those provided by using the alternative technique of chemiluminescence. Other factors such as sensor pre-treatment and durability have been characterised. The performance of a glucose biosensor was also investigated but the results are presented later in chapter 5, nonetheless, the background electrochemical theory presented in this chapter is applicable to both types of sensor.

3.1 Electrochemistry

A change in oxidation state or charge transfer are processes common to many chemical or biochemical reactions. The associated transfer of charge can be analysed using a variety of electrochemical techniques[73,74] to determine factors such as reaction kinetics and/or concentrations. The need for minimal signal transduction and the availability of accurate electronic instrumentation makes electrochemical measurement a popular approach in biosensor development. Electrochemistry was used extensively in this project for the analysis of surface cleanliness and for monitoring the response of a variety of sensor structures.

3.1.1 Theory: Electrochemistry

The standard techniques of chronoamperometry and cyclic voltammetry provided the backbone of the amperometric electrochemical analysis used in this study. The techniques were applied using both macro- and micro- sized electrodes and the effects of different electrode sizes is discussed below.

3.1.1.1 Chronoamperometry

This is a technique frequently used for the recording the response of voltammetric biosensors.[75,76] The technique relies on the measurement of the time course of a redox current at a constant potential. The working electrode of a three electrode configuration is maintained at a constant potential necessary to oxidise or reduce the analyte, the magnitude of redox current being related to the concentration of analyte in the reactant solution. The technique

provides a rapid method of quantitative analysis, however, calibration against known standards is necessary. A disadvantage of the technique is that only one point of the voltage/current curve is recorded. Variations in responses associated with sensor deterioration or contamination cannot be distinguished from changes in analyte concentration. An example current *vs.* time curve for a PPy/GOx glucose sensor is shown in figure 3.1.

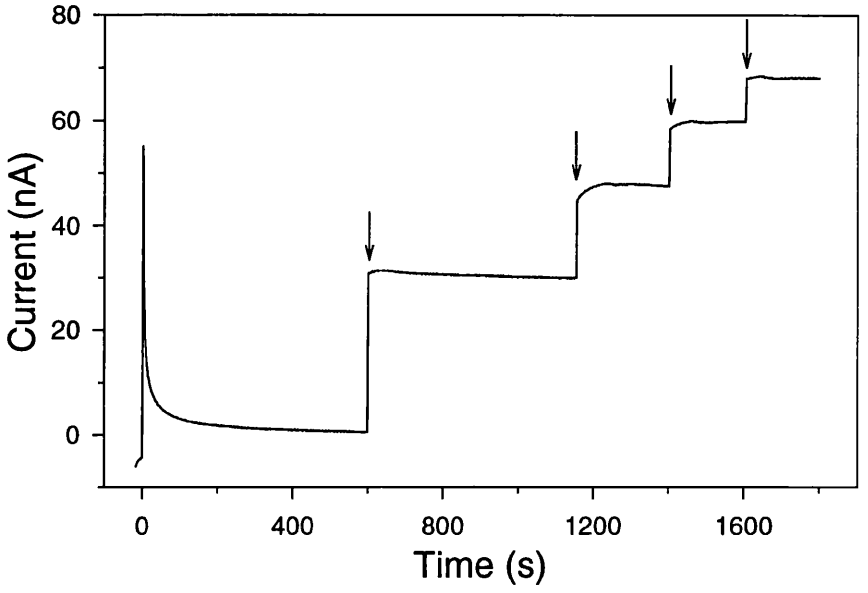

Figure 3.1: An example of the chronoamperometric response of a PPy/GOx sensor. Repetitive additions of the substrate (glucose) are indicated by arrows. The working electrode is maintained at a constant potential (+0.65V *vs.* Ag/AgCl). At this potential, oxidation of the product (hydrogen peroxide) produces a concentration dependent electrochemical current.

3.1.1.2 Cyclic Voltammetry

The technique involves the cycling of working electrode voltage between potential limits (see figure 3.2a), which are defined by the redox couple(s) of interest. This allows the fate of the electrochemical species created in the forward potential sweep to be probed during the return sweep. The technique is a popular method for the analysis of redox couples[77-79] and quickly provides information on the kinetics of the system.[80,81] The observed current is made up of two components. The first is a background (non-Faradaic) current component, associated with double-layer charging and adsorption effects at the electrode surface, whilst the second (Faradaic) current, provides information regarding the electrochemistry of the redox couple(s).

Sample experimental voltammograms for ferricyanide ($K_3Fe(CN)_6$) are shown in figure 3.2b. The peaks in the current response are observed due to the combined effect of a decreasing surface concentration and an expansion of the diffusion layer with time. The key parameters in a cyclic voltammogram are the anodic and cathodic peak currents, peak separation (ΔE_p), and

the half-wave potential. The half-wave potential is usually within a few mV of the formal potential of the redox couple. The peak separation provides information of the reversibility and number of electrons involved in the electrode reaction. Theoretically, the difference should be 59mV for a reversible one electrode redox couple at room temperature.

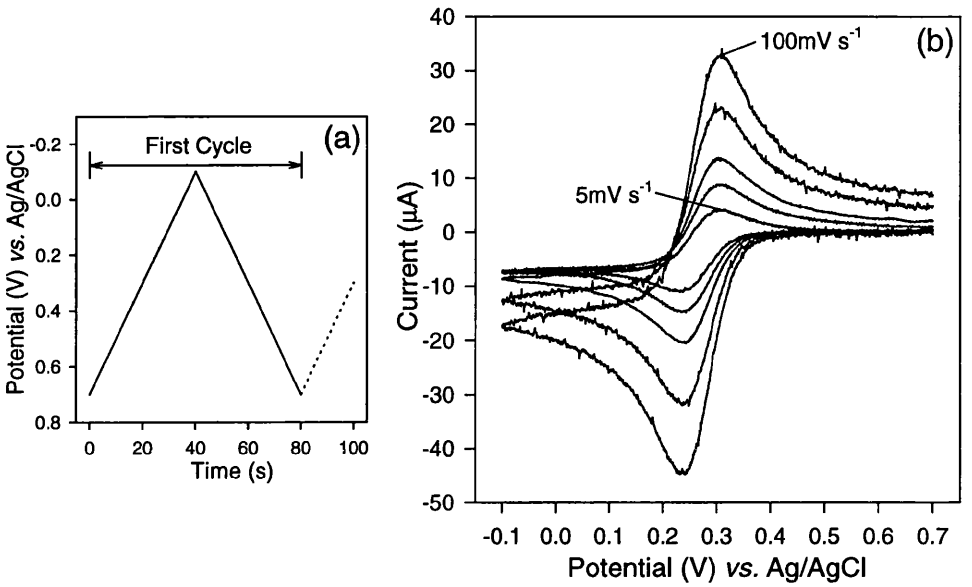

Figure 3.2: (a) One of the ramp potential profiles used in the above experiment (scan rate=10mV s^{-1}). (b) Cyclic voltammograms of ferricyanide (2mM) at a range of scan rates recorded using a 2mm diameter macroscopic gold electrode.

When the electroactive species are all in solution, the peak current (i_p) in a reversible system is proportional to the square root of scan rate (ν) as described by the Randles-Sevcik equation:[74]

$$i_p = 0.4463nFAD_o^{1/2}C_o\left(\frac{nF}{RT}\right)^{1/2}\nu^{1/2} \qquad (3.1)$$

where n is electron stoichiometry, F is the Faraday constant, R is the gas constant, T is absolute temperature, A is electrode area, C_o is the concentration and D_o is the diffusion coefficient of the oxidised species. When the redox species is surface bound and the response is not influenced by mass transport, there is a linear relationship with scan rate, given by:

$$i_p = \frac{n^2F^2}{4RT}A\Gamma\nu \qquad (3.2)$$

where Γ is the surface coverage of immobilised species on the electrode.

3.1.1.3 Microelectrodes

The small size of microelectrodes has been exploited in neuroscience research since the early 1960s. However, it was only in the early 1980s that the field was given a firm theoretical foundation by the pioneering work of researchers such as Wightman, Pons and Fleischmann.[82-84] A microelectrode has been defined as an electrode with at least one dimensions of <20μm in size.[85] The definition takes into consideration the properties of band microelectrodes which exhibit microelectrode properties while possibly having a relatively large total area. In this study, electrodes both 'macro' and 'micro' by definition were used in a range of different geometries.

Microfabrication presents many options for the manufacture of novel microelectrode structures[86,87] and arrays.[56,88,89] Smaller size, measurements in small volumes, batch production, on-chip signal processing are only some of the advantages that have been highlighted in the development of microbiosensors. With the improved current sensitivity of electrochemical equipment, microelectrodes offer a number fundamental practical advantages not offered by macroelectrode designs. These advantages can be summarised as follows:

1. Mass transport rate to an active surface is greatly enhanced, and steady-state (diffusion controlled) behaviour is easier to attain. For example, such behaviour makes a microelectrode particularly resistant to the effects of convection, so improving current stability and permitting stable measurements in flow-through systems.
2. Reduced influence of double-layer charging currents. Permits analysis of rapid electrochemical kinetics using faster scan rates.
3. Reduced '*iR*' potential drop across the electrolyte. Measurements can be made in low conductivity electrolytes.
4.

3.1.1.3.1 Mass Transport at Microelectrodes

Mass transport is the fundamental property that defines the nature of microelectrode response. The topic has been examined in standard electrochemical texts.[73,73] The change in the nature of the diffusion to a microelectrode in comparison to a macroelectrode is shown in figure 3.3

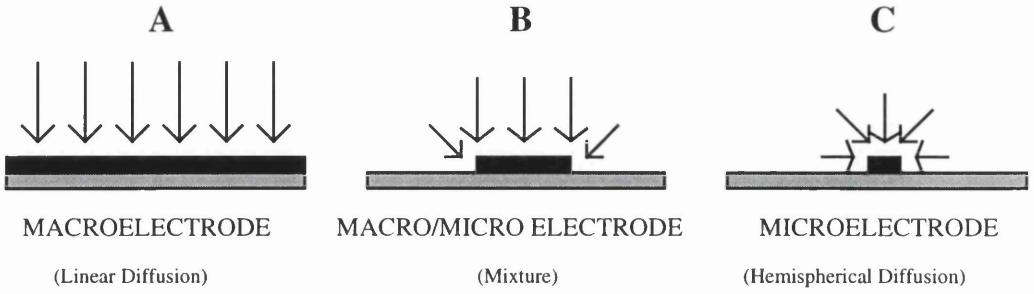

Figure 3.3: A comparison of diffusion profiles at macro and micro electrodes

As a basis for a theoretical analysis, consider the analysis of semi-infinite diffusion at a spherical electrode, where Fick's second law becomes:

$$\frac{\partial C_o(r,t)}{\partial t} = D_o\left\{\frac{\partial^2 C_o(r,t)}{\partial r^2} + \frac{2}{r}\frac{\partial C_o(r,t)}{\partial r}\right\} \tag{3.3}$$

Where t represents time, r is the radial distance from the electrode centre, C_o is the concentration and D_o is the diffusion coefficient of the oxidised species. Using Laplace transformation, a modified form of the Cottrell equation for diffusion current ($i_d(t)$) is obtained:

$$i_d(t) = nFAD_oC_o^*\left[\frac{1}{(\pi D_o t)^{\frac{1}{2}}} + \frac{1}{r_0}\right] \tag{3.4}$$

where r_0 is the radius of the electrode and C_o^* is the concentration of solution in the bulk solution. The first component on the right hand side of equation 3.4 represents linear diffusion present at both macro and micro sized electrodes. However, the second spherical diffusion component dominates the response of small radius microelectrodes particularly at longer diffusion time scales. Under these conditions the microelectrode response is independent of time and steady state diffusion control is easily established. Steady state currents can be determined for a variety of microelectrode geometries using simulation,[90] theoretical[91] and experimental[92] methods. Of particular relevance to this study was the micro-ring geometry. From a similar analysis of a ring capacitor,[93] the steady state diffusion current (i_{ss}) can be expressed as:

$$i_{ss} = nFC_o^* D_o \left[\frac{\pi^2 (d+a)}{\ln 16 \left({}^{(d+a)}/_{(d-a)} \right)} \right] \tag{3.5}$$

where a is the inner radius and d is the outer radius of the micro-ring structure.

3.1.2 Methods & Materials: Electrochemistry

All chemicals were obtained from Sigma/Aldrich, apart from 3,3'-dithiobis(sulfosuccinimidylpropionate) (DTSSP) which was obtained from Pierce. All solutions were prepared using RO water. Reactant concentrations and the pH of solutions will be quoted adjacent to the relevant results. The standard buffer was phosphate (KH_2PO_4 (113mM)/Na_2HPO_4 (296mM)) prepared to give a constant ionic strength (I=0.1)[94] at pH 7.4. In some instances, 300mM $NaClO_4$ was added to the buffer solution to reduce any '*iR* loss' that might affect the observed electrochemistry. To aid the solvation of hypoxanthine, a higher pH buffer (pH 8.0, KH_2PO_4(31mM)/Na_2HPO_4(323mM)) was necessary. Neutrophil suspensions were prepared in phosphate buffered saline (PBS; Sigma ref. no.: P-4417, pH 7.4) according to the method described in section 4.2.4.2, used over a period of up to four hours, and stored on ice between experiments. The neutrophils were activated using the chemotactic stimulant phorbol 12-myrsitate 13-acetate (PMA). The enzymes xanthine oxidase (XOx) (EC 1.1.3.22, Sigma ref. no.: X4376, from buttermilk; activity 0.75unit mg^{-1}) and superoxide dismutase (SOD) (EC 1.15.1.1, Sigma ref. no.: S2515, from bovine erythrocytes; activity: 5000unit mg^{-1}) were prepared in the buffer solutions used for each specific experiment.

Electrochemical responses were recorded either using an IBM PC controlled EG&G 273A potentiostat, or for low current measurements, a CV-100 potentiostat (Bioanalytical Instruments Inc. (BAS)) connected to a Lineseis LY1600 *x-y-t* chart recorder. Analog recordings were digitised using 'Digitize' software (©Danon Software, Israel). The electrochemical cell contained either a platinum gauze ($2cm^2$ area), or for microelectrode experiments a wire counter electrode (1mm diameter). All experiments were performed using a Ag/AgCl (3M NaCl) reference electrode (BAS) against which all potentials in this section are quoted.

Both macroscopic (BAS) and lithographically patterned evaporated gold electrodes (both 2mm discs) were used in the electrochemical analysis. The fabrication of the lithographic electrodes (10/10/100nm Ti/Pd/Au) is described in section 2.1, bonding pads and inactive areas of the planar structure were insulated using silicon adhesive (Dow Corning, RTV 3140). The macroscopic gold electrodes were cleaned by polishing in an alumina slurry of decreasing grain

size (3μm, 0.3μm, and 0.05μm) followed by ultrasonic cleaning in RO water. The evaporated gold electrodes were RIE cleaned in an O_2/Ar plasma, see section 3.1.3.1.2 for full details.

The immobilisation of cytochrome *c* was performed using either 1-ethyl-3-(3-dimethylaminopropyl) carbodiimide (EDC) or DTSSP protein coupling chemistry (see table 3.1). The experimental protocols are based upon those described by McNeil *et al.*[95,96] All solutions described in table 3.1 were prepared in phosphate buffer (I=0.1, pH 7).

Step No.	EDC Based Immobilisation	DTSSP Based Immobilisation
1	Clean electrode	Clean electrode
2	Immediately immerse electrode in 10mM N-acetyl cysteine (NAC) for 1 hour	Immediately immerse electrode in 100mM DTSSP for 2 min
3	Wash in RO water	Wash in RO water
4	Place modified electrode in 25mM EDC for 1 hour	Place activated electrode in 5mg ml^{-1} cytochrome c at 4°C for 12 hours
5	Wash in RO water	
6	Place activated electrode in 5mg ml^{-1} cytochrome c at 4°C for 12 hours	

Table 3.1: The experimental protocols for the EDC and DTSSP based protein immobilisation procedures.

3.1.3 Results and Discussion: Electrochemistry

This section will focus on the use and response of microfabricated electrochemical sensors. Microelectrode properties will be discussed and considerations of electrode preparation will be addressed. The protein electrochemistry that forms the heart of the superoxide sensor has been investigated in detail. Sensor response based upon two immobilisation techniques are discussed, and the different responses of macroscopic and microfabricated electrodes are highlighted.

3.1.3.1 Cleaning of Microfabricated Electrodes

A clean working electrode surface is a crucial factor in the recording of accurate and reproducible electrochemical results. Preparation of clean electrochemical surfaces on microfabricated electrode structures presents further challenges when compared to the methods used in standard electrochemical experiments. Polishing using alumina or diamond pastes is not a practical option due to the thin planar nature of the microfabricated electrode arrays. In addition, the option of using strong oxidants (e.g. piranha (H_2SO_4/H_2O_2) solution) is undesirable, since they can attack the substrate and insulator layers. The alternative cleaning methods,

described in the literature, focus on potential cycling[97,98] and plasma cleaning.[89,99] Both methods were investigated in this project and the results are presented below.

3.1.3.1.1 Potential Cycling in Acid Solutions

Potential cycling/cleaning, usually in sulphuric or perchloric acid, until a consistent response is recorded is a popular method that relies on either hydrogen evolution at negative potentials[100] or electrode oxidation at positive potentials.[101] The use of negative potentials proved unsatisfactory for two reasons. Firstly, the hydrogen evolution resulted in the accelerated delamination of any insulator layer. Secondly, in the analysis of cleaning at 'non-insulated' areas it proved to be less effective than the use of positive oxidative potentials. Successful cleaning using oxidative potentials required a carefully controlled procedure. Excessive cycling will result in the rapid deterioration of the thin electrode surface (100nm gold) This was most notable at the electrode edges, which experience the highest current densities. Whilst it should be noted that the use of adherent metal structures (see section 2.2.1) will improve durability, deterioration at the electrode edges can nonetheless have a dramatic effect on the performance of these microelectrode structures.[56]

In the optimisation of cleaning methodologies, analytical work was performed at macro-sized (2mm diameter) evaporated gold disc electrodes prepared using lithographic techniques. Typical responses during cycling are shown in figure 3.4a, the gold surface is first oxidised (>1.1V) and then reduced (at *ca.* 0.85V) with the aim of removing any surface contamination. This method is satisfactory for removing a thin layer of surface contamination, for example an adsorbed monolayer, however, thicker deposits of contamination hinder diffusion to the electrode surface and impede the oxidation mechanism (i.e. the formation of gold oxide). An alternative approach, is the addition of chloride ions into the solution to permit the formation of gold chloride complex. In contrast to insoluble gold oxide, the chloride complex is soluble and its solvation will result in etching of the gold electrode. Careful selection of experimental parameters can allow the surface to be etched in a controlled manner to reveal a fresh gold surface. Figure 3.4b, provides an illustration of the chloride etching procedure, under these experimental conditions the etch rate is *ca.* 2nm/cycle.

The cleaning procedure proved successful and was tested by observing the response of standard electrochemical couples such as ferricyanide or ferrocene - a ΔE_p close to the theoretical value of 59mV being a good guide of efficient electrochemistry. Care is required with the above procedure to ensure that the entire gold surface is not removed (e.g. after the 50-60 cycles, as seen figure 3.4). Furthermore, the procedure increases the microscopic roughness[1] of the electrode, as demonstrated by the increasing current with successive cycles seen in figure 3.4.

---

[1]Roughness is defined as real area/geometric area. Typically, values range from 1.1 to 3.0[102]

A potential disadvantage suggested by Creager *et al.*[50] concerns the poor quality of thiol monolayers that are formed on gold surfaces cleaned by cycling in chloride solutions.

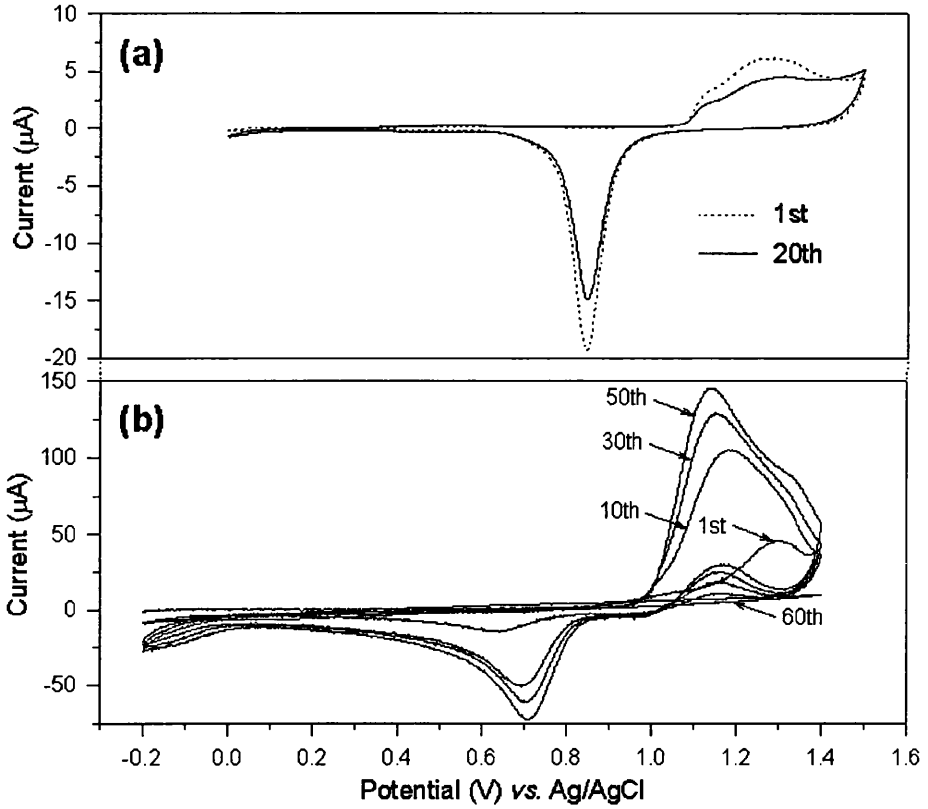

Figure 3.4: Potential cycling cleaning mechanisms on evaporated gold disc electrodes (2mm diameter, 100nm thick) at a scan rate of 100mV s^{-1}. (a) Illustrates the potential profile of successive cycles in 1M H_2SO_4. (b) The potential profile of successive cycles in 1M H_2SO_4 + 10mM KCl. In this case, the presence of chloride permits the formation of soluble gold chloride complex which etches the gold surface. The etching process on successive cycles increases the roughness of the gold surface, hence the increasing oxidative current. When all the gold is removed (*ca.* 60th scan), a insubstantial current is recorded

In summary, the careful use of cycling in chloride solutions is one of the better methods (from a limited choice) of cleaning microfabricated electrode structures. Great care is required in the selection of experimental parameters and it is suggested that only a few nm of the gold surface be removed (e.g. 2 cycles using the parameters described in figure 3.4b). Furthermore, it is important that the surface is first cleaned of particulate matter using a standard lithographic cleaning techniques (see section 2.1.1), otherwise uneven gold etching will occur. These cautionary comments are particularly important when the technique is applied to microelectrode structures as the effect of hemispherical diffusion will result in even faster etch rates.

3.1.3.1.2 Plasma Cleaning

The technique of plasma cleaning is common in the semiconductor industry as a means of cleaning substrates.[55,64] Argon or oxygen are the gases most frequently used. Argon is effective at the removal of adsorbed water, while oxygen is excellent for the removal of organic contamination. The ion plasmas are created using radio frequency energy at low pressures and the ions can be directed towards the substrate using a biasing voltage between the electrodes within the chamber. The energy of the ions is closely related to the bias voltage, and too high an energy can result in excessive sputter removal of a metals from the microfabricated structure. Gold was the predominant electrode surface used in this study and is a particularly 'soft' metal in respect of plasma sputtering. Hence, the selection of an appropriate bias voltage is an important parameter in the RIE cleaning protocol.

The RIE parameters that determine the nature of the etching/cleaning procedure include: machine, pressure, gas, gas flow rate, etch time and bias voltage. Only bias voltage was varied, all other parameters remained constant and the standard values are given in table 3.2. Using the PlasmaFab ET340 RIE machine, the minimum bias voltage was -160V, hence a slightly higher value of -180V was selected to ensure that a plasma could be 'struck'. The bias voltage could be increased up to -250V and a similarly successful cleaning procedure would result. Bias voltages above -250V resulted the in onset of significant gold sputtering, for example, at -350V, a 100nm layer of evaporated gold would be removed in 8 minutes.

Etch Parameter	Value
Machine	PlasmaFab ET340
Etch Pressure (O_2)	50mT
Etch Pressure (Ar)	11mT
O_2 Flow Rate	50sccm
Ar Flow Rate	20sccm
Bias Voltage (O_2 and Ar)	-180V (equivalent power ~2W)
Etch Time	3 min (per gas)

Table 3.2: RIE parameters for the plasma cleaning of evaporated gold electrodes.

Any over-etching was evident by the obvious removal of the gold, so that the titanium/palladium underlayer was exposed. An effective method used to test the cleaning procedure was the investigation of cytochrome *c* electrochemistry. This redox couple is described in detail in section 3.1.3.3. The electrochemistry relies on the preparation of a clean gold surface for the immobilisation of a thiol-mediator that promotes efficient electron transfer

from the adsorbed protein. A contaminated electrode surface will result in poor electrochemistry. Figure 3.5 illustrates the effectiveness of plasma cleaning in the preparation of an evaporated gold surface for thiol immobilisation and subsequent recording of good cytochrome *c* electrochemistry (ΔEp=72mV). To further illustrate the effectiveness of the cleaning procedure, the same electrode was RIE etched and the electrochemical procedure repeated. A similar voltammogram was recorded, but this time with a higher background and slightly increased peak separation (ΔEp=85mV). This result demonstrates the effectiveness of the RIE cleaning method and its potential use in repeated cleaning of the same electrode structure.

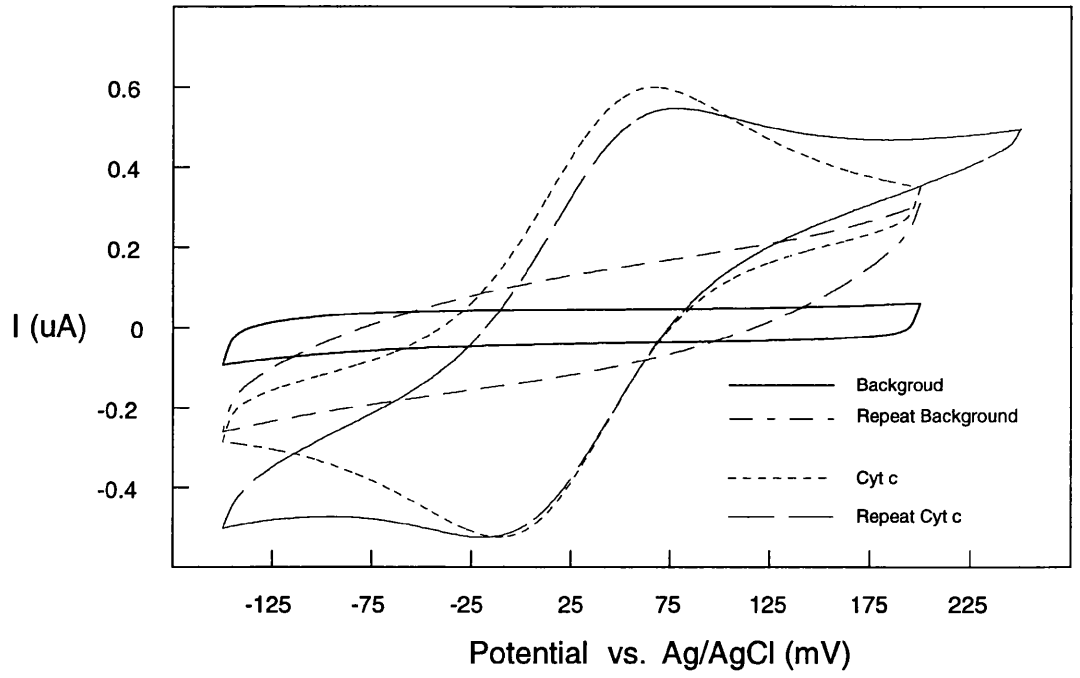

Figure 3.5: Cyclic voltammograms of a 2mm diameter evaporated gold disc electrode in a solution of 5mg ml^{-1} cytochrome *c* + 300mM $NaClO_4$ at a scan rate of 50mV s^{-1}. The electrode has been plasma cleaned using the RIE parameters detailed in table 3.2. Following each plasma clean the gold electrode is modified with 10mM NAC (I=0.1, pH 7.4 buffer) for 1 hour. The background scans of the NAC modified electrode in 300mM $NaClO_4$ are included for comparison. The voltammogram illustrates the effectiveness of the RIE cleaning method and its potential use in repeated cleaning procedures.

It is recommended that the structure is first cleaned of particulate matter using a standard lithographic cleaning techniques (see section 2.1.1). Furthermore, once RIE etched, the electrodes should be immediately used or stored in RO water to minimise the contamination from the atmosphere.

3.1.3.2 Microelectrode Sensors

Some of initial research concentrated on the fabrication and characterisation of micro-ring electrodes. It was envisaged that these would provide the sensing element of the single cell superoxide sensor described in section 1.3.1. The first fabrication step proved successful, and

examples of micro-ring structures have been shown earlier (see figure 2.3). The performance of the structure was analysed using ferricyanide electrochemistry and the response at low scan-rates demonstrates the classic steady-state sigmoidal response expected for a microelectrode (see figure 3.6a). At the higher scan rates (figures 3.6b and 3.6c), the mechanism of the microelectrode response changes and the shape of the cyclic voltammogram is influenced by the depletion of reactants at the electrode surface. The magnitude of the recorded steady state current was 3.6nA, significantly higher than the 0.45nA predicted using theory (see equation 3.5; using D_0=6.3x10^{-6}cm^2 s^{-1},[81] d=25μm and a=23μm).

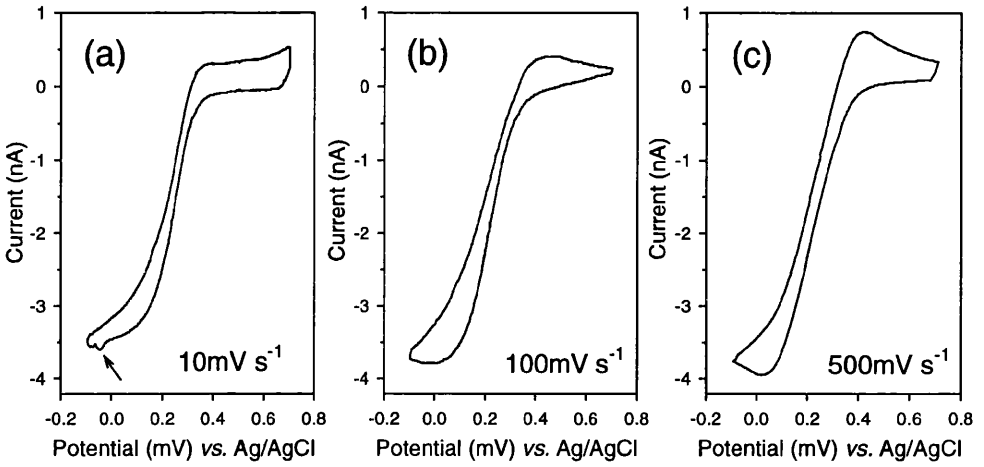

Figure 3.6: Cyclic voltammograms for the outer ring of the gold micro-ring electrode shown in figure 2.2 at a range of scan rates. The electrochemical response of the structure has been recorded in 1mM $K_3Fe(CN)_6$ + 300mM $NaClO_4$ solution using a Pt wire counter electrode. The electrode structure was cleaned using a RIE plasma. Note the steady-state response at low scan rates (a), that ceases to be diffusion limited at higher scan rates (b & c).

The response of the microfabricated micro-ring electrode was initially stable. However, repeated use led to an inconsistent response and eventual failure. The cause of the failure was ascribed to two processes. Firstly, the dominant process was poor adhesion of the insulating (silicon nitride) layer to the substrate. This permitted seepage of electrolyte into the intervening space, leading to a time dependent rise in exposed electrode area. The associated increase in current helps to account for the difference between the measured and theoretical steady-state current values. In some cases, the increased electrochemical current resulted in a 'burn-out' of the structure at a location originally isolated from the aqueous solution (see figure 2.3). Secondly, in some instances, delamination of the micro-ring structure was observed. This was particularly evident when the structure was exposed to high oxidative potentials (>0.5V). This failure mechanism is most likely the oxidation of the titanium underlayer used to promote the adhesion of the evaporated gold to the substrate.[51] Furthermore, it is suspected that the small unexplained reducing current arrowed in figure 3.6a may be a component of this titanium electrochemistry.

An exhaustive investigation of these failure processes is described in detail in section 2.2.2.2. In summary, the difficulties with insulator adhesion were addressed by investigating adhesion promoters, reducing the stress in the insulator layer, and the use of alternative insulators. The delamination effect of Ti underlayer oxidation was successfully reduced by the use of a Pd intermediary layer (i.e. Ti/Pd/Au) and minimising the use of high oxidative potentials. These aspects presented numerous challenges, moreover, until they were overcome only a limited amount of worthwhile electrochemical analysis could be performed at similar microfabricated microelectrodes.

3.1.3.3 Cytochrome c Electrochemistry

The investigation of the solution electrochemistry of cytochrome *c* was the first step in the development of the superoxide sensor described in section 1.3.1. Eddowes & Hill[103] were the first to demonstrate the quasi-reversible electrochemistry of the protein on gold electrodes using 1,2-Bis(4-pyridyl)ethylene as an electron transfer promoter. Since then there have been many publications analysing the electrochemistry at a variety of different metal surfaces[104-106] and using a range of different promoters.[107-109] Figure 3.7 presents a similar experimental comparison of cytochrome *c* electrochemistry recorded using the range of thiol-promoters.

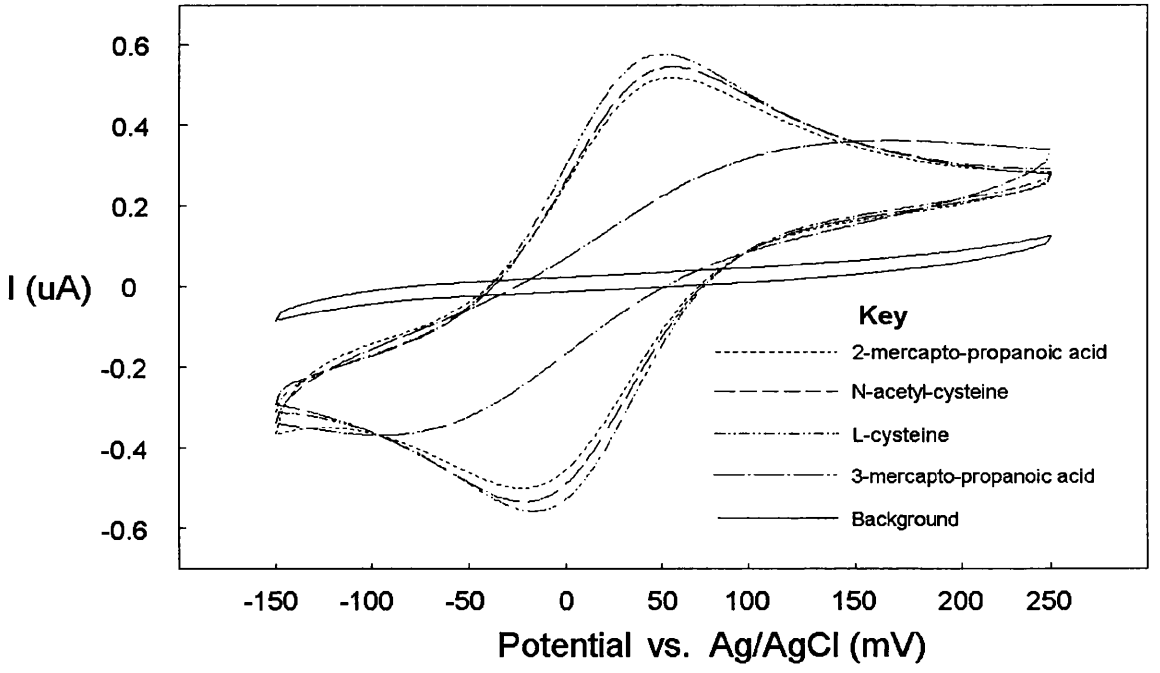

Figure 3.7: Cyclic voltammograms of 2mm diameter evaporated gold disc electrodes in a solution of 5mg ml^{-1} cytochrome *c* + 300mM $NaClO_4$ at a scan rate of 50mV s^{-1}. The electrodes have been RIE plasma cleaned and modified using a range of promoters at concentrations of 10mM (I=0.1, pH 7.4 buffer) for 1 hour. The background scan in 300mM $NaClO_4$ (50mV s^{-1}) for the NAC modified electrode has been included for comparison. The voltammogram compares the relative ability of each modifier to successfully promote the redox electrochemistry of cytochrome *c*.

A good indication of efficient electron transfer is the reversibility of the redox process, as indicated by a value of ΔEp close to the ideal of 59mV. All the modifiers in figure 3.7, except 3-mercapto-propanoic acid, exhibited good electron transfer properties with ΔEp in the range 65-80mV. NAC was selected as the thiol for subsequent work since it is believed that its acetyl group can aid the steric co-ordination of the electroactive haem centre of the protein.[110] Figure 3.8 illustrates the electrochemistry of cytochrome *c* at a range of scan rates. The linear variation of i_p *vs.* $v^{1/2}$ confirms that the redox process is controlled by the diffusion of electroactive species in solution. Analysis of the variation of scan rate and ΔEp using the method of Nicholson[80] provided a k_s of 4.9×10^{3}cm s^{-1} ($D_o = 9.4 \times 10^{-7}$cm^2 s^{-1}[103] and assuming an $\alpha = 0.5$). This value is close to the 2.3×10^{3}cm s^{-1} reported in a similar study using NAC.[110]

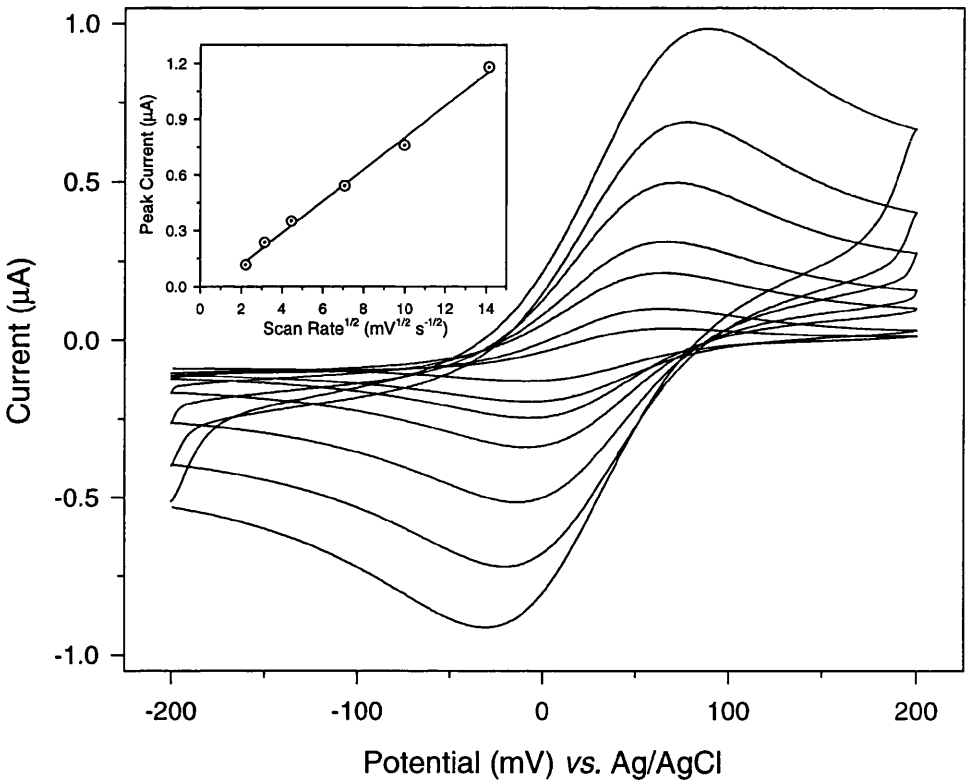

Figure 3.8: The variation of ΔEp with scan rate (5, 10, 20, 50, 100 and 200mV s^{-1}) for a 2mm diameter evaporated gold disc electrodes in a solution of 5mg ml^{-1} cytochrome *c* + 300mM $NaClO_4$. The electrode had been RIE plasma cleaned and modified using 10mM NAC (I=0.1, pH 7.4 buffer) for 1 hour. The linear variation of i_p *vs.* $v^{1/2}$ shown in the inset graph demonstrates that the redox process is controlled by the diffusion of the electroactive species in solution.

3.1.3.4 Superoxide Sensing

The first step in the preparation of a superoxide sensor based on cytochrome *c* electrochemistry is the immobilisation of protein on the electrode surface. The results of this procedure are described below, along with measurements of superoxide production generated using two

different mechanisms. The first mechanism is based on the enzymatic breakdown of hypoxanthine by XOx, the second is the chemotactic stimulation of human neutrophils by PMA.

3.1.3.4.1 Immobilisation of Cytochrome *c*

Previous work on the immobilisation of redox proteins such as cytochrome *c*, has been based on the formation of a peptide linkage to the protein shell. For example, Bowden *et al.*[111] used long chain carboxyl group terminated thiols ($SH\text{-}((CH_2))_n\text{-}COOH$, n=6,11,16) immobilised on gold, followed by covalent linkage to the protein amino groups using EDC chemistry. A similar approach was used by Cooper *et al.*,[95] but using NAC to form the thiol monolayer. An alternative approach was demonstrated by Lotzbeyer *et al.*,[112] where and amino terminated thiol (cystamine) was coupled using EDC chemistry to carboxylate residues on the protein shell. In each of the above examples, successful protein immobilisation was demonstrated by monitoring the protein redox electrochemistry (direct electron transfer) in fresh buffer solution.

A similar approach of using thiol monolayers was adopted in this study, but the observed protein electrochemistry at microfabricated surfaces was both inconsistent and short-lived. However, as the results presented in section 3.1.3.4.2 will demonstrate, some protein has been immobilised on the electrode surface, but most likely not in a sufficient quantity to generate a significant redox response in comparison to the background current. In the attempt to improve the observable direct electrochemistry, a wide variety of experimental parameters were adjusted according to recommendations made in the literature. These included adjustments in supporting buffer composition,[112] gold surface (sputtered or evaporated gold[8]), electrode cleaning methods,[50] and protein purification.[95] None of the parameter changes was dramatically successful, a quantitative comparison being difficult due to the lack redox electrochemistry or inconsistency of response.

An alternative approach to a three-step[2] coupling procedure is to use a two-step procedure where the immobilised thiol contains an active group capable of directly forming a peptide bond to the protein. DTSSP can be used for this purpose, forming a peptide bond with the protein and resulting in a succinimidyl leaving group (see figure 3.9). Again, clear direct electrochemistry was not evident. However, a comparison of the two immobilisation methods in terms of an amperometric assay (of the form shown in figure 3.12) for superoxide suggests that the DTSSP method is superior - coupling an estimated four times more protein to the electrode.[96] Subsequent work focused solely on the use of the DTSSP immobilisation mechanism.

[2] i.e. 1) thiol immobilisation, 2) EDC linkage, and 3) protein coupling

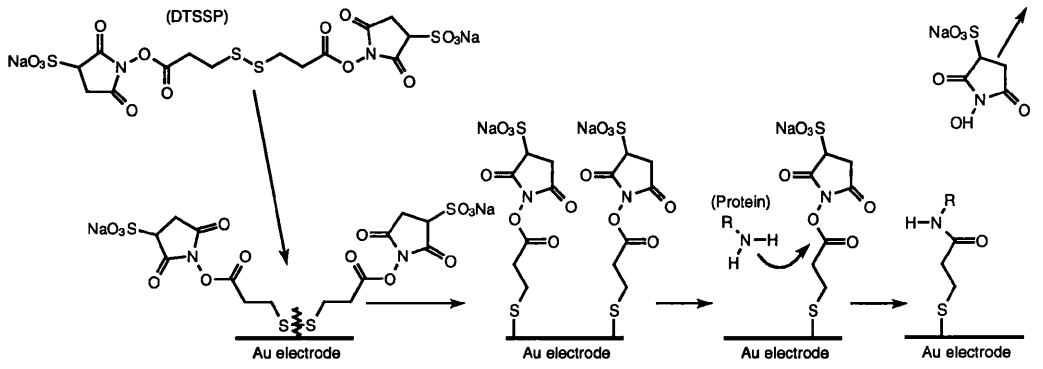

Figure 3.9: The chemistry associated with the DTSSP/protein immobilisation procedure.

The formation of the DTSSP/protein bond is a pH dependent reaction. Extreme pH values are undesirable since the protein will become de-natured and values in the literature remain within the range pH 6 to 8. A pH in the range 6.5 to 7.5 was used, since it aided the forming of the peptide linkage by protonating the amine residues on the protein, while not leading to excessive hydrolysis of the DTSSP. Figure 3.10 presents the electrochemistry of immobilised DTSSP. Initially, it was believed that cytochrome *c* was responsible for the redox wave, however, the $E_{1/2}$ of +170mV was significantly higher than previously reported ($E_{1/2}$=20mV).[95] Control experiments using DTSSP alone generated the same results and the linear variation of peak current *vs.* scan rate indicated that the redox species was surface bound (see figure 3.10). It can thus be concluded that the DTSSP or a decomposition derivative is responsible for the electrochemistry.

This response is surprising for a thiol bonded to a gold surface, since previous reports have concentrated on adsorption/desorption electrochemistry at high (>0.8V) positive potentials[113] and their use as modifiers in forming insulating surfaces.[114] Some suggested mechanisms for the observed behaviour include the charge transfer between the gold and sulphur atoms, or the reversible formation of thiol/di-thiol bonds at the gold surface. A comprehensive understanding of the behaviour will require further work, and it is notable that similar thiol behaviour has been observed by another research group.[115] The electrochemistry of DTSSP is curious, but it does not affect the specificity of the superoxide sensor (see section 3.1.3.4.2). Nonetheless, a better understanding of the mechanism can only contribute to the future sensor developments.

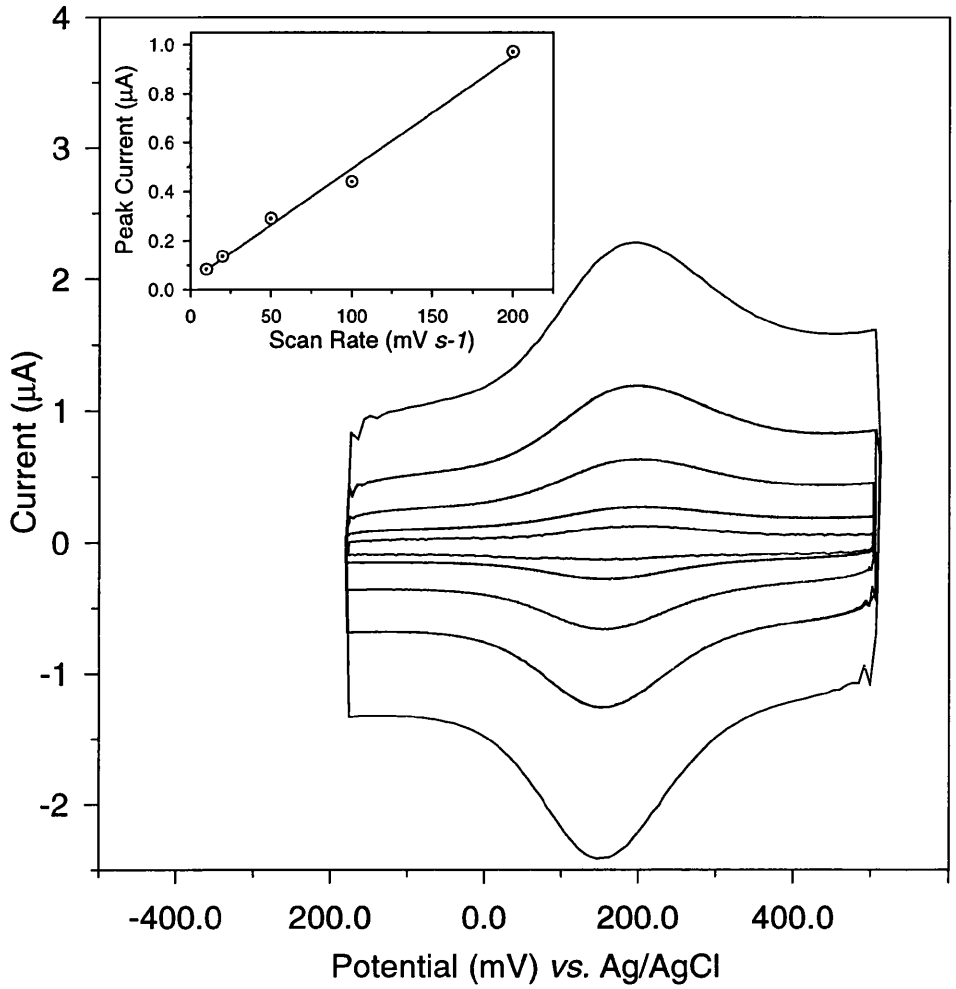

Figure 3.10: The electrochemical response of immobilised DTSSP (2mm diameter evaporated gold disc electrode) in a solution of I=0.1 (pH 7.4) buffer + 300mM $NaClO_4$ at a range of scan rates (10, 20, 50, 100 and 200mV s^{-1}). The monolayer was formed by immobilisation from a solution of 100mM DTSSP in I=0.1 (pH 7.4) buffer for 10 minutes. The electrode was cleaned by cycling in 1M $HClO_4$ until a consistent response was recorded. The linear variation of i_p *vs.* v shown in the inset graph demonstrates that the observed redox process is determined by a surface bound species.

3.1.3.4.2 Superoxide Measurement: Hypoxanthine/Xanthine Oxidase

The use of hypoxanthine/XOx is a standard enzymatic method of generating superoxide and other reactive oxygen species (see figure 3.11). It provided a rapid method of assessing the performance of the DTSSP/cytochrome *c* superoxide sensor (no cell purification required) and provided a convenient method for recording the reference response of each electrode.

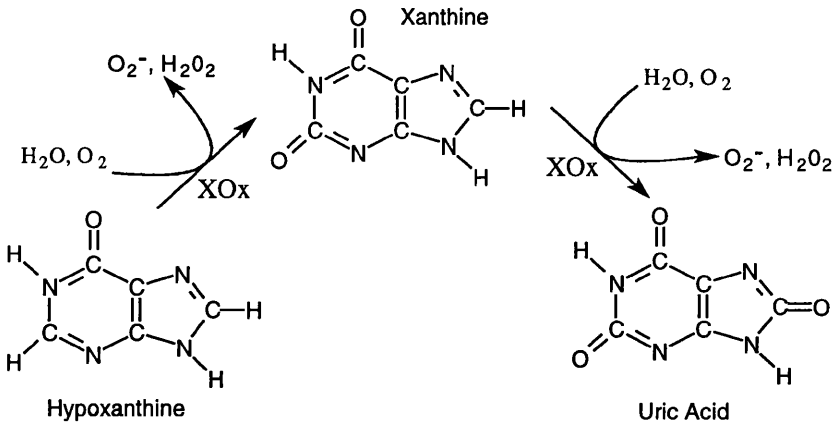

Figure 3.11: The mechanism of superoxide generation using hypoxanthine/XOx chemistry.

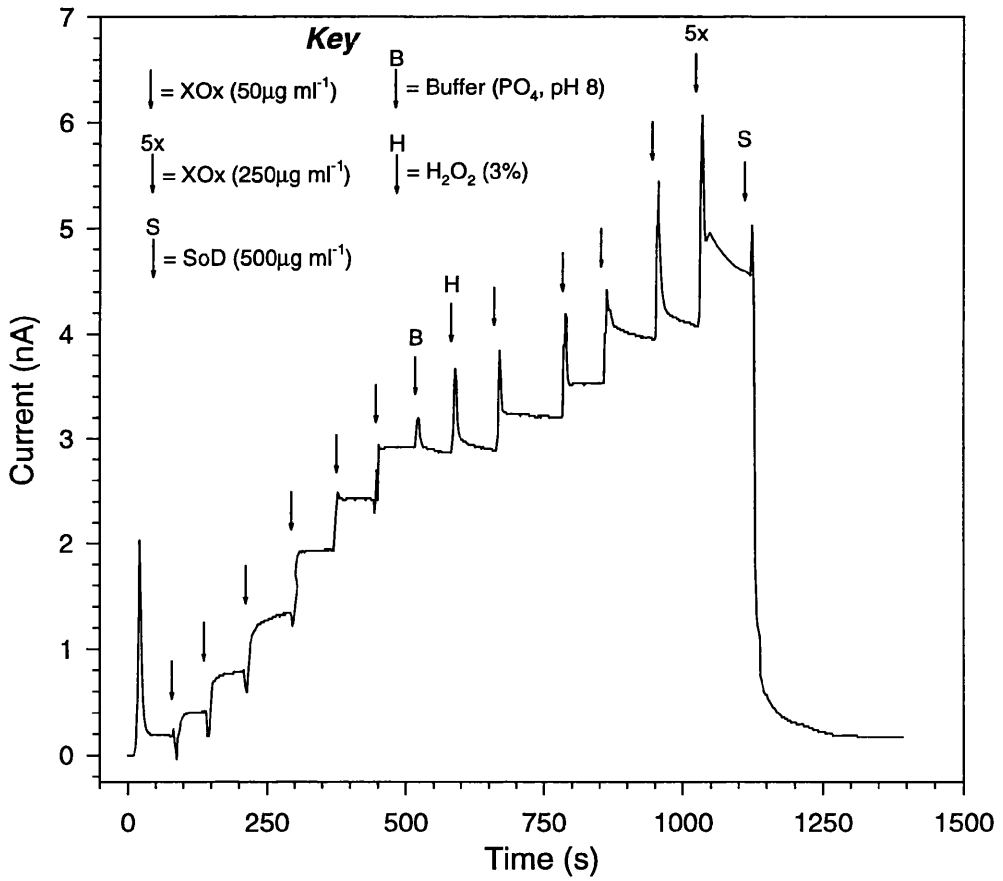

Figure 3.12: Amperometric assay for superoxide using a RIE cleaned 2mm diameter evaporated gold disc electrode activated using the DTSSP/cytochrome *c* chemistry described in section 3.1.2. The working electrode was poised at +100mV *vs.* Ag/AgCl, a potential capable of oxidising the immobilised cytochrome *c* that has been reduced by its reaction with superoxide. The stock solution is 1.5mM hypoxanthine prepared in I=0.1 (pH 8.0) phosphate buffer. The timing and concentration (final value) of the additions (50µl) are indicated using labelled arrows that correspond to the key in the figure.

Figure 3.12 illustrates an amperometric assay for superoxide, the additions of enzyme produced a concentration dependent response while the substrate remained in excess (1.5mM). Specificity is demonstrated by the lack of significant response to additions of buffer or hydrogen peroxide. In contrast, the addition of the enzyme SOD, a highly specific scavenger of superoxide ions, rapidly reduces the current to the baseline level.

An alternative method of analysing the amperometric response is to monitor the rate of superoxide release.[95] Figure 3.13 provides a comparison between superoxide measurement using both macroscopic and evaporated gold electrodes. The response is significantly reduced (*ca.* 5 times less) at the evaporated gold electrode even though both electrodes have the same area and were prepared simultaneously using the same solutions. The only difference in the preparation of the electrode surfaces was in the cleaning procedure (polishing or RIE cleaning). However, this would appear to make little difference, since the two types of gold surfaces have already been compared using the homogeneous electrochemistry of cytochrome *c* (see section 3.1.3.3), and little or no difference was apparent. In contrast, during the comparison of superoxide response, the evaporated gold electrode response was consistently lower. This observation suggests that the nature of the gold surface has a significant effect on the quantity of immobilised protein, or more precisely, the quantity of protein in electronic communication with the electrode.

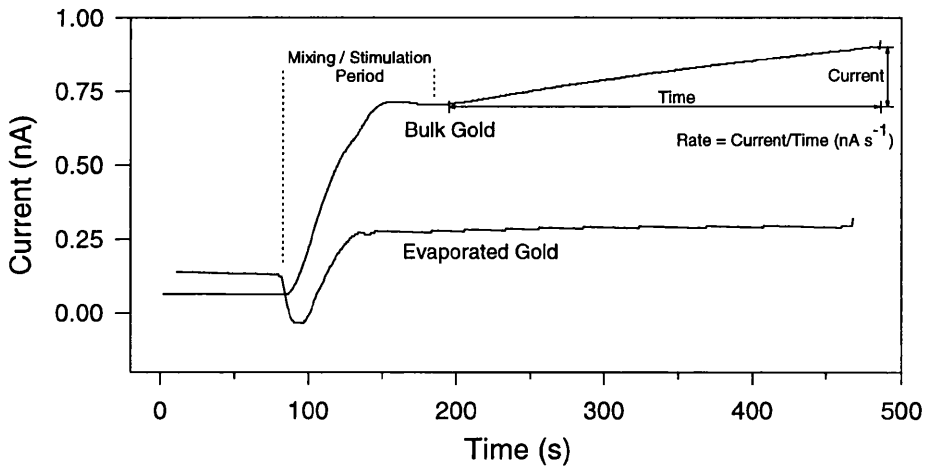

Figure 3.13: A current *vs.* time plot comparing the response of macroscopic and an 2mm diameter evaporated gold disc electrodes activated using the procedure described in section 3.1.2. The working electrode was poised at +100mV *vs.* Ag/AgCl in 100mM hypoxanthine prepared in I=0.1 (pH 8.0) phosphate buffer. Superoxide generation was initiated by the addition of XOx to a final concentration of 125mg ml^{-1}. The short delay associated with mixing and the neutrophil activation process has been indicated.

It is difficult to find a concise explanation for the difference in response, although it is likely that surface roughness or gold domain orientation have a role in determining the characteristic

response of each surface. In similar work, Bowden *et al.*[111] strongly recommend the use of sputtered (in preference to evaporated) gold; while careful substrate annealing[50] is a recommended procedure in the preparation of high quality thiol monolayers. It is apparent that a better understanding of all aspects involved in sensor fabrication, ranging from preparation of the gold surface to protein immobilisation, is required to support the further development of this class of superoxide sensor.

3.1.3.4.3 Superoxide Measurement: Stimulated Human Neutrophils

Figure 3.14 presents the response of both macroscopic and evaporated gold to superoxide generated by activated human neutrophils. After allowing for the initial mixing process, the dependence on cell concentration is evident. A similar and more comprehensive study[96] has demonstrated a linear relationship between cell concentration and rate of superoxide production down to cell concentrations as low as 500cell ml^{-1}. Again, as discussed in section 3.1.3.4.2, the response of the evaporated gold electrode is significantly lower than that seen for the macroscopic gold electrode.

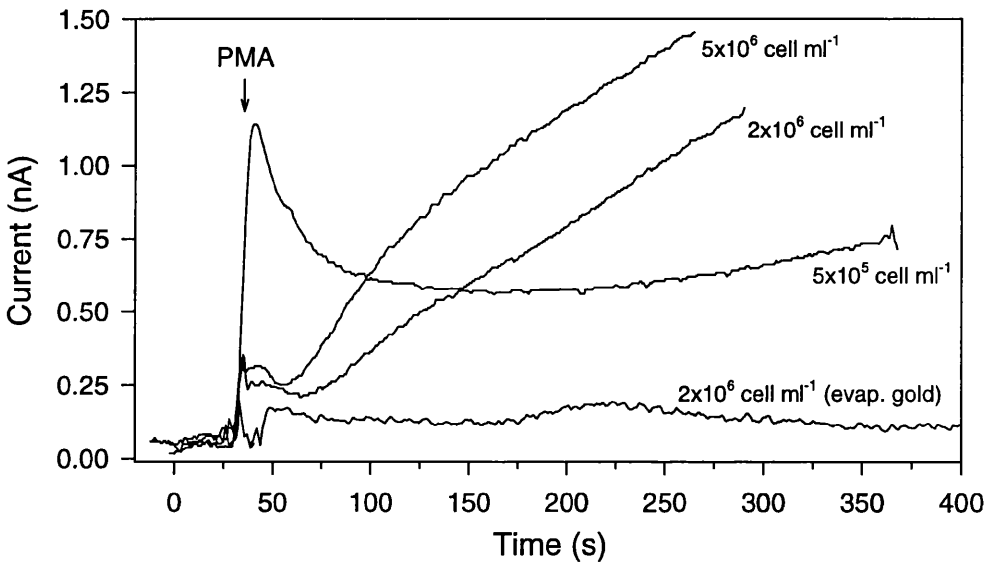

Figure 3.14: A current *vs.* time plot comparing the superoxide response at range of neutrophil concentrations for both macroscopic and an evaporated gold 2mm diameter disc electrodes activated using the procedure described in section 3.1.2. The working electrode was poised at +100mV *vs.* Ag/AgCl in PBS (pH 7.4). Superoxide generation was initiated by the addition of PMA to a final concentration of 0.5μM. N.B. the time axes of all the plots in the above figure have been adjusted so that the PMA additions coincide for all four traces.

The result in figure 3.14 demonstrates the use of the sensor for detecting the release of superoxide from human neutrophils. The durability of the sensor was poor (*ca.* 6 hours), the major determinant being the time spent in cellular solution, a factor almost certainly related to the blocking of the working electrode by the adsorption of cells and cellular proteins. In comparison, an equivalent sensor used solely in hypoxanthine/XOx solutions had a lifetime of

over 24 hours. Sensor storage at 4°C between measurements is recommended to preserve the integrity of the immobilised protein.

3.2 Chemiluminescence

The simplicity and speed of the chemiluminescent assay provided a valuable technique for the rapid analysis of superoxide release from human neutrophils. The technique was not only used as a control, demonstrating that stimulated neutrophils produced superoxide, but also provided a valuable tool for comparing experimental parameters such as: cell concentration, chemotactic stimulant and buffer type.

3.2.1 Theory: Chemiluminescence

Luminescence is the emission of light from atoms or molecules as a result of a transition from an electronically excited state to a lower energy state.[12] In chemiluminescence, the excited states are created by a chemical reaction. A familiar example is the luciferase enzyme based chemiluminescence exhibited by the firefly.[116] A number of synthetic compounds including luminol, luminol derivatives, and lucigenin exist which chemiluminesce in an oxidising environment.

A chemiluminescent assay is a common method for detecting the release of superoxide and other reactive oxygen species[3] (ROS). While not specific for superoxide, chemiluminescent assays have been shown to correlate well with more specific photometric assays for superoxide release based upon the reduction of cytochrome *c* in solution[117] A luminol based chemiluminescent assay is described by the following reaction:

$$\text{Luminol} + \text{ROS} \longrightarrow \text{Aminophthalate} + N_2 + h\upsilon \qquad (3.6)$$

The reaction has a low quantum yield in comparison to the 'firefly' reaction but the yield can be improved in alkaline conditions.

3.2.2 Methods & Materials: Chemiluminescence

Superoxide release was assessed by luminol enhanced chemiluminescence using a LKB 1251 Luminescence Photometer (Luminometry; LKB). The luminometer was controlled by a BBC Archimedes computer. Superoxide was generated by the metabolic activation of neutrophils or as a component ROS generated from the xanthine or hypoxanthine/XOx reaction. Neutrophils were prepared in PBS according to the procedure described in section 4.2.4.2, used over a period

[3] Other ROS include hydrogen peroxide, peroxide radicals and singlet oxygen.[16]

of up to four hours, and stored on ice between experiments. Neutrophils and luminol were used at a range of concentrations and the values are quoted adjacent to the corresponding results.

The chemotactic factors PMA and N-formylmethionyl-leucyl-phenylalanine (FMLP) were used to initiate neutrophil activation. These stimulants were used at a range of concentrations. They were initially dissolved in dimethyl sulfoxide (DMSO) at a concentration of 1mM, and then diluted to the appropriate concentration using PBS. The xanthine or hypoxanthine (both 1.5mM) based mechanism was initiated by the addition of XOx at a concentration of 500μg ml^{-1}. For both superoxide generating mechanisms, the control experiments represent the recorded response of the un-activated system. SOD was used at a concentration of 500μg ml^{-1}. All samples were held in UV transparent plastic cuvettes. Sample volume were fixed at 1ml, the final volume was maintained by the addition of PBS. Chemicals were obtained from Sigma/Aldrich and all solutions were dissolved in a PBS stock solution prepared using RO water.

3.2.3 Results and Discussion: Chemiluminescence

The initial experiments were performed with the aim of optimising experimental conditions and characterising the system under study. Both luminol and cell concentration showed a dose dependent response (figure 3.15), as can be assessed from the relative peak response values. While it was possible to obtain a saturated luminol response at close to 20μM, no effort was made to observe a similar saturation with cell concentration. Based upon these initial experiments, a luminol concentration of 10μM and a cell concentration of $5x10^5$cell ml^{-1} was chosen for subsequent experiments. These values primarily reflect the sensitivity constraints of the luminometer; i.e. a significant, but not saturated, response is desirable.

The final component of an electrorotation experiment was the mechanism for stimulating the neutrophils into superoxide production. The pioneering work of Babior[118] developed the use of IgG coated latex beads and subsequent research has identified a range of alternative mechanisms and chemicals.[119-121] In this study, only the chemotactic stimulants PMA and FMLP (a bacterial peptide residue) were investigated. Figure 3.16 provides a comparison of superoxide response of these two stimultants.

From figure 3.16, the durability of the PMA induced response in comparison to that of FMLP is apparent. The 'kink' visible in the FMLP but not the PMA response in frequently observed and has been ascribed to the different mechanism of neutrophil activation. Whilst the FMLP response can be broken down into a physiologically based multi-stage process initiated by its contact with the cell membrane, PMA needs to be transported into the cytoplasm where it directly activates the protein-kinase-C receptor.[44] In recent literature, both stimulants are used

although FMLP is gaining preference, probably due to the improved speed of response and better characterised stimulating mechanism. Although generating a slower response, the durability of the PMA response was a definite asset in subsequent electrorotation experiments (see section 4.3.3.2) and it was adopted as the preferred stimulating mechanism.

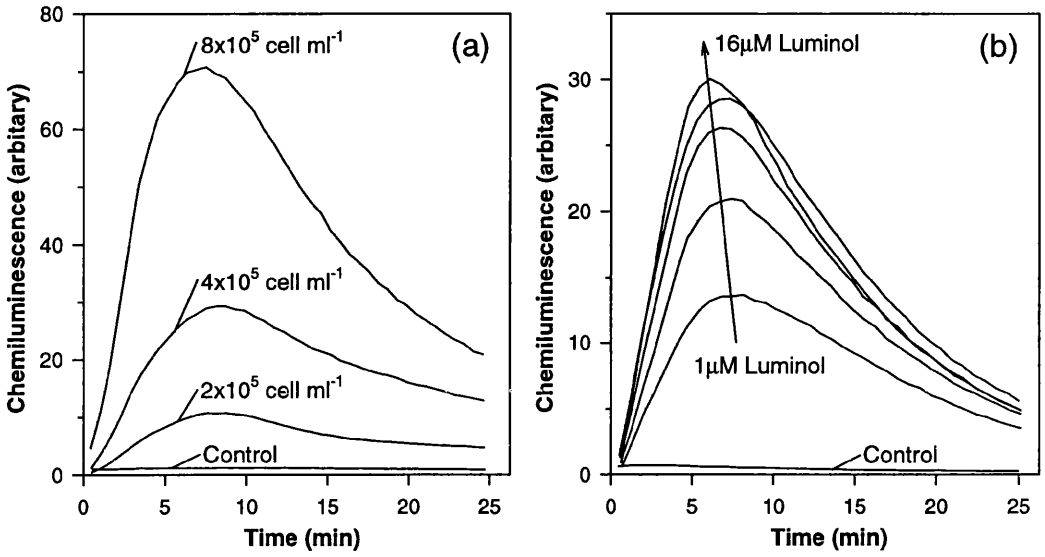

Figure 3.15: The results of control experiments to determine suitable cell (a) and luminol (b) concentrations for subsequent experiments. The luminol concentrations used were 1, 2, 4, 8, 16μM. Neutrophil stimulation for both experiments was with 1μM PMA, see section 3.2.2 for the full experimental protocol.

Analysis of PMA response over a range of concentrations (figure 3.17) indicated a more complex behaviour than seen in the earlier luminol and cell concentration experiments (see figure 3.15). At very low concentrations PMA demonstrated a dose dependent response but obvious mechanistic effects were apparent at higher concentrations. A comparison of peak response magnitude for 1μM and 10μM would suggest that the response remains dose dependent. However, a more rigorous comparison of total areas indicated the responses to be of a similar magnitude. These two concentrations are saturated responses, the nature of the response is almost certainly determined by the rate at which the PMA is transported across the cell membrane into the cytoplasm.[44] Furthermore, a very high concentration (100μM) of PMA produced a reduced response, probably related to the known physiological toxicity of the chemical.[119]

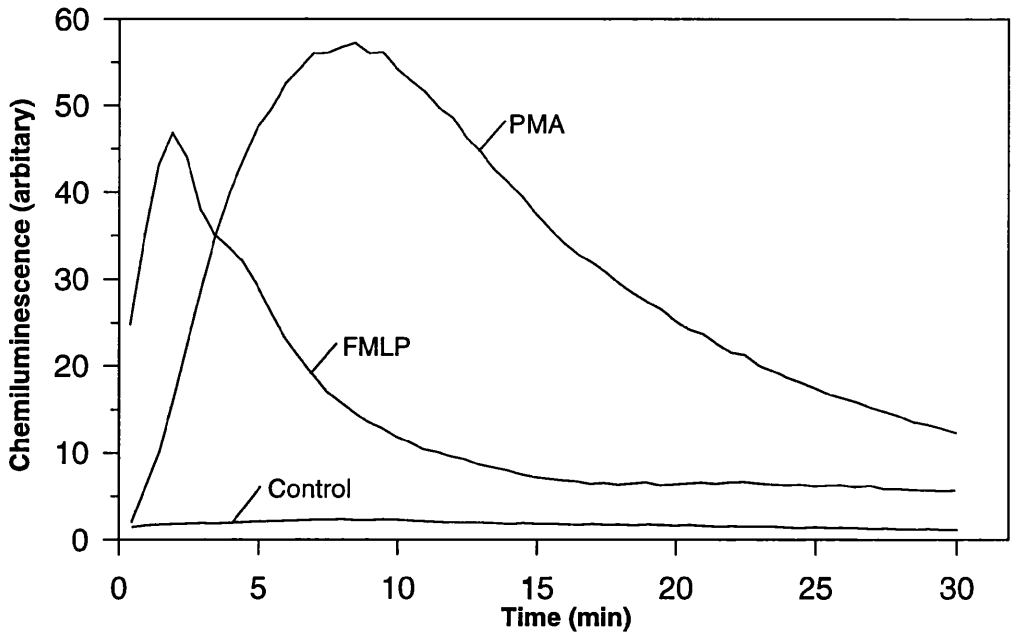

Figure 3.16: A comparison of the chemiluminescence intensity *vs.* time recorded from neutrophils stimulated by PMA (1μM) and FMLP (0.1μM). The cell and luminol concentrations were $5x10^5$cell ml^{-1} and 10μM, respectively.

The specificity of the chemiluminescent assay for superoxide is demonstrated in figure 3.18. If the enzyme SOD is included with the stimulated neutrophils, the response is reduced to a negligible level in comparison to the control (figure 3.18a). From this result it can be concluded that the dominant ROS contributing to the luminol based chemiluminescence is superoxide. This result agrees well with the broad base of research on the mechanisms of neutrophil activation.

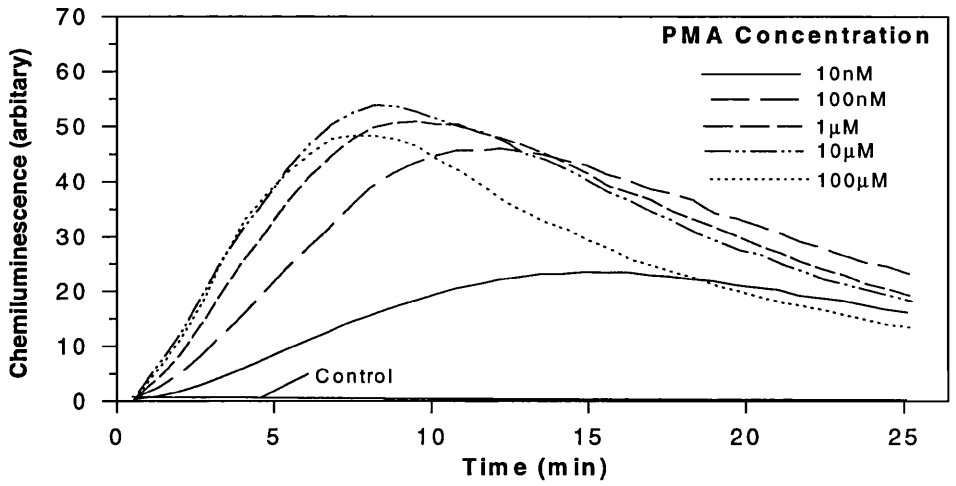

Figure 3.17: A comparison of the superoxide response of stimulated neutrophils at a range of PMA concentrations. The cell and luminol concentrations were $5x10^5$cell ml^{-1} and 10μM, respectively.

Also shown in figure 3.18a is the response for neutrophils prepared in an isotonic sucrose solution (260mM). For comparison, figure 3.18a includes the response of the same cell sample at a similar concentration but in this case prepared in PBS. No significant difference in superoxide generating activity is observed, again, this is a result of relevance to the electrorotation experiments described in section 4.3.3.

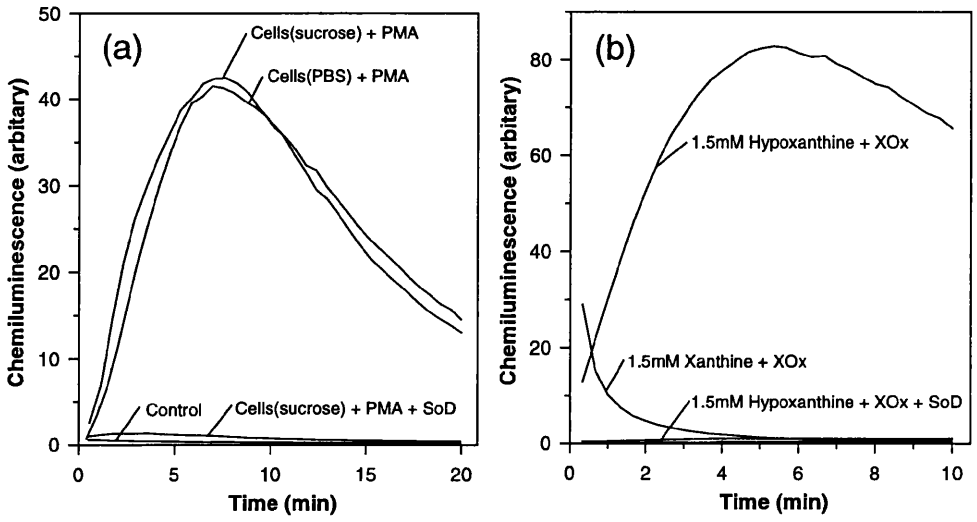

Figure 3.18: (a) The chemiluminescence response for PMA (1μM) stimulated neutrophils in both PBS and isotonic sucrose (260mM) - the use of different buffer solutions produced no significant change in response. The cell and luminol concentrations were $5x10^5$cell ml^{-1} and 10μM respectively. (b) A similar experiment but this time comparing the response of xanthine and hypoxanthine (both 1.5mM) following the addition of 500μg ml^{-1} XOx - hypoxanthine has a more durable response. The luminol concentration was 5μM.

The experimental results presented in figure 3.18b provided corroborative evidence for the differing mechanisms of superoxide generation that can occur using the xanthine or hypoxanthine/XOx systems. The chemistry of this system has been described earlier (see figure 3.11) and from the chemiluminescence data it is suggested that the hypoxanthine reaction is both more durable (i.e. of a slower rate) and generates significantly more superoxide at equivalent molar concentrations. This conclusion cannot be confirmed by chemiluminescence since the rapid initial rate of the xanthine/XOx reaction cannot be accurately recorded and one cannot exclude the possibility of a rapid saturated luminol response at the onset of the xanthine/XOx reaction. However, this result does recommend the preferential use of the hypoxanthine/XOx system in similar superoxide assay experiments.

3.3 Summary

The major topic of this chapter has been the preparation and characterisation of an electrochemical superoxide sensor. In addition, unique aspects applicable to the cleaning and

activating of lithographic electrode structures have been addressed and proven methods described. The procedures associated with the fabrication and testing of microelectrode structures have also been discussed. The scope for further work in this field is rapidly expanding and it is hoped that this work has presented some indication of the many challenges ahead.

To conclude, it is worthwhile to asses the progress toward the project goal of sensing superoxide release form a single cell using cytochrome *c* electrochemistry. Consider the maximal response (*ca.* 5μA, 2mm evaporated gold disc) recorded using the hypoxanthine/XOx superoxide generating mechanism (see figure 3.12). This current magnitude can be compared to the expected current at a micro-ring electrode to be used for detecting the release of superoxide from a single cell (see figure 1.2). For example, assuming a ring width of 10μm and diameter 50μm and similar protein immobilisation conditions, the estimated maximum current using a relative area comparison is *ca.* 3pA. Even accounting for the 'current amplification'[122] effect associated with hemispherical diffusion to microelectrode structures, and the reduction of superoxide dismutation by making measurements close to the source - the maximal current will still be in the low pA range. This estimation is made in relation to a saturated response, the actual currents are likely to be orders of magnitude lower.[123] Hence, to make successful measurements of chemicals released from single cells it is recommended that three specific aspects of the sensor design are improved, these are:

1) ***Protein Immobilisation:*** Based on the methodology described in section 3.1.2, the protein immobilisation procedure could be enhanced by improved thiol immobilisation and gain a better understanding of the protein coupling chemistry.

2) ***Low volume structures:*** An example would be the fabrication of the ring microelectrodes on the bottom of 'pits' in the substrate. The limited volume would improve the sensor sensitivity by confining the diffusion of superoxide.[124]

3) ***Low Current measurement:*** - If currents in the pA range need to be measured, a sensitive multi-potentiostat will be required. The new generation of low input bias current operational amplifiers are exciting developments in this area.

4. Dielectrophoresis

In this project, the aim was to explore the use of dielectrophoresis as a means of non-invasive particle positioning and confinement. The dielectrophoretic response of both polystyrene beads and viable cells were studied, the beads providing 'cell-shaped' models for the initial studies.

4.1 Theory:

Particle confinement and electrorotation are related aspects of the dielectrophoretic phenomenon. Each is described theoretically in the following sections.

4.1.1 Particle Confinement

The dielectrophoretic phenomenon is associated with the field-induced dipole moment of a particle in its surrounding medium. Using the following vectored parameters, it can be shown that for a homogeneous spherical particle in an electric field of strength E, the effective dipole moment $m(\omega)$ and dielectrophoretic force $F(\omega)$ are related as follows:[125,126]

$$m(\omega) = 4\pi\varepsilon_m f\left(\varepsilon_p^*, \varepsilon_m^*\right) R^3 E \tag{4.1}$$

$$F(\omega) = \frac{\mathrm{Re}[m(\omega)]\nabla E_{(RMS)}^2}{2E} \tag{4.2}$$

where R is the radius of the particle, ∇ is the del vector operator, and $f\left(\varepsilon_p^*, \varepsilon_m^*\right)$ is the Clausius-Mossotti factor,[127] represented by:

$$f\left(\varepsilon_p^*, \varepsilon_m^*\right) = \frac{\varepsilon_p^* - \varepsilon_m^*}{\varepsilon_p^* - 2\varepsilon_m^*} \tag{4.3}$$

The parameters ε_p^* and ε_m^* represent the complex permittivities of the particle and the medium respectively, and take the form:

$$\varepsilon_{p/m}^* = \varepsilon_{p/m} - j\sigma_{p/m}/\omega \tag{4.4}$$

where σ is conductivity and j is $\sqrt{-1}$.

Further analysis of equations 4.1, 4.2 and 4.3 yields the Real (Re) and Imaginary (Im) components as follows:

$$\mathrm{Re}\left[f\left(\varepsilon_p^*,\varepsilon_m^*\right)\right]=\frac{\sigma_p-\sigma_m}{\left(1+\omega^2\tau^2\right)\left(\sigma_p+2\sigma_m\right)}+\frac{\omega^2\tau^2\left(\varepsilon_p-\varepsilon_m\right)}{\left(1+\omega^2\tau^2\right)\left(\varepsilon_p+2\varepsilon_m\right)} \tag{4.5}$$

$$\mathrm{Im}\left[f\left(\varepsilon_p^*,\varepsilon_m^*\right)\right]=\frac{3\omega\tau\left(\varepsilon_p\sigma_m-\varepsilon_m\sigma_p\right)}{\left(1+\omega^2\tau^2\right)\left(\sigma_p+2\sigma_m\right)\left(\varepsilon_p+2\varepsilon_m\right)} \tag{4.6}$$

with τ representing the characteristic time constant for a Maxwell-Wagner type dielectric dispersion[128] at the interface of the particle and its surrounding medium.

This theory provides the basis for an analysis of the dielectrophoretic phenomenon. A more detailed model for biological applications would consider the reality that a cell is not a homogenous medium, being typically composed of a cell membrane, cytoplasm, nucleus and vacuoles. However, this simple model does allow one to make some useful initial observations on the phenomenon. From equation 4.2 it can be seen that $F(\omega\ \ )$ is primarily dependent on the real component of the Clausius-Mossotti factor $(f(\varepsilon_p^*,\varepsilon_m^*))$, and is independent of electrode polarity due to the dependence on $E^2_{(RMS)}$ and hence will be apparent in both d.c. and a.c. fields.

It can be seen from equation 4.5 that the dielectrophoretic force is sensitive to frequency ($f=\omega/2\pi$). At low frequencies (where $\omega > 0$), the most significant parameters are the relative conductivities of the particle and its surrounding medium. However, at high frequencies (where ω approaches ∞), the influence of the relative permittivities becomes dominant. Hence the polarisability of a particle in the particular medium determines the nature, be it positive or negative, of the dielectrophoretic force acting upon it.

In the use of dielectrophoresis for the manipulation of cells, the variation of frequency provides the most flexible means of control. As a broad guide, at frequencies below 1kHz the response is dominated by membrane surface charge effects. In the range up to 100kHz the effective conductivity of the cell membrane has a controlling influence. Whilst at higher frequencies the dielectric properties of the cell interior are most apparent.[129]

4.1.2 Electrorotation

Electrorotation occurs as a result of the induced torque exerted on particles in rotating electric fields. The vectored frequency dependent torque ($\Gamma(\omega)$) is related to effective dipole moment (see equation 4.1) as follows:[125,126]

$$\Gamma(\omega) = -\mathrm{Im}(m(\omega))E \tag{4.7}$$

The nature of the observed electrorotation is determined by the Imaginary component of the Clausius-Mossotti factor (see equation 4.6). It is dependent on the relative conductivities and permittivities of the suspension medium and particle, the applied field, and frequency. When the $\mathrm{Im}(f(\varepsilon_p^*, \varepsilon_m^*)) > 0$, the induced dipole lags behind the applied field by less than half a period and an anti-field rotational torque is exerted on the particle. Conversely, when $\mathrm{Im}(f(\varepsilon_p^*, \varepsilon_m^*)) < 0$ the induced dipole moment lags by greater than half a period and co-field torque is exerted (see figure 4.1).

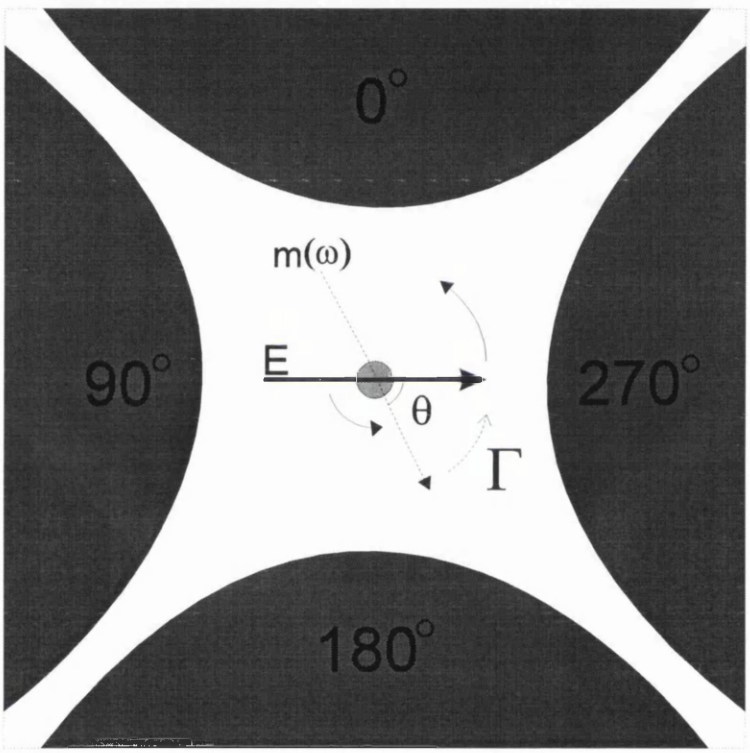

Figure 4.1: The induced dipole moment of a particle is out of phase with the direction of the electric field. The angle between the two (θ) reflects the time taken for the dipole to form. The phase difference will generate a variable torque (Γ) acting on the particle causing it to rotate. Co-field rotation will occur if the angle is less than 180°, anti-field rotation will occur if the angle is greater than 180°.

The nature of observed rotation rate ($R(\omega)$) is the resultant force balance between the torque and the viscous forces acting on the particle in a particular medium, defined as:[129]

$$R(\omega) = -\frac{\varepsilon_m E^2}{2\eta}\mathrm{Im}(f(\varepsilon_p^*, \varepsilon_m^*)) \tag{4.8}$$

where η is the dynamic medium viscosity. Since the field is applied by a phase shifted voltage, $R(\omega)$ can be also be expressed as:

$$R(\omega) = -\frac{\varepsilon_m k^2 V^2}{2\eta} \mathrm{Im}(f(\varepsilon_p^*, \varepsilon_m^*)) \qquad (4.9)$$

where k is a constant relating the applied RMS voltage, electrode geometry and particle position.

In practice, the electrorotation of viable cells follows a characteristic pattern. At low frequencies (<1MHz), the majority of the electric field voltage is distributed across the cell membrane and the cell behaves as a poorly conducting sphere, and anti-field rotation is observed. At higher frequencies (>1MHz), the applied field permeates the membrane and the rotational response is dominated by the dielectric properties of the conductive cellular interior, and co-field rotation is observed. Changes in cell physiology and the influence of cell organelles will be reflected in the speed and sense of the electrorotation.[130] Data on the frequency dependent changes in response (i.e. an electrorotational spectrum) can be interpreted to provide values for specific cellular parameters, for example, in determining the membrane capacitance and the cytoplasm conductivity of lymphocytes.[131] The models used in this study for the interpretation of electrorotational spectra are discussed in Appendix A.

4.2 Methods & Materials

This section describes the procedures used in the particle confinement and electrorotational experiments. In addition, the methods of media preparation, particle purification and electrode fabrication are described.

4.2.1 Suspension Media

All aqueous media used in this study were prepared using RO water, the conductivity being adjusted using additions of PBS. Solution conductivity was measured at 20°C on a Hewlett Packard (HP) 4192A Impedance Analyser using a platinum black electrode. Conductivity measurements were made at 100kHz, a frequency high enough to avoid any effects of electrode polarisation.[132] A stock solution of a sucrose (260mM) was used for all cell suspensions. This medium has the equivalent osmotic pressure (osmolarity) to physiological saline (300mosmol kg^{-1}). Use of sucrose, or similar sugars, provides a means of maintaining cell viability over a range of solution conductivities.

A important consideration for the electrorotational work was to ensure that the media selected did not contribute to the activation mechanism of neutrophils. Alternative media such as glucose[133] and mannitol[18] solutions were avoided for this reason. Furthermore, a salt solution free of divalent ions was chosen in preference to a simple culture media, as it has been shown that Ca^{2+} and Mg^{2+} ions can contribute to the undesirable aggregation of neutrophils during the purification procedure.[134]

4.2.2 Electrodes and Instrumentation

Electrodes were designed using the Wavemaker (Barnard Microsystems Ltd., UK) circuit design package and fabricated using photolithography and lift-off (see section 2.1). Circular and polynomial electrode arrays (figure 4.2) of varying tip-to-tip distance were used in this study. The simple circular array was satisfactory for generating the non-uniform field necessary for particle confinement. The polynomial electrode design of Huang *et al.*[135] is best suited to the work on particle electrorotation.[136] Glass was selected as a good flat substrate material that also provided the transparency necessary for inverted light microscopy.

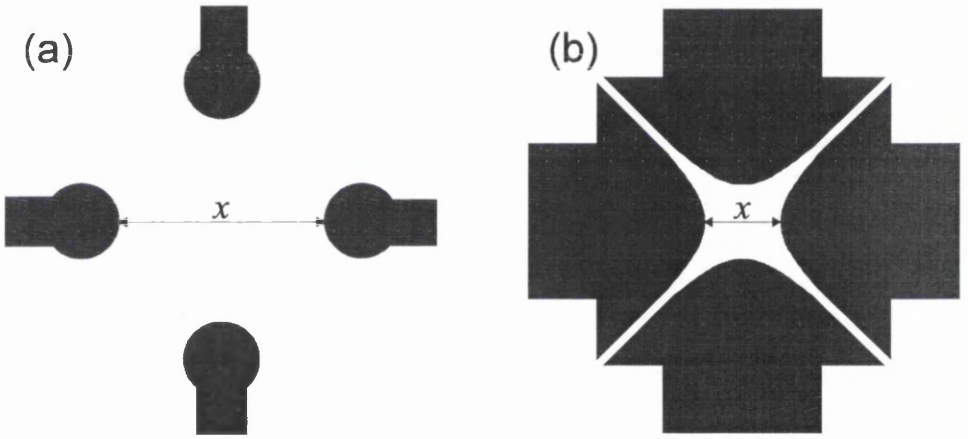

Figure 4.2: The circular (a) and polynomial (b) electrode geometries of varying tip-to-tip separation (x) used in this study. Both geometries were suitable for particle trapping experiments (x=15-100μm). A wider polynomial array was best for the electrorotation studies (x=360μm).

The electrodes were made by e-beam evaporation of a Ti/Pd/Au (10/10/10nm) multilayer metal structure, which provided both an adherent and inert electrode structure (see section 2.2.1). Noble metal electrode are preferred as they exhibit a higher oxidation potential in aqueous solutions. Care is required when working at low frequencies because the time averaged d.c. component of the voltage signal can lead to electrolysis at the electrodes. The likelihood of electrolysis, and subsequent damage of the electrode structure, is enhanced by higher conductivity media and high field strengths (i.e. high potential and/or small electrode separation).

Observations of the dielectrophoresis phenomenon were made on a Nikon Microspot light microscope using both reflected and transmitted light. Phase contrast imaging helped to highlight particle profiles. The sinusoidal electric fields (1Hz-20MHz, 0-12V) were generated using a direct digital synthesis generator designed in the department (design no.: GUED 1101) and controlled by a software written in Borland Turbo Pascal running on an IBM PC.

4.2.3 Bead Preparation

Polystyrene beads of average diameter 6μm were obtained form Polyscience Inc., USA. The beads were thoroughly washed before use to remove any contaminants in the original bead suspension (3 centrifugal washes in RO water). The washed beads were then re-suspended in sucrose (260mM). A 100 times dilution of the original suspension provided a suitable concentration ($2x10^5$beads ml^{-1}) for particle confinement, a lower concentration ($5x10^4$beads ml^{-1}) was used in the electrorotational experiments.

4.2.4 Cell Preparation

Numerous cell types were used in this study, including: Baby Hamster Kidney (BHK) cells and a range of blood cells (neutrophils, lymphocytes and erythrocytes) separated from both human and rabbit blood. All cells were suspended in isotonic sucrose solutions of adjusted conductivity.

4.2.4.1 BHK Preparation

The BHK cell line is immortal and can be maintained by 'passaging' at 3-4 day intervals. In suspension, these cells have are spherical shape with a radius of 4-5μm. In preparation for dielectrophoretic experiments, the cells were detached from the base of the culture flask using trypsin-versin (a digester of the adherent proteins) and thoroughly washed in sucrose.

4.2.4.2 Blood Purification

This section describes the procedure for the separation of neutrophils and lymphocytes from a sample of whole blood. The procedure is based on that of Chettibi *et al.*[137] Human blood was obtained from the Glasgow Royal Infirmary Hospital, and rabbit blood was obtained form Sapu(Carluke, UK). In some cases, 'buffy coat' was obtained from the Blood Transfusion Service (Glasgow) and diluted in a 1:1 ratio with PBS before separation. Buffy coat is the residual component following the centrufugation of whole blood to remove the plasma and erythrocytes fractions required for hospital use. All samples were screened for HIV and hepatitis B and all separation procedures were conducted in a Class 2 biological grade fume hood.

An erythrocyte sample was prepared by the simple dilution of whole blood. This sample was of satisfactory purity, since 99% of blood cells are erythrocytes. However, separation of

neutrophils and lymphocytes first required the removal of the erythrocytes using dextran sedimentation. The first step of the procedure is to mix a dextran solution (5% in PBS) with the blood at a 1:10 ratio. The dextran dramatically increases the sedimentation rate of erythrocytes by selectively bonding to the cell walls. This step takes approximately 30 minutes and leaves a supernatant rich in neutrophils and lymphocytes.

The next step is the centrifugal separation of the remaining components using a Ficoll (Histopaque 1077, Sigma) density gradient. The details of the procedure are illustrated in figure 4.3. The residual plasma and supernatant fractions can be discarded. The lymphocyte fraction is of high purity, and following the appropriate washing and conductivity adjustments, is ready for use in dielectrophoretic experiments. However, the neutrophils fraction is frequently contaminated with residual erythrocytes. These can be removed by rapid (20s) hypotonic lysis in RO water, which generates enough osmotic pressure to rupture the cell membrane of the erythrocytes. The stronger membrane of neutrophils remains intact during this procedure, although it has been suggested that this procedure does partially activate or 'prime' the neutrophils[120] and may initiate a degree of neutrophil aggregation.[138] The cell lysis step is halted by excess (>10 times) dilution with PBS and the residual neutrophils can be removed by centrifugal washing.

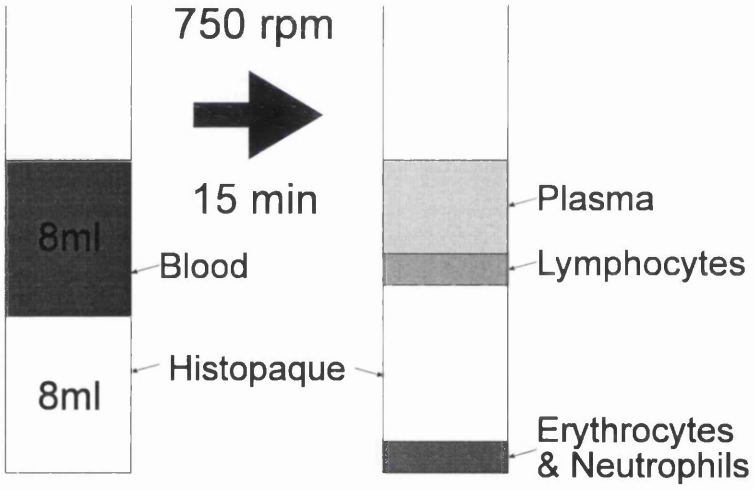

Figure 4.3: A summary of the procedure used to separate lymphocytes and neutrophils. Initially, the supernatant of the dextran sedimentation step is carefully layered onto the Histopaque. Under centrifugation the denser neutrophils and erythrocytes pass through the Histopaque and collect at the bottom of the tube. The lymphocytes remain above the Histopaque layer.

Cell viability was determined using the 'trypan blue' exclusion test,[139] typical values were in the range 95-98%. Cell concentrations were measured using a haemocytometer. A concentration of $5x10^4$cells ml^{-1} was suitable for electrorotation experiments, while the higher concentration of $2x10^5$cells ml^{-1} was optimal for the cell confinement experiments.

4.2.5 Collection of Electrorotational Spectra

In preparation for collection of spectra, the electrode structure was soaked in casein solution (1mg ml^{-1}) for 15 minutes. The adsorbed milk protein provides a layer that reduces the rate of particle adhesion to the electrode structure. The mechanism of cellular adhesion is particularly apparent in neutrophils and is associated with the high motility and subsequent activation of these cells.[119] A sample of cell suspension (*ca.* 800µl) was contained above the electrodes in a 2mm tall and 20mm diameter glass ring attached to the substrate using a thin layer of silicon grease. Increases in conductivity due to evaporation were reduced to a negligible level by covering the glass ring with a cover slip.

Electrorotational spectra were collected by observing the rotation rate and sense at 4 points per frequency decade. In addition, a greater amount of rotation data was collected near the inflexion and cross-over frequencies within the spectra. The experimental observations were made by recording the rotation of the cells on video followed by later analysis of determine the rotation speed (ω) in rad s^{-1}. Each of the recorded spectral points represent the average of six measurements on particles of similar diameter.

Induced dipoles in nearby rotating particles can affect the rotational response. To minimise this influence, recordings were made from particles separated by at least three cell diameters.[129] In addition, recordings were only made of particles positioned in a area defined by a circle located at the centre of the electrode array. This 'virtual' circle had a width of $0.3x$, where x represents the separation between the electrode tips. For the polynomial electrode design used in these electrorotational experiments, Hughes *et al.*[136] have shown that particles in this region experience a consistent (95% confidence) rotational torque and minimal positive dielectrophoretic forces.

4.2.5.1 Activation of Neutrophils

Neutrophils were activated by the addition of chemotactic factors[136] such as PMA or the bacterial peptide FMLP. Both stimulants were first dissolved in DMSO and then diluted to a concentration of 500µg ml^{-1} in sucrose/PBS solution of the same conductivity and osmolarity as the cell suspension. Once the spectrum of the resting neutrophils had been collected a 40µl aliquot (i.e. a *ca.* 20 times dilution) of chemotactic factor was added to the cell suspension. The suspension was left for 60 seconds before collection of the spectrum of the activated neutrophils.

Neutrophils are extremely sensitive to both these chemotactic stimulants, concentrations as low at 10nM can generate a response.[44] In the central concentration range (i.e. 50nM to 1µM) a dose dependent response has been observed, as demonstrated by the generation of free radicals (see section 3.2.3). These can be measured by techniques such as chemiluminescence[140] and

cytochrome *c* reduction.[117] The final chemotactic factor concentration (25μM) used in this study was chosen specifically to give a rapid saturated response. PMA was preferred to FMLP since PMA is known to provide a more consistent and durable chemotactic response in neutrophils.[140] Control experiments ensured that the addition of DMSO alone did not contribute to the observed response.

4.3 Results and Discussion

The results of the particle confinement and electrorotation experiments will be discussed separately in this section. The electrical properties of the medium are of relevant to both aspects of the dielectrophoretic phenomenon and the results will be detailed below.

4.3.1 Medium Conductivity and Permittivity

Medium conductivity and permittivity are crucial parameters in experiments exploiting the phenomenon of dielectrophoresis. Aqueous salt (0-200mM PBS) and sucrose (0-270mM) solutions were used in this study. At these concentrations, the solution permittivity remains constant ($79\varepsilon_0$)[141] over the available frequency ranges (100Hz-20MHz). However, the same is not true for ionic conductivity. The movement of aqueous ions is the mechanism of charge transfer in solutions, and is very sensitive to changes in concentration.

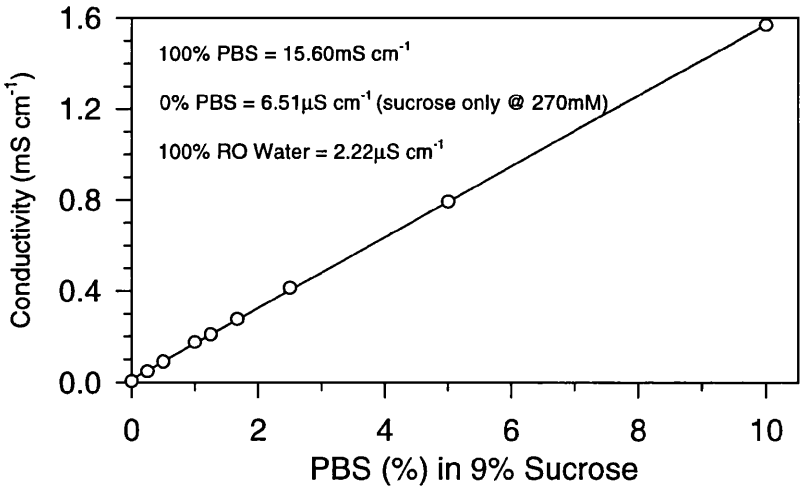

Figure 4.4: The variation in conductivity of mixed PBS/sucrose solutions used as suspension media in the dielectrophoresis experiments. Conductivity was measured with a HP 4192A Impedance Analyser using a platinum black electrode (cell constant=0.96cm^{-1}) at 100kHz. The linear variation demonstrates the predominant effect of PBS concentration on the conductivity of the medium.

Figure 4.4 demonstrates the predominant effect of PBS on the conductivity of mixed PBS/sucrose solutions. This data provided a guide to the preparation of stock solutions. The conductivity values quoted in the text represent those values measured after the addition of cells at the required concentration.

4.3.2 Particle Confinement

The work on particle confinement concentrated on the use of the dielectrophoretic phenomenon to generate electric field traps for single particles. The procedure relies on the use of negative dielectrophoresis to induce a translational force on the particle. This moves and retains it at the position of minimum potential energy (see figure 1.6).

The results presented below provide a guide to the experimental conditions necessary to trap polystyrene beads and cells. It is primarily a qualitative analysis to see if the particle was successfully trapped and to identify the experimental conditions. Quantitative studies to measure the dielectrophoretic force include: the measurement of average velocity of yeast cells[40] and the use of particle levitation.[39] In this study, under microscopic observation, it was evident when a single particle was trapped, as it ceased to be sensitive to the characteristic convection current drift and Brownian motion of other particles in solution. However, an indication of the quality of the field trap could be deduced from the speed with which the particles were confined. Any particle levitation was indicated by the de-focusing of the microscope image.

4.3.2.1 Polystyrene Beads

Successful confinement of polystyrene beads was particularly dependent on the conductivity of the suspending medium. At a medium conductivity of 200-2000μS cm^{-1} (1.2-12.5% PBS), it proved simple to trap a single bead (figure 4.5a) over a broad range of frequencies (10kHz-20MHz). At lower conductivities (e.g. <100μS cm^{-1}, <0.6% PBS), successful trapping proved impossible, since the positive dielectrophoretic force (i.e. attraction of beads to the electrode edges) was dominant. However, at higher frequencies (>1MHz) and higher conductivities (i.e. *ca.* 100μS cm^{-1}), a weak negative dielectrophoretic force was apparent. When using very high conductivity solutions (>2000μS cm^{-1}), the negative dielectrophoretic force was acting over the entire frequency range. The action of this force was evident from the obvious repulsion of beads from the electrode edges. Nevertheless, stable particle confinement was difficult to control, most probably due to ohmic heating of the solution (see section 4.3.2.3 for further discussion).

One difficulty encountered in similar studies has been sedimentation and adhesion of particles to the substrate. The increase in medium viscosity by the use of sucrose (9%) provided a satisfactory solution but also reduced the responsiveness of beads to changes in the dielectrophoretic force. Other possible compromises, such as substrate silanisation,[127] use of even higher solution concentrations and the inversion of the measurement chamber[39] failed to provide a comprehensive solution to this dilemma. Stubbornly adherent beads could be

released by washing in concentrated detergent (Decon 90). However, the best method to maintain a clean substrate was to prevent it from drying-out.

4.3.2.2 Cells

In contrast to polystyrene beads, the response of cells is more complex due to the influence of the cell membrane and cytoplasm contents (see appendix A). For particle trapping, all cell types behaved in a broadly similar manner and will be treated as a one group in the following analysis.

A minor experimental change was recommended for work with erythrocytes.[142] The concentration of the stock sucrose solution was adjusted to 220mM in order to reduce the solution osmolarity (see also section 4.2.1). The concentration change generated the necessary osmotic pressure to force the naturally biconcave erythrocytes into a more suitable spherical shape.

In some respects, the response of cells is similar to that of beads. For example, cell or bead trapping was less successful at high conductivities (>1000μS cm^{-1}, 6.5% PBS). At low conductivities (6μS cm^{-1} (0% PBS)), a positive dielectrophoretic force was dominant at all frequencies (1kHz- 20MHz), which attracted cells to the electrode edges. To generate a satisfactory negative dielectrophoretic force to confine the particle, the medium conductivity needed to be adjusted into the range 100-1000μS cm^{-1}. A conductivity of 400μS cm^{-1} (2.4% PBS) provided a value suitable for all the cell types used in this study.

Even when using a medium of optimal conductivity, the nature of the dielectrophoretic force was still highly frequency dependent. A strong negative trapping force was apparent at low frequencies (5kHz-150kHz). However, at higher frequencies (150kHz-20MHz) the positive dielectrophoretic became dominant. A similar response for pollen cells has been observed by Fuhr *et al.*[39] at a conductivity of 250μS cm^{-1}.

The positive dielectrophoretic force at high frequency was theoretically predicted by Foster *et al.*,[126] in addition, the modelling also indicates another region of negative dielectrophoretic force at very high frequency. Interestingly, Fuhr *et al.*[39] have managed to demonstrate the use of this high frequency region and have investigated its advantages. They claim that it is superior for particle trapping since the higher frequency voltage will reduce any electric field induced physiological stress generated across the cell membrane.

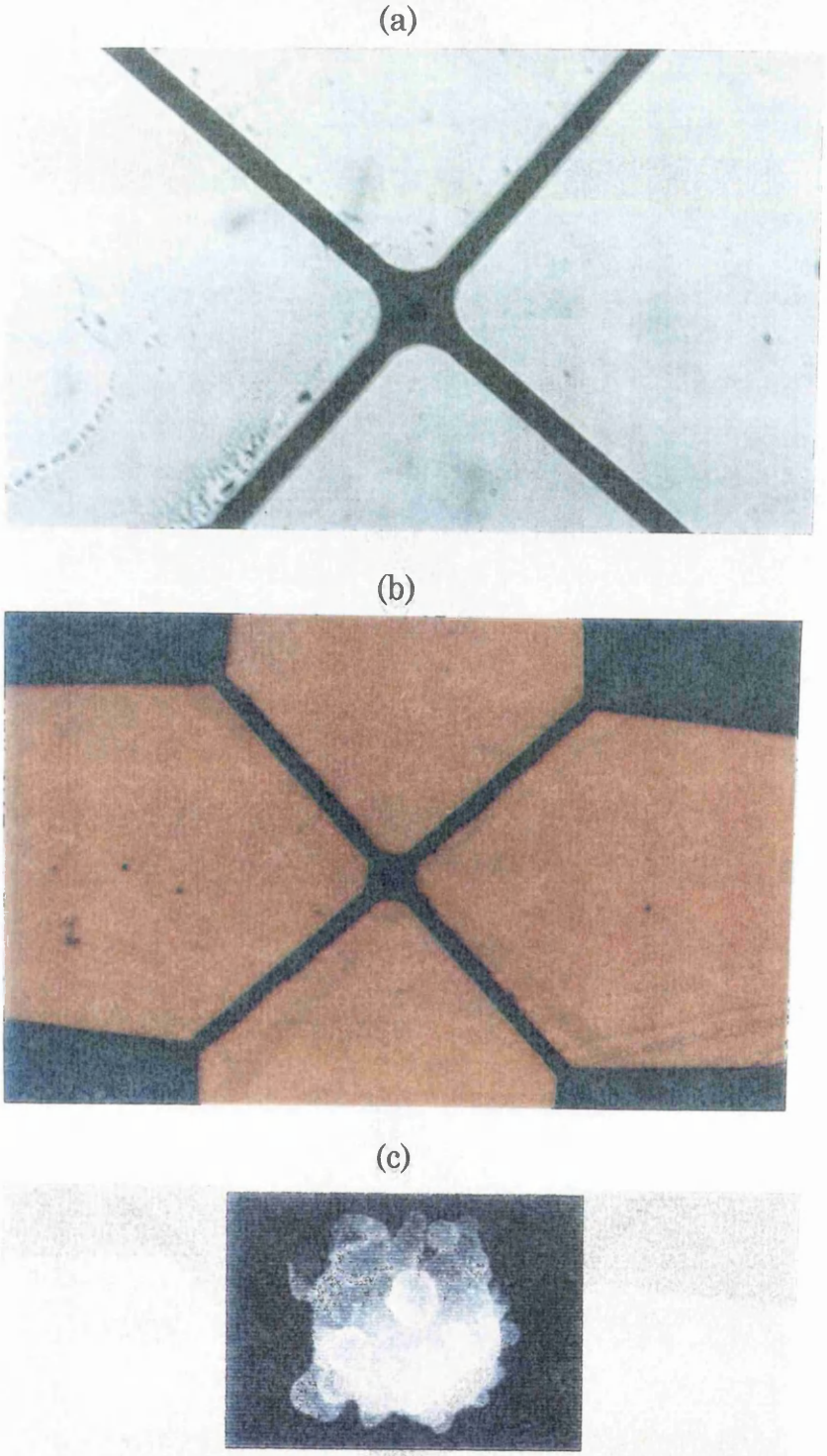

Figure 4.5: Confinement of single particles using negative dielectrophoresis. The polystyrene bead (a) is trapped at the centre of a polynomial electrode array (20μm tip separation), the experimental conditions are 10MHz, 5V p-p, 260mM sucrose/PBS medium (1.2% PBS, 200μS cm^{-1}). The BHK cell (b) is trapped in the same electrode array, the experimental conditions are 50kHz, 1V p-p voltage in an isotonic sucrose/PBS medium (2.4% PBS, 400μS cm^{-1}). (c) Bleb formation and membrane roughening on the surface of activated human neutrophils. *Reproduced from the work of* Watts *et al.*,[149] see section 4.3.3.2.

The highest frequency available in this study was 20MHz and at this frequency a positive dielectrophoretic force was still apparent. For the human neutrophil, these experimental observations concur with the theoretical predictions provided by the double-shell model described in appendix A. Figure 4.6 illustrates the variation in the real component of the Clausius Mossotti factor with frequency for a neutrophil over a broad range of medium conductivities (see table 4.1 for details of the modelling parameters).

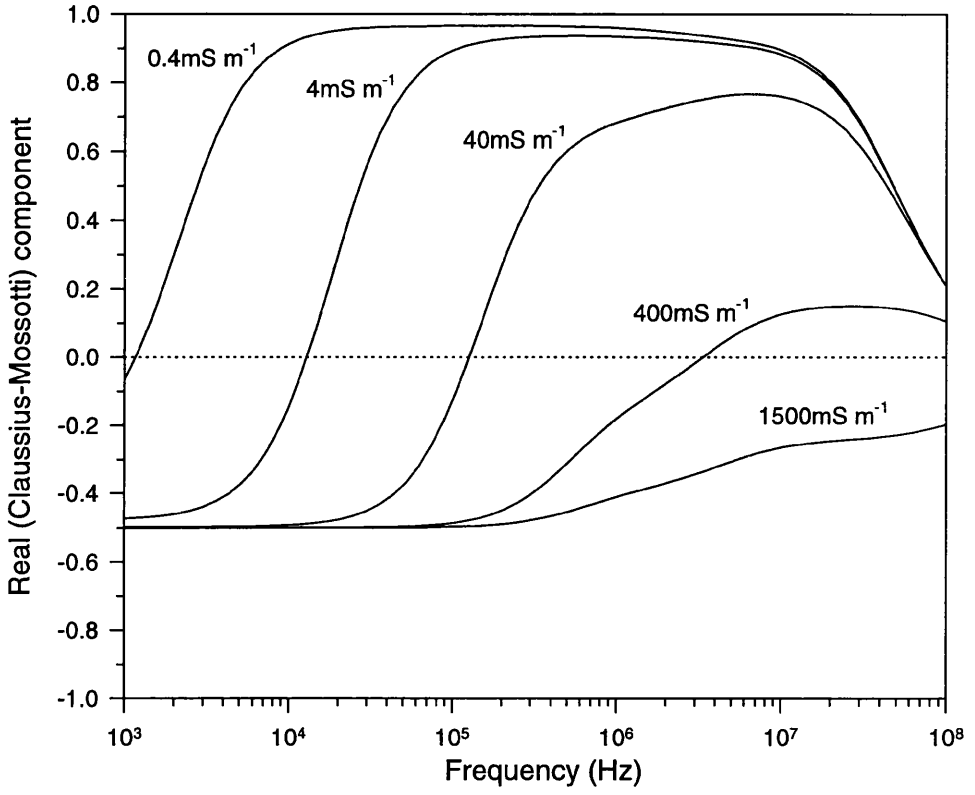

Figure 4.6: The application of the double shell model to the simulation of the dielectrophoretic response of human neutrophils in a range of medium conductivities. The variation in the real element of the Clausius-Mossotti factor provides a guide to the nature of the dielectrophoretic force. A negative value, for a particular frequency, indicates a repulsive force away from the electrodes and the possibility of particle confinement.

From equation 4.2 it can be seen that $\mathrm{Re}(f(\varepsilon_p^*,\varepsilon_m^*))$ is the dominant factor in determining the direction of the dielectrophoretic force. The double-shell model predicts the observed variation in the nature of the dielectrophoretic force at low and medium conductivities. However, at high conductivities (e.g. 1500mS m^{-1} in figure 4.6), theory predicts a negative dielectrophoretic force over the entire frequency range, but this result could not be exploited experimentally. In this study, only poor quality cell trapping was possible at high conductivities. Cells were seen to be repelled away from the electrode edges by a negative dielectrophoretic force. However, it was

difficult to retain any cells within the electric field minimum. Occasionally, a single cell remained in unstable motion within the field trap, but after a short period (1-60sec), the cell escaped into the bulk solution.

A probable explanation for this anomalous behaviour (also seen for polystyrene beads) is ohmic heating of the suspension medium - an effect associated with high conductivity media. Heating effects are created as electrical power is dissipated between the electrodes in the array. It has been shown[144] that the associated temperature rise is linearly related to medium conductivity and can in some cases lead to dramatic local temperature increases. The changes to solution dielectric parameters and the convection currents generated by this local heating account for the unstable motion and poor retention of cells within field traps created in high conductivity media.[145] Fuhr *et al.*[144] use a three dimensional electrode array to create an enclosed field trap. This method overcomes the weakness of two dimensional traps that rely on sedimentation forces to retain the particle. However, the fabrication of three dimensional structures dramatically increase the complexity of any particle trapping application.

4.3.2.3 Further Observations on Particle Confinement

At this point, it is worthwhile to make additional observations on the experimental subtleties of using the phenomenon and it scope for use in similar applications.

4.3.2.3.1 Insulator Layers

Since the phenomenon is based on generation of electric fields, the electrode arrays can be covered in a limited thickness of insulator and still generate the necessary field traps. Under similar experimental conditions as described above, cells and beads were trapped successfully in the array shown in figure 4.5. However, in this instance, the arrays were coated in silicon nitride (see section 2.1.5.2 for details) at a thickness of 50, 110, 240, or 520nm. At a thickness of 520nm, the electrical shielding provided by the silicon nitride was enough to disrupt the field pattern to prevent successful particle confinement at any frequency, even when potentials were increased to the maximum of 12V. This is a valuable result in terms of the design of microfabricated sensors exploiting dielectrophoresis. The use of a thin insulating layer provides the option of multilayer fabrication and will also reduce the magnitude of electrical noise that reaches additional electrodes included with sensor structure. In addition, use of an insulator will reduce the solution heating effects prevalent in high conductivity media.

4.3.2.3.2 Electrode Geometry

For particle trapping, no obvious advantage was seen by use of either the circular or polynomial electrode geometries. However, the electrode tip to tip separation in relation to cell diameter was identified as an important factor. This was particularly apparent if the separation was too narrow and the cell was unable to rest firmly within the electric field trap. It is recommended that the trap should be no smaller than 2 times the cell diameter. The maximum separation is

a more flexible parameter and will depend on a range of factors, such as the required position accuracy, cell viability, and available instrumentation.

If positional accuracy is of paramount importance, a separation of *ca.* 3 times the cell diameter is recommended. This relative geometry provides a suitable steep sided field trap ideal for the confinement of single particles.

The influence of electric fields on cell viability is a difficult matter to assess. However, it would be prudent to minimise the field strength whenever possible so as to minimise the perturbations induced in the intrinsic membrane potential of the confined cells.[39] One of the simplest ways to achieve this aim is to increase electrode separation. Using the method of Wang *et al.*,[129] a reasonable estimation of the typical field strength used in this study was 500V cm^{-1}. Significantly, and of related interest, is the work by Fuhr *et al.*[146] which indicates the negligible effect of even higher field strengths (1000V cm^{-1}) on the life-cycle of mouse fibroblasts.

An obvious constraint of electrode geometries is the instrumentation available. This was demonstrated in this study by the inability to observe any satisfactory high frequency (i.e. >20MHz) negative dielectrophoresis. From equation 4.2 it is clear that the applied voltage will have a dramatic effect (squared relationship) on the nature of the dielectrophoretic force. Similar particle trapping conditions can be generated at two electrode arrays of the same basic design. For example, if the voltage is doubled, a similar dielectrophoretic force can be generated in an array of four times the tip-to-tip separation.

4.3.3 Electrorotation

Detailed electrorotational studies were performed on polystyrene beads and human neutrophils. These particles demonstrated markedly different rotational characteristics. The aim of the work with the beads was to provide a grounding to the subsequent novel work on neutrophils. From the range of cell types available, neutrophils were selected because they are known to have a rapid and dramatic physical and chemical responses to chemotactic stimulation. Human rather than rabbit neutrophils were chosen for their greater availability, increased activity, larger size, and more extensive background literature.

4.3.3.1 Polystyrene Beads

The rotational spectra for the beads was collected in a 260mM sucrose solution (6.51μS cm^{-1}). The spectrum is shown in figure 4.7. There is the suggestion of a co-field rotation peak at low frequency (<1kHz) and there is complete peak centred at 400kHz. This spectrum is similar to previous work on inanimate particles.[37,127] However, in those studies, spectra were collected from particles suspended in salt solutions not containing sucrose. As discussed earlier (see

section 4.3.2.1), use of sucrose helped in collection of the spectra by reducing sedimentation rate, but it also slightly reduced the rotation rate.

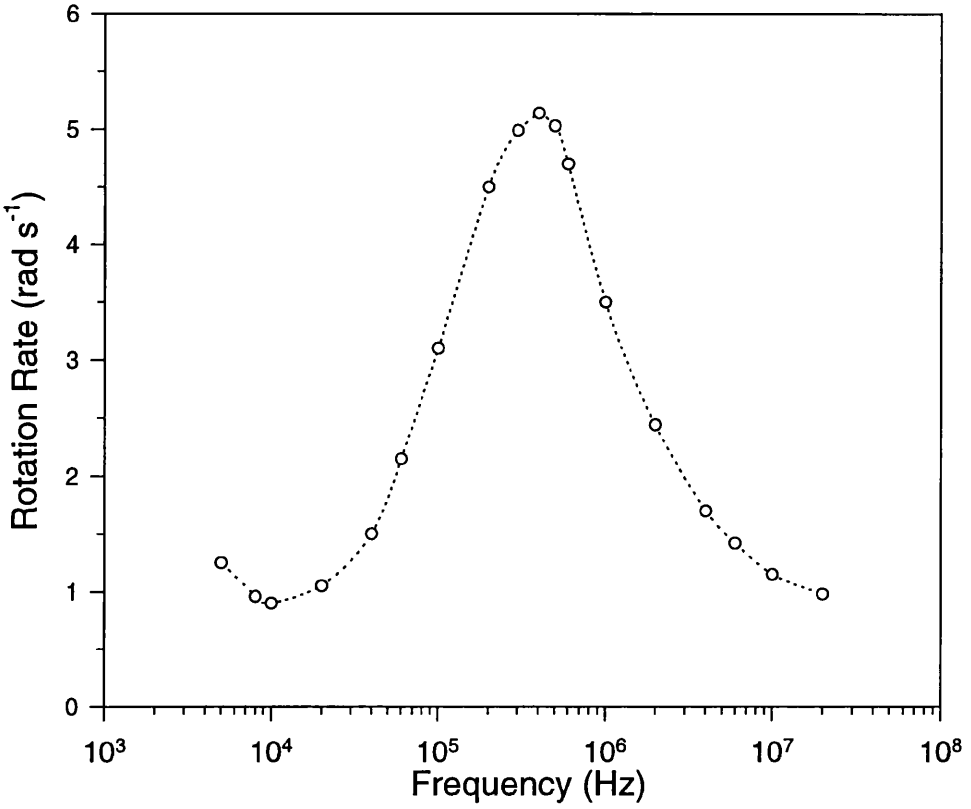

Figure 4.7: The electrorotation spectrum of a polystyrene beads suspended in 260mM sucrose (6.51μS cm^{-1}). The spectrum was collected between 5kHz and 20MHz at a voltage of 3V using polynomial electrodes of 360μm separation. Only co-field rotation (i.e. positive rotation rates) peaks can be seen, these are located at <1kHz and 400kHz.

The co-field rotation peak at 400kHz is predicted by the theory summarised in appendix A. The source of the co-field rotation peak occurring at a frequency below 1kHz has yet to be fully explained. Further detailed analysis at these low frequencies is hampered by electrolysis at the electrodes (see section 4.2.2), electrophoresis,[128] and an attenuated response due the effects of electrode polarisation.[132] The nature of the low frequency peak is suspected to be based on changes occurring within the ionic double layer surrounding the bead.[37]

4.3.3.2 Human Neutrophils

The electrorotational work on neutrophils provided a more complex spectrum having both a co-field and an anti-field rotational peak (see figure 4.8). Upon neutrophil activation, subtle changes in the physical properties of the cell were reflected in the changing nature of the spectrum.

In contrast to similar studies on human lymphocytes,[147] a relatively high medium conductivity (400μS cm^{-1}) was used in this study. A low conductivity was not used was for three reasons. Firstly, the increased centrifugal washing necessary to lower medium conductivity initiated neutrophil activation. This mechanism was caused by the cellular compression and was indicated by cell aggregation.[134] Secondly, a previous study has shown that leakage of cytoplasm contents makes it difficult to maintain a consistently low medium conductivity.[35] When a higher conductivity media is used, the suspension media is much less sensitive to the effects of ionic leakage. Thirdly, at a low conductivity, the positive dielectrophoretic force attracting rotating particles towards the electrodes is apparent over a broader range of frequencies (see section 4.3.1). Experimentally, this leaves less time to collect the spectrum of a single cell.

The recorded spectra are shown in figure 4.8. The spectrum of the resting neutrophil was subsequently simulated to provide the best fit spectrum using the double shell model (appendix A).

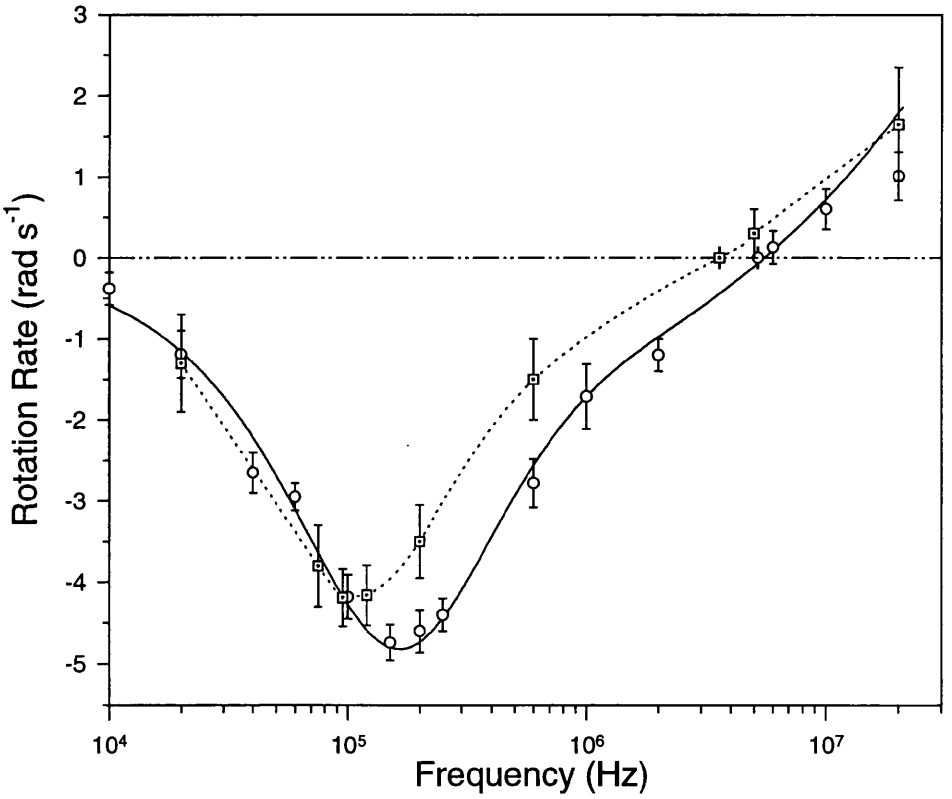

Figure 4.8: The electrorotation spectra of resting (O) and activated (□) human neutrophils. The spectra were collected using polynomial electrodes (360μm separation) at a field strength of *ca.* 56V cm^{-1} (2V p-p) in a sucrose/PBS medium (2.4% PBS, 400μS cm^{-1}). The neutrophils were activated using PMA at a final concentration of 25μM. The spectrum of the resting neutrophils has been simulated (solid line) using the double-shell model, parameters are given in table 4.1.

The model is based on that described by Asami *et al.*[131] for mouse lymphocytes. The parameters used for the neutrophil model are summarised in table 4.1. Values for cell and nucleus radii were measured using light microscopy. Other values were gathered from similar work on lymphocytes[130,131] or found in the literature.[141,142]

Parameter	Value	Source
Cell radius (R)	6μm	Measured
Cell membrane thickness (d_m)	8nm	Asami *et al.*[131]
Nucleus radius (r_n)	3.5μm	Davis *et al.*[143]
Nuclear membrane thickness (d_n)	20nm	Asami *et al.*[131]
Medium Conductivity (σ_{med})	0.4mS cm^{-1}	Measured
Medium Permittivity (ε_{med})	$79\varepsilon_0$	Arnold *et al.*[141]
Cell membrane conductivity (σ_m)	$1x10^{-8}$μS cm^{-1}	Ziervogel *et al.*[130]
Cell membrane permittivity (ε_m)	$6.2\varepsilon_0$	Ziervogel *et al.*[130]
Cytoplasm conductivity(σ_{cp})	3mS cm^{-1}	Ziervogel *et al.*[130]
Cytoplasm permittivity (ε_{cp})	$60\varepsilon_0$	Asami *et al.*[131]
Nuclear membrane conductivity (σ_n)	60μS cm^{-1}	Asami *et al.*[131]
Nuclear membrane permittivity (ε_n)	$28\varepsilon_0$	Asami *et al.*[131]
Nucleoplasm conductivity (σ_{np})	13.5mS cm^{-1}	Asami *et al.*[131]
Nucleoplasm permittivity (ε_{np})	$52\varepsilon_0$	Asami *et al.*[131]
Permittivity of free space (ε_0)	$8.854x10^{-12}$F m^{-1}	CRC Handbook

Table 4.1: The parameter values and literature sources used in the double-shell model of a neutrophil

Key changes in the spectrum of the neutrophil upon activation are the shifts of the anti-field rotation (f_p) and cross-over (f_c) peak frequencies. The lack of an additional obvious dispersion in the 500kHz-5MHz range suggests that nucleus is not contributing significantly to the nature of the anti-field rotation peak.[130,131] For this reason, the discussion of differences in these spectra will focus on physical changes in the cellular membrane and cytoplasm. Relying solely on the electrorotational spectrum, it is difficult to precisely identify which physical change or combination of physical changes is occurring in an activated neutrophil. Parameter values within the model were varied in an attempt to explain the observed changes in the neutrophil spectra.

Previous work[148] has found that cell volume increases by an average by 21.7% upon neutrophil activation. This would be apparent as a 4.5% increase in cell radius. Furthermore, activation is known to induce physical changes in the structure of the cell membrane, as illustrated in figure 4.5c. An activated neutrophil initially forms blebs on the membrane surface, subsequently, it undergoes shape changes associated with actin polymerisation and de-

polymerisation.[149,150] Other associated physical factors such as changes in membrane capacitance (common in other studies on cell differentiation[129,147]) may also contribute to the nature of the electrorotational spectra.

The model was used to investigate the effects of varying four dominant cellular parameters (R, d_m, ε_m and σ_{cp}). The effect of increasing cell radius is shown by the appropriate downward shift in f_c and f_p (figure 4.9a). However, an unrealistic (i.e. not seen by light microscopy) volume increase of 337% would be required to provide an acceptable fit (i.e. R=9μm) to the activated neutrophil spectrum. The model also predicts that a decrease in membrane thickness to *ca.* 5nm would provide a simulated spectrum with an appropriate f_c (figure 4.9b). An increase in membrane capacitance (shown by an increase in ε_m (figure 4.9d)) is a likely possibility since membrane roughness increases during bleb formation. Finally, decreased cytoplasm conductivity is another possible explanation (figure 4.9d).

The increase in volume after neutrophil activation has been predicted elsewhere using a different technique. This would concur with a combination of the changes predicted by the model. For example, the expulsion of ions during cell activation[44] and subsequent uptake of water would reduce the cytoplasm conductivity and increase cell volume. In addition, membrane stretching associated with increased volume and bleb formation, is a suspected process leading to a reduction in the thickness of the cell membranes.[151] An increase in membrane capacitance is not unexpected, since it has been also measured in the differentiation of DS19 leukaemia cells,[35] and following the mitogenic stimulation of human T and B lymphocytes.[147]

The electrorotation spectra of the resting and activated neutrophil do indicate significant changes in the electrical properties of the cell. However, it is not possible to de-convolute the measured changes into specific physical changes in the cellular structure and physiology - only an indication of likely changes is possible (figure 4.9). To allow a precise interpretation of the data, a more accurate electrorotational spectrum is necessary. In contrast to the spectra of resting neutrophils there were broader errors and a reduced number of data points (see figure 4.8) collected for the activated neutrophils. This makes it unrealistic to attempt to model the data and assign specific parameter values. These difficulties are associated with the inevitable adhesion and motility mechanisms characteristic of activated neutrophils. Experimentally, this was demonstrated by cell adhesion to the substrate and a non-spherical shape. For resting neutrophils, coating the substrate in milk protein (see section 4.2.5.1) was effective in limiting the effects of the activation mechanisms, however, the addition of PMA always accelerated cell adhesion. A reduced time window of only 5 minutes was available to collect the spectrum of the activated neutrophil.

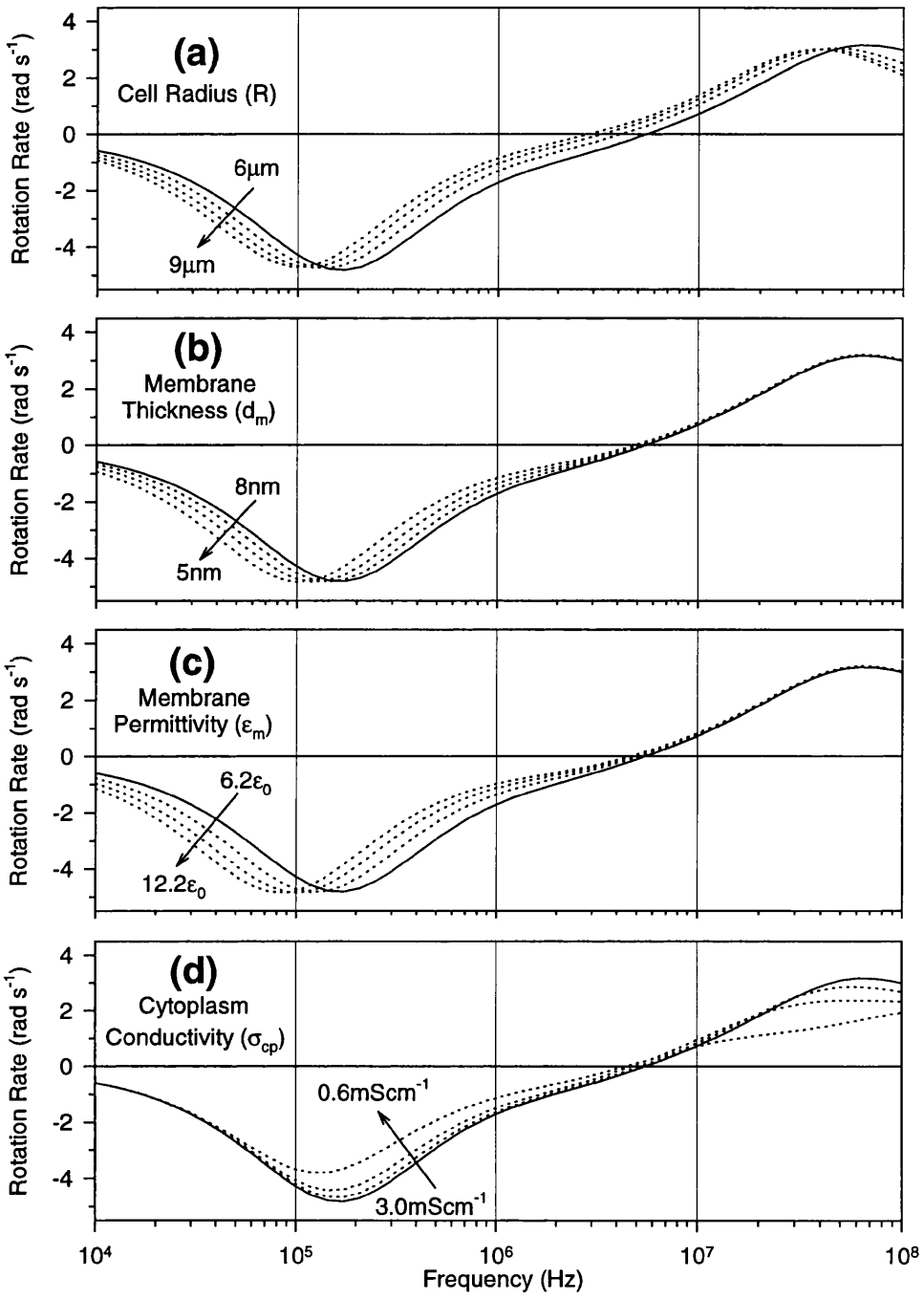

Figure 4.9: The effect of the variation of four cellular parameters (R, d_m, ε_m and σ_{cp}) on the nature of the modelled electrorotational response of human neutrophils. The modelled response of resting neutrophils (solid line) can be compared to the measured (see figure 4.8) changes. Conceivable physical changes in cellular properties upon cell activation are indicated by dotted lines.

4.4 Summary

This work has demonstrated the successful use of dielectrophoresis for particle confinement and for the analysis of subtle physical changes in living cells. Particle confinement was straightforward following the selection of a suitable medium conductivity and signal frequency. The technique of electrorotation was a sensitive means of detecting changes in the physical properties of human neutrophils when activated by chemotactic reagents. Subsequently, analysis using the double-shell model provided an indication of the changes in specific cellular parameters. The results agree with the observations of other studies on neutrophil activation, and the nature of the dielectrophoretic response is similar to that seen in studies on other blood cells.

4.4.1 Potential for Further Work

The fabrication of novel electrode structures using microfabrication techniques presents an excellent opportunity for the exploitation of dielectrophoresis within biotechnology. Applications such as the separation of breast cancer cells from erythrocytes[152] have already been demonstrated. The use of electrorotation in water purity analysis has already generated significant industrial interest.[37] Further electrode miniaturisation and a better understanding of associated theory presents exciting possibilities for the future. For example. the use of dielectrophoresis to control the movement, and measure the electrical properties, of sub-μm particles such as viruses and macromolecules.[56] One novel application of dielectrophoresis is travelling-wave dielectrophoresis.

4.4.1.1 Travelling-Wave Dielectrophoresis

Masuda *et al.*152 were the first to note the potential use of phase-shifted voltage applied in a linear electrode array to move cells. The resultant electrokinetic force on particles within the electrode array could be used to move and/or sort particles with different electrical properties.[32,154,155] Figure 2.2c (chapter 2) shows a structure built during this project to separate two particles of similar but not identical electrical properties. The device needed three signal generators, each providing a voltage to the three channels of the Y-shaped electrode. In theory, one channel would be used to move both particle types towards the centre of the Y, while specific signal frequencies would be applied to the remaining fingers in order to differentially guide each particle type into a separate channel. Although the theory of the technique has been proposed,[156] the experimental analysis of the technique was impeded due to the difficulties in the fabrication of the complex electrode array. The principal difficulties were both poor insulator adhesion and formation of reliable thru-holes (see section 2.2.1.2). Further work to overcome these problems is in progress.

5. Biosensor Interfaces

This chapter describes the analysis of enzyme content within a polymer matrix using three different techniques, focusing on the quantification of the amount of GOx entrapped within a PPy film. As discussed in the Introduction, much work has been done on this system, primarily concentrating on its use as a glucose biosensor. However, this work focuses on two a particular aspects of this biosensor interface: the relationship between enzyme concentration in the polymerisation solution and its concentration in the as-grown PPy/GOx film, and the analysis of the amount of *active* enzyme in the film.

5.1 Growth of Biosensor films

PPy was first prepared chemically as a powder in 1916 as described by Chandler and Pletcher,[157] but first produced electrochemically in 1968[158] and as a free standing film by Diaz *et al.* in 1979.[159] Work by Foulds *et al.*[160] in 1986 demonstrated its use as a matrix for GOx entrapment leading due to its application as a glucose biosensor.

5.1.1 Theory: Polymer Growth

The electro-oxidation of the monomer is believed to occur via a reactive π-radical cation mechanism (see figure 1.4, in chapter 1) which reacts with a neighbouring pyrrole species either in solution or in the polymer backbone.[12] The resulting polymer incorporates anions from the supporting electrolyte and has a net positive charge. Although the enzyme is entrapped as a poly-anion in an active form, its viability is dependent on storage conditions and usage,[161] and in one instance its stability at pH extremes was improved by the entrapment process.[162]

The following sections review the variety of polymerisation conditions that were investigated and optimised during the course of this study.

5.1.2 Methods & Materials: Polymer growth

The biosensor films were electrodeposited onto a gold surface evaporated onto a scribed glass substrate. The electrodes were prepared by electron-beam evaporation of Ti/Pd/Au (10/10/100nm) multilayer structure, providing excellent adhesion of the metal to the glass substrate, and good electrochemical stability, even at high oxidative potentials in aqueous solutions. Immediately prior to bio-polymer deposition the gold surface was cleaned by a RIE

etch for 5 minutes (50mT, 20sccm and 10W) in first oxygen and then argon using a PlasmaFab ET340.

Biosensor films were grown from a solution of 150mM pyrrole in 50mM NaCl with a varying concentration of GOx (*Aspergillus niger* (E.C. 1.1.3.4), Medisense UK, with an activity of 165U mg^{-1}) in the range 6 to 420μg ml^{-1}. The pH of the polymerisation solution was adjusted to 4.5 by drop-wise addition of HCl. Polymer deposition was carried out by cyclic voltammetry using an EG&G 273A potentiostat, scanning the working electrode (area *ca.* 90mm^2) between 0 and +0.8V (scan rate=50mV sec^{-1}) with a platinum gauze counter electrode of area of 2cm^2. Film growth using this technique produced a consistent film thickness of *ca.* 75nm, as measured using a Dektak ST^3 (Veeco Instruments Inc.) surface profiler. Electrochemical experiments were conducted using an Ag/AgCl (3M NaCl) reference electrode (BAS), against which all the potentials in this section are quoted.

The glass electrodes were scribed prior to evaporation but only broken in two after growth of the polymer film. The lower part of the electrode was used for the XPS and FTIR analysis, while the upper half was used for the electrochemical assay. This ensured that exactly the same film was used in all three analysis techniques used in this study. All electrochemical assays were completed within 24 hours of film growth. The films for XPS and FTIR analysis were stored overnight in a solution of 50mM NaCl thus minimising the effects of adventitiously adsorbed contamination during transport.

5.1.3 Results and Discussion

Use of methods adapted from the work of various groups provided background information to guide the selection of the above polymerisation conditions.[163-162] The following sections focus on elements of the biosensor preparation of specific note in this study.

5.1.3.1 Effect of pH

Work by Gros[166] has previously shown that films grown at pH 5-6 can have an enhanced response. Whilst maximising the response was certainly desirable, other parameters such as film uniformity and "quality" are examples of additional important factors taken into consideration during the optimisation of the growth procedure.

It was important that the films grew uniformly across the whole electrode since pinholes or defects lowered the sensitivity of the electrochemical assay due to the resultant higher baseline current. Furthermore, uniform films held a significant advantage in the spectroscopic analysis, particularly in FTIR analysis,[167] as a 'smooth' film would reduce quantification errors from diffuse reflections. The observation of higher quality PPy films is related to maintaining a low

pH close to the site of electropolymerisation,[168] thus promoting the progress of the nucleated growth mechanism.[169]

The benefit of lower pH is evident in the range pH 2 to 7, however, films grown at pH <2 had a poor glucose response due to reduced enzyme entrapment within the film. This observation highlights the mechanism by which the enzyme is incorporated into polymer matrix. Since GOx has an isoelectric point of 4.2,[170] in a pH 2 solution the enzyme will have a positive charge whereas at a >pH 4.2 the enzyme will have a negative charge aiding its incorporation into the polymer film.

A solution of pH 4.5 was found to be the best compromise. Films grown as this pH deposited both easily and uniformly at all utilised GOx concentrations producing noticeably 'smoother' defect free films. Figure 5.1 provides an illustration of the galvanostatic profiles for PPy/GOx films grown in solutions of increasing pH. The increased difficulty of polymerisation in higher pH solutions is apparent because the potentials are being forced to higher values, and subsequently staying at these values for a longer time, before returning to the characteristic growth process at *ca.* +0.7V. Maintaining the potential below +0.8V helped to prevent both the over-oxidation of the PPy and formation of over-oxidation related groups[171] (e.g. C=O) in the polymer backbone. This factor was of significant value during the quantitative analysis of the XPS data (see section 5.3.4).

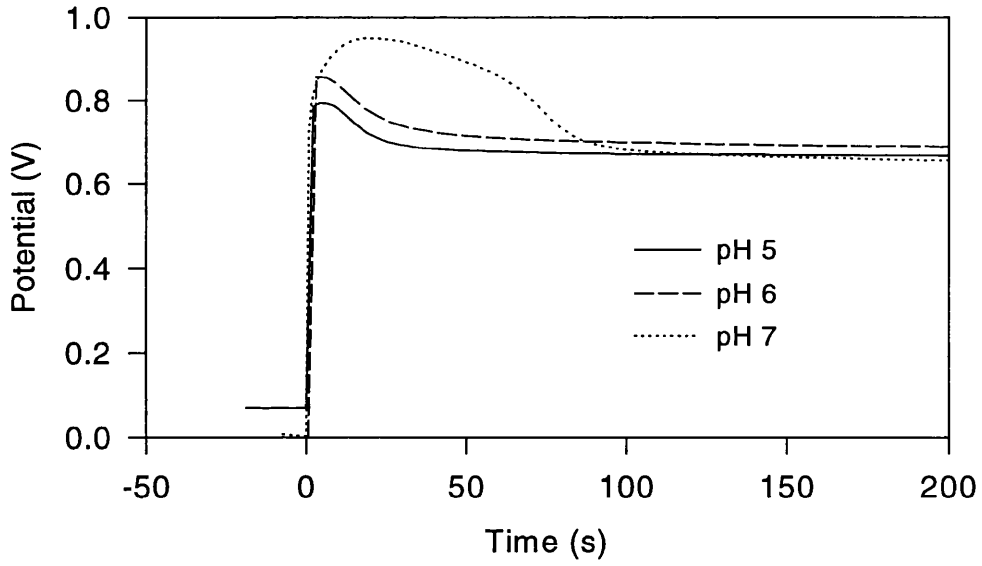

Figure 5.1: The galvanostatic growth profiles of a PPy/GOx films prepared from a solution of 150mM pyrrole and 120μg ml^{-1} GOx in 50mM NaCl adjusted to pH 5,6 and 7 by dropwise addition of HCl. The polymer films were grown on RIE cleaned evaporated gold electrodes (area *ca.* 90mm^2) at a current density of 500μA cm^{-2}, the potentials are quoted *vs.* Ag/AgCl. The speed with which the response reaches a stable value (*ca.* 0.7V) provides a guide to the ease of film growth.

5.1.3.2 Film Thickness

Routine measurement of the polymer film thickness is a persistent difficulty encountered in the study of conducting polymer films. It is commonly estimated by the measurement of total polymerisation charge.[165] However, it is difficult to apportion the recorded charge to that solely used in the growth of the polymer membrane. Precision techniques, such as ellipsometry[28] or atomic force microscopy (AFM)[172] can be used for detailed analysis, although they are not suitable for routine thickness measurements. In this study, measurement of film thickness was investigated using all the above techniques, excluding ellipsometry. However, none was found to be ideal in terms of both accuracy and convenience. In consequence, a further method was developed based on the observation of the *in-situ* current amplitude at 0V correlated against thickness measurements made using a surface profiler. This correlation is shown in figure 5.2.

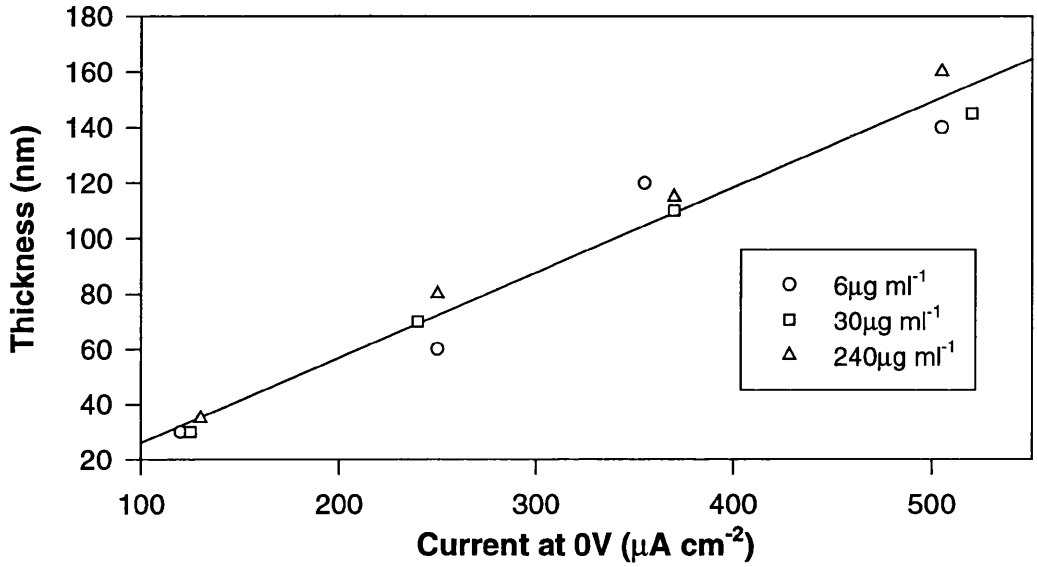

Figure 5.2: The variation of film thickness with current amplitude at 0V. The graph shows thickness measurements for films grown at three different enzyme concentrations (6, 30 and 240μg ml^{-1}). The PPy/GOx films were prepared from a solution of 150mM pyrrole and GOx in 50mM NaCl (pH 4.5). The polymer films were grown on RIE cleaned evaporated gold electrodes (area *ca.* 90mm^2) by successive scans between 0 and +0.8V *vs.* Ag/AgCl at a scan rate of 50mV s^{-1}.

A current of -250μA cm^{-2} measured at 0V was found to provide the required film thickness of *ca.* 75nm. The number of potential cycles required to reach this current marker increased with solution enzyme concentration. The range varied from 5 sweeps (6μg ml^{-1}) to 11 sweeps (420μg ml^{-1}). An example of the stepwise variation of current is illustrated in figure 5.3. To confirm the validity of the measurement at 0V, cyclic voltammograms were recorded for PPy/GOx films grown at a range of enzyme concentrations. The responses indicated no difference in the nature of the observed response that could be ascribed to enzyme dependent redox activity at 0V. This concurred with the previous work by Belanger *et al.*[173] that

demonstrated no difference at 0V between the cyclic voltammograms of PPy and PPy/GOx films grown using similar polymerisation conditions.

Surface profilometry measurements for a range of PPy/GOx films confirmed the correlation between the 0V current marker and film thickness. Since the only variable in the polymerisation solution was enzyme concentration, it is reasonable to assume that the rise in the negative value of the current marker is a reflection of the increase in polymer thickness and subsequent rise in non-Faradaic charging current. This assumes a mostly passive electrochemical role for GOx during PPy growth, which agrees with the conclusions of similar work.[162,174] As the polymer growth mechanism is inhibited by increased enzyme concentration,[175] at increased concentration a greater number of potential sweeps are required to grow the same film thickness.

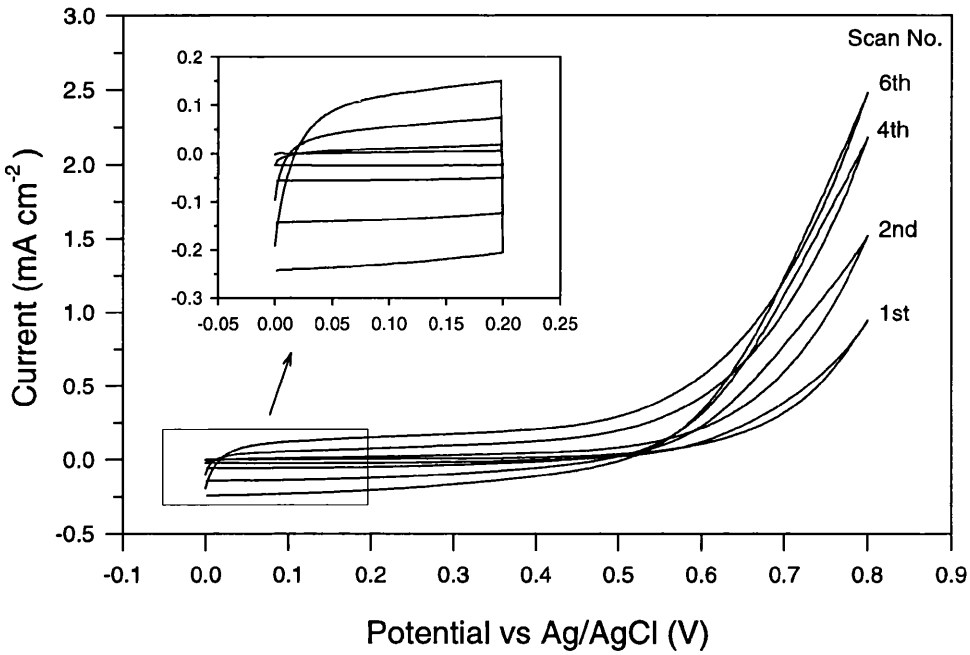

Figure 5.3: A sequence of voltammograms recorded during the growth of a PPy/GOx film prepared from a solution of 150mM pyrrole and 30μg ml^{-1} GOx in 50mM NaCl (pH 4.5). The polymer films were grown on RIE cleaned evaporated gold electrodes (area *ca.* 90mm^2) by successive scans between 0 and +0.8V *vs.* Ag/AgCl at a scan rate of 50mV s^{-1}. A current of -250μA cm^{-2} at 0V after the 6th scan corresponds to a film thickness of *ca.* 75nm.

The current at 0V was easily monitored using the potentiostat software used to control the cyclic polymerisation procedure. This thickness measurement technique is limited to a range of enzyme concentrations in a particular solution. However, it provides a very convenient method of *in-situ* measurement of polymer thickness and minimised the possibility of contamination associated with *ex-situ* techniques. Furthermore, the use of a cyclic growth procedure aided the

consistent preparation of uniform high-quality polymer films, an observation noted by other groups investigating the mechanism of conducting polymer growth.[176,177]

Film thickness studies using both AFM and surface profilometry also provided information on film morphology. These are illustrated by the typical film thickness profile (figure 5.4a) and the textured surface of PPy (figure 5.4b) associated with its nucleated growth mechanism. A film thickness of 75nm was chosen since is provided a satisfactory electrode coverage and the consistent electrochemical response. A thicker film was undesirable due to the loss of peak definition in the FTIR spectra (see section 5.4.3).

5.1.3.3 Selection of Electrolyte

A range of polymerisation counterions were examined including NO_3^{2-}, Cl^-, PO_4^{2-} and ClO_4^-, at a variety of concentrations (5-500mM). The Cl^- ion was judged to be the best, the use of PO_4^{2-} resulted in poor quality films even at reduced pH. No advantage was gained by variation of electrolyte concentration. These results agree with observations of other groups.[165,174] Interestingly, the choice of cation also had a role to play in the selection of electrolyte. Residual K^+ cations within the PPy/GOx films produced a small but interfering signal in the Carbon(1s) XPS signal (figure 5.5) which made baseline subtraction more difficult. This prompted the use of NaCl (50mM) in preference to commonly used KCl.

5.2 Electrochemical Analysis

This section describes the electrochemical analysis of the active enzyme response within the polymer films grown by the procedure described in section 5.1.

5.2.1 Methods & Materials: Electrochemical Analysis

The as-grown biosensor films were first washed in 100mM phosphate buffer (pH 7.4). Then, the PPy component of the biosensor films was over-oxidised in the same buffer by successive cyclic voltammograms. The over-oxidation potential cycle was carried out using cyclic voltammetry on an EG&G 273A potentiostat, scanning the working electrode potential between -0.25 and +1.25V (scan rate=50mV sec^{-1}) with a platinum gauze counter electrode of area of $2cm^2$. Cycles were repeated until a consistent voltammogram was observed. This procedure took up to 20 minutes, resulting in a non-conducting polymer matrix containing the entrapped enzyme. The electrochemical assay for H_2O_2 was conducted at +0.65V in unstirred buffer using additions of 2 or 20mM glucose prepared in the same buffer. Electrochemical experiments were conducted using an Ag/AgCl reference electrode (BAS), against which all the potentials in this section are quoted.

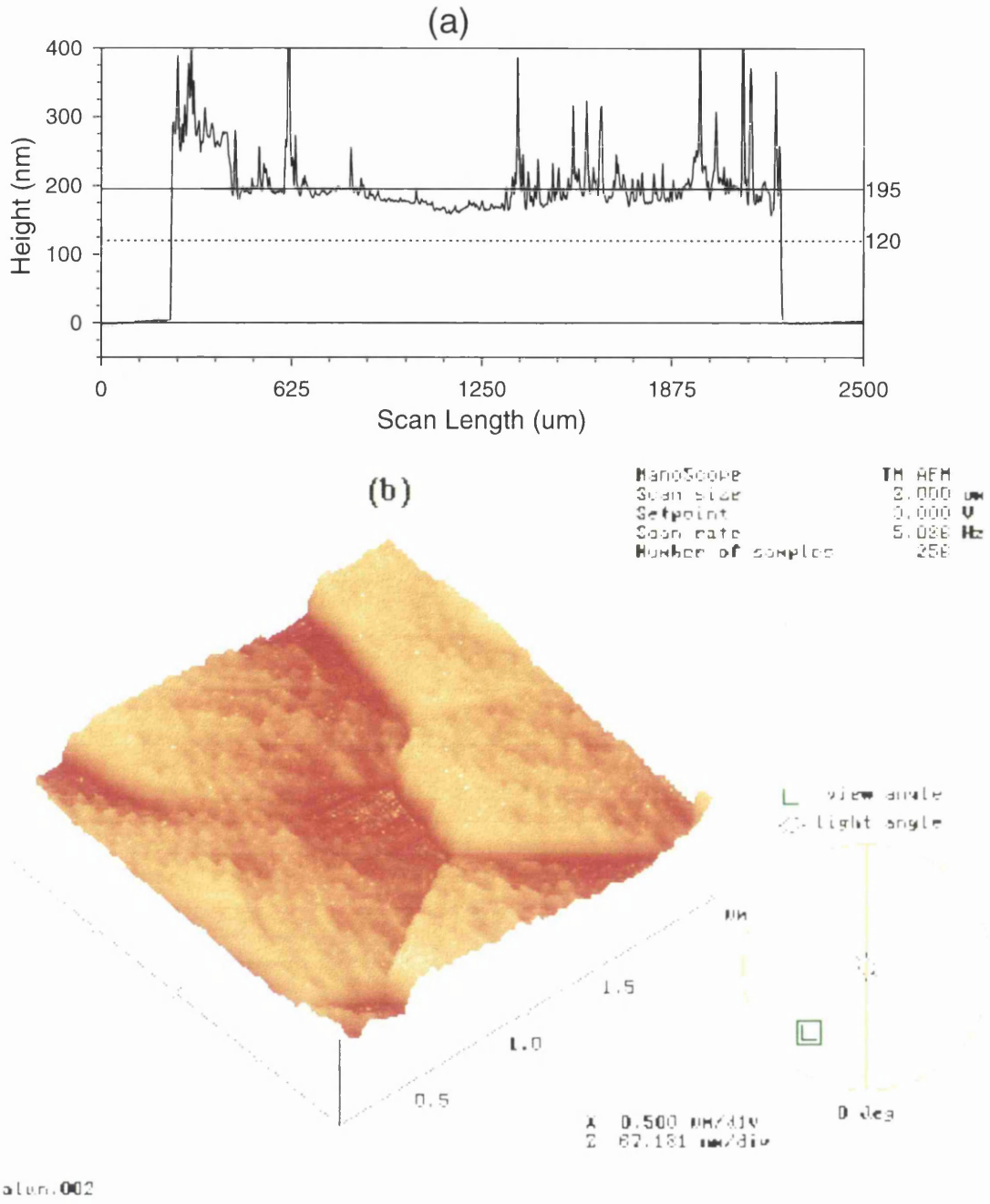

Figure 5.4: (a) A film surface profile for a PPy/GOx film recorded using a Dektak^{3}ST surface profiler. The polymer film thickness is *ca.* 75nm after subtraction of the metal film thickness (120nm). The plateau in the scan length region from 250 to 450μm is due to an aberration associated with the relative compliance of the polymer (i.e. the relative stiffness of measuring cantilever versus that of the polymer). (b) An AFM image (4μm^2 area) showing the surface morphology of the film measured above. The image agrees well with the suggested nucleated growth mechanism for PPy, the surface appears to be composed of a series of nucleation sites that have merged into a continuous film. The image was recorded using a Nanoscope 3 AFM scanning at 5Hz.

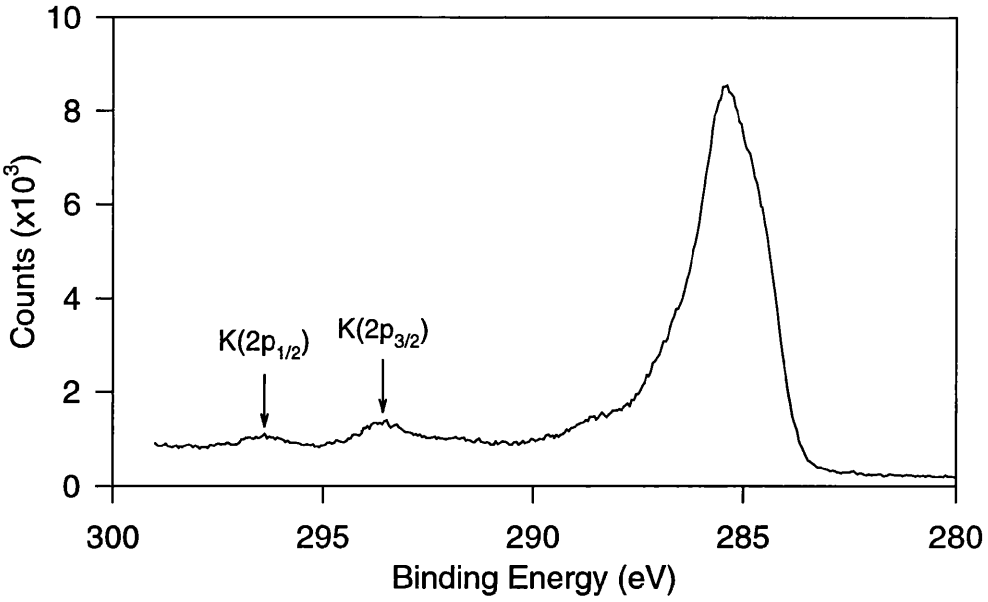

Figure 5.5: A Carbon (1s) XPS spectrum for a PPy film grown using 150mM pyrrole in 50mM KCl (pH 4.5). The spectrum demonstrates that some potassium ions, indicated by peaks at 294 and 296eV, still remain in the sample even after washing in RO water and drying using a nitrogen gun. The potassium peaks are a hindrance in the fitting process used in the analysis of XPS spectra, in consequence, a NaCl electrolyte was used in subsequent experiments. Details of the procedure used for recording the XPS spectra are given in section 5.3.2.1.

5.2.2 Results and Discussion

The amperometric assay technique for glucose is a familiar tool used by many groups[178-180] in the field since the first data on PPy/GOx based biosensor was published in 1986.[160] However, the use of deliberately over-oxidised polymer films as an entrapment matrix has only been investigated in recent years.[166,181] This section will highlight the electrochemical advantages of using an over-oxidised PPy (PPy-oox) film as a matrix for GOx entrapment.

5.2.2.1 Why Use Over-oxidised PPy Films?

A PPy-oox film was chosen because of the larger baseline current associated with the charging current of solely oxidised PPy (PPy+).[181] The magnitude of non-Faradaic baseline current was considerably reduced from *ca.* 20μA cm^{-2} to 90nA cm^{-2}. In addition, the time taken to reach a satisfactory stable baseline response was reduced from 60+ to 5 min. However, the dominant advantage was the increased sensitivity and reproducibility of electrochemical assays. PPy+ films are known to degrade (i.e. over-oxidise) with time, particularly when exposed to the high positive potentials[182] necessary for the standard H_2O_2 assay. Furthermore, chemical over-oxidation of PPy+ by H_2O_2 is another factor that can alter the reproducibility of measurements that rely on the conductivity of PPy+ based films.[183] In fact, it has been suggested that the long baseline settling time required for PPy+/GOx films, at potentials

necessary for H_2O_2 detection, is responsible for a significant amount of PPy over-oxidation.[173] Using PPy-oox films from the outset eliminates any errors that might be introduced by the uncharacterised effects of polymer degradation.

There has been much recent interest in the application of PPy-oox in biosensor applications, primarily for its permiselective properties.[184] The permiselective properties of PPy-oox have been shown to significantly hinder the transport of common anionic interferents (e.g. dopamine or ascorbate). Neither, the transport properties of H_2O_2 or O_2 within the film is significantly affected, nor is the activity of the entrapped GOx.[166] Various methods of over-oxidation are used, including both constant and scanned potential methods. The mechanism has been shown to depend on electrolyte with an over-oxidation process involving the smaller and more nucleophillic OH^- ions in NaOH proceeding at twice the rate of an equivalent concentration of phosphate buffer.[185]

Standard voltammograms for the over-oxidation of a PPy/GOx film following the procedure used in this study are shown in figure 5.6.

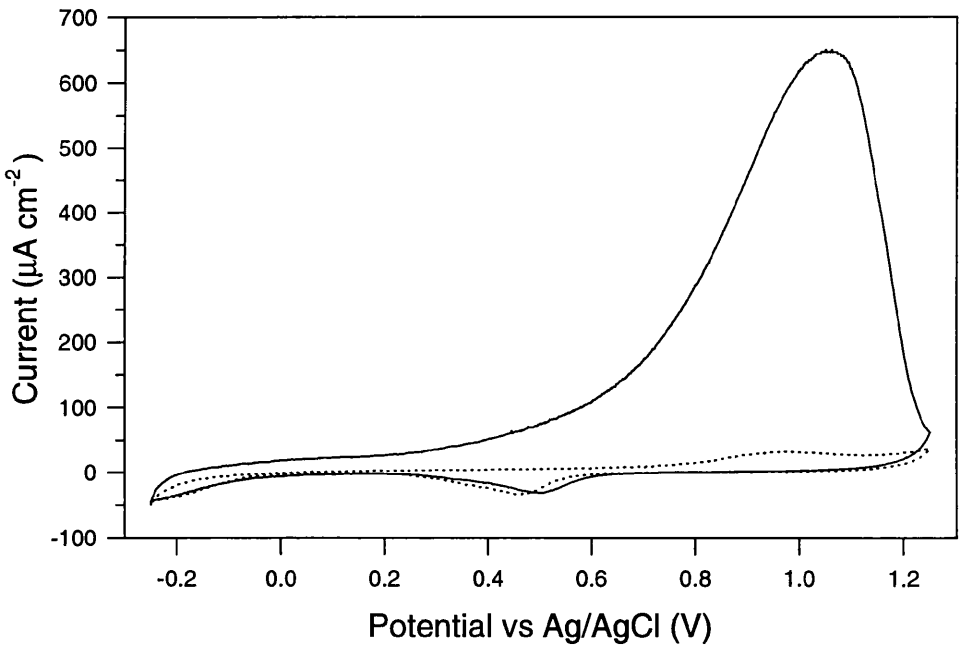

Figure 5.6: The over-oxidation of a PPy/GOx film (enzyme concentration 30μg ml^{-1}) grown on RIE cleaned evaporated gold electrodes (area *ca.* 90mm^2) in 100mM potassium phosphate buffer (pH 7.4). The potential is being cycled between -0.25 and +1.25V *vs.* Ag/AgCl at a scan rate of 50mV s^{-1}. The first cycle results in a massive current due to the over-oxidation of the conducting PPy, whilst by the 20th cycle all the PPy has been over-oxidised and the voltammogram represents that of a non-conducting film.

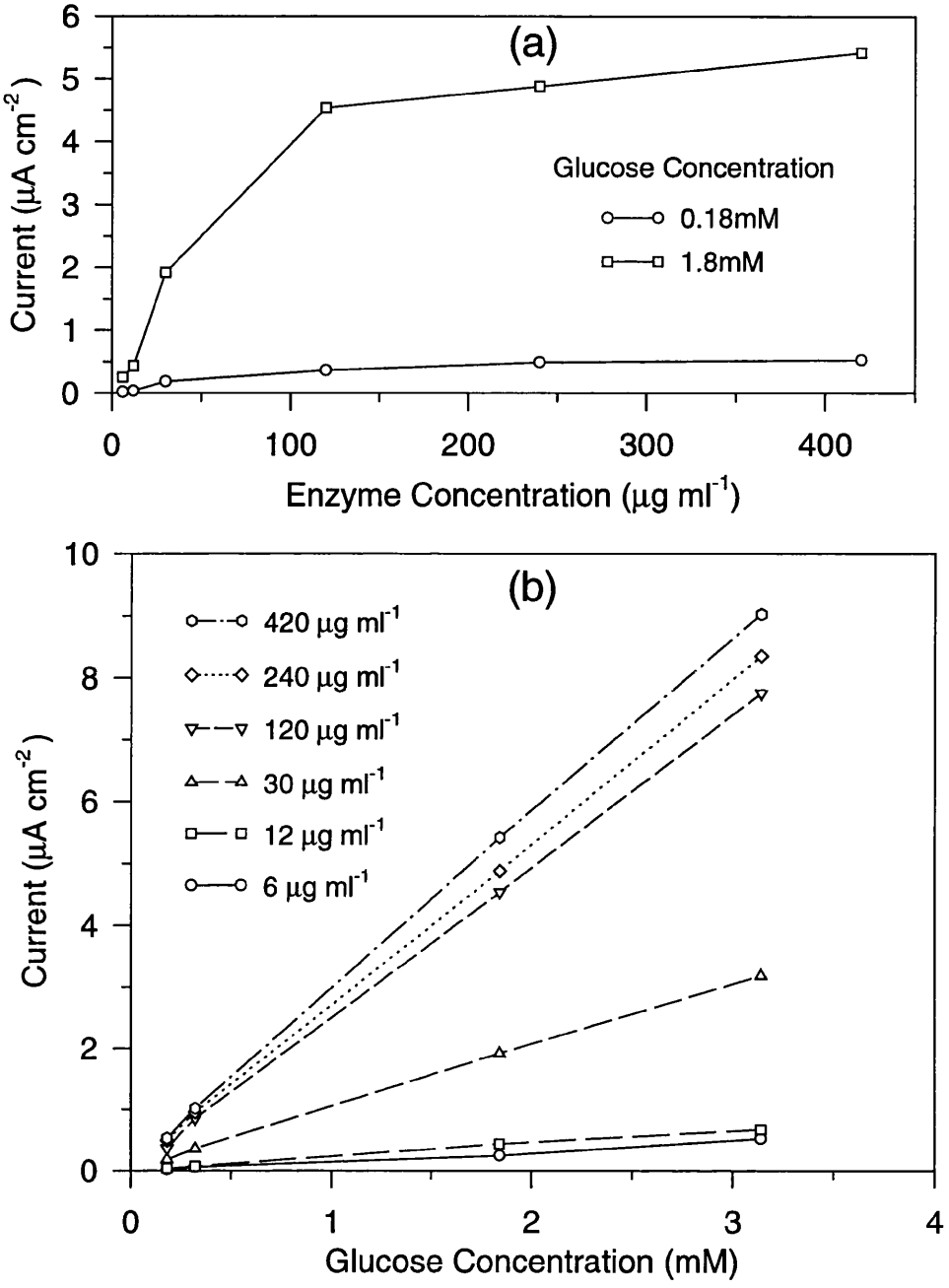

Figure 5.7: The electrochemical response of the range of PPy/GOx films analysed in this study. The polymer films were grown on RIE cleaned evaporated gold electrodes (area *ca.* 90mm^2) from solutions of 150mM pyrrole and GOx (6-420μg ml^{-1}) in 50mM NaCl (pH 4.5). The amperometric response from H_2O_2 was measured at +0.65V (*vs.* Ag/AgCl) in 100mM phosphate buffer (pH 7.4) following two additions of both 2 and 20mM glucose. Note the non-linear variation of current response (i.e. active enzyme within the biosensor film) with increasing enzyme concentration in the polymerisation solution.

5.2.2.2 Assay Results

Electrochemical assays for all the samples were performed at four different glucose concentrations. The results for the range of enzyme concentrations in the polymerisation solution are shown in figure 5.7. The assays have a linear response to a range of low glucose concentrations. However, the corresponding variation of response with solution enzyme concentration is non-linear. For example, comparing the response of the 420μg ml^{-1} and 30μg ml^{-1} films, the 14 fold increase in solution enzyme concentration results in only a 3 fold increase in electrochemical response.

Similar non-linear responses in the literature are ascribed to a combination of mass transport (i.e. diffusion of glucose, oxygen and hydrogen peroxide), enzyme turnover rate constants or enzyme activity effects.

Use of thin polymer films (i.e. <~100nm) in preference to thicker films provides faster response times, but at the expense of reduced magnitude of total current response (i.e. sensitivity). Response times are improved due to the reduction of substrate and product mass transport effects within the polymer matrix. Sensitivity is affected by the reduced total amount of enzyme in the polymer matrix of thinner films. In practice, the selection for optimal film thickness is a compromise is between these two factors and this subject has received thorough investigation in two previous studies.[165,166]

In this study, thin biosensor films (*ca.* 75nm) were used, since it was desirable to minimise the attenuation in sensor response due to mass transport effects. The use of thin films provided a clearer indication of *active* enzyme content within the biosensor film. The sensitivity of the biosensor films response was not a matter of significant concern even at less than micromolar glucose concentrations, due to excellent assay responses afforded by the large electrode surface area and low PPy-oox/GOx baseline currents. Low glucose concentrations were used in the assay, so that the electrochemical response would accurately reflect the enzyme loading and activity within the film, and not be determined by a saturated response. The logic used in the selection of film thickness and substrate concentrations is demonstrated by the linearity of responses (figure 5.7) for all the PPy/GOx films used in this study.

Nevertheless, the effects of non-linear response could be seen at higher glucose concentrations. Figure 5.9 presents the detailed electrochemical assay of the 120μg ml^{-1} biosensor film over a broader range of glucose concentrations. The response is linear at low concentrations (up to 2.5mM) while a non-linear response is apparent at higher glucose concentrations. The Michaelis-Menten kinetic parameter (K_M) for the enzyme in the biosensor film can be

determined when the assay was performed over a broader range of glucose concentrations. For example, the K_M value for the 120μg ml^{-1} film was measured as 24mM, as determined from the *x*-axis intercept of a Lineweaver-Burk plot[186] (see figure 5.8). Similar values of between 10 and 30mM were obtained for the range PPy/GOx films. These values agree with those reported in the literature,[160,162] so excluding the possibility that the entrapment mechanism has a significant concentration dependent effect on enzyme activity.

In conclusion, analysis of the results suggests that enzyme concentration in solution is a poor guide to active enzyme concentration in the biosensor film. This is in contrast to the earlier reports[160,178] of a linear a variation with GOx concentration. However, the earlier analyses were performed on thicker films under different polymerisation conditions. This non-linear variation was also noted by Fortier *et al.*,[162] and was explained in terms of thickness variations and the non-linear distribution of H_2O_2, and hence current response, in the polymer film as the glucose is more rapidly consumed at the biosensor/solution interface. This is certainly a valid argument and will affect the electrochemical response, and helps to explain the small variation response between the 120, 240 and 420μg ml^{-1} films (see figure 5.7). However, it does not provide a complete explanation, since the XPS and FTIR results in the next sections will demonstrate a similar non-linear variation in the enzyme loading of polymer films. Finally, these results suggest that there is a maximum concentration of enzyme that can be entrapped in the polymer matrix, although, from comparison with similar studies, this concentration is likely to depend on a variety of polymerisation conditions. Further work is necessary to separate the influences of enzyme concentration, enzyme activity and polymerisation conditions on biosensor response.

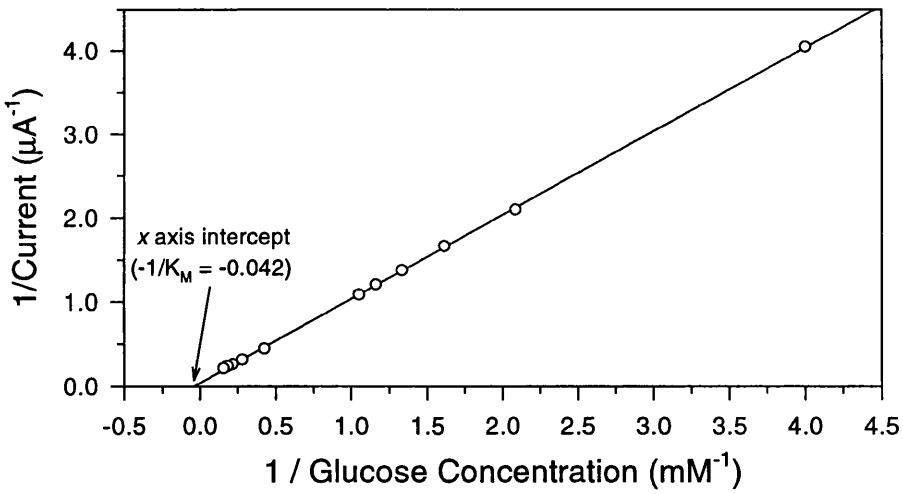

Figure 5.8: A Lineweaver-Burk plot for the 120μg ml^{-1} film used this study (ref. figure 5.9). The value of K_M is 24mM, as determined by the *x* axis intercept of the least squares fit straight line (r^2=0.9998). This result indicates that the entrapment procedure has not altered the activity of the enzyme within the polymer film.

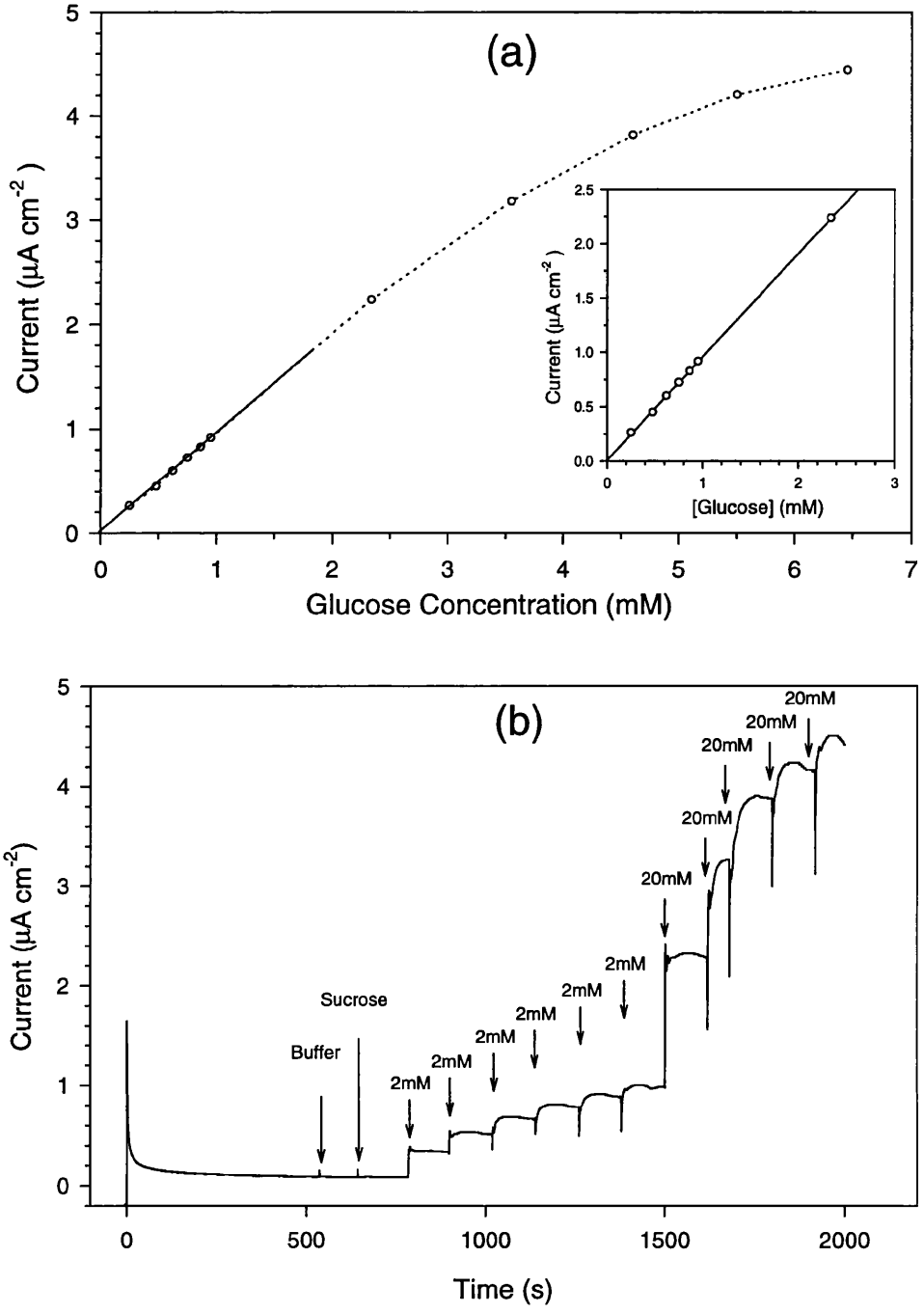

Figure 5.9: The amperometric response of a PPy/GOx film grown from a solution of 150mM pyrrole and 120μg ml^{-1} GOx in 50mM NaCl (pH 4.5). The amperometric response from H_2O_2 was measured at +0.65V (*vs.* Ag/AgCl) in 100mM phosphate buffer (pH 7.4) following additions of either 2 or 20mM glucose at the points marked. The polymer films were grown on RIE cleaned evaporated gold electrodes (area *ca.* 90mm^2). (a) Note the linear response at low glucose concentration (i.e. below 2.5mM), which becomes non-linear at higher concentrations. (b) The original i *vs.* t response is included to illustrate the good speed of response to glucose additions, and the lack of response to control additions of buffer and 20mM sucrose (same buffer), thus demonstrating the specificity and stability of the biosensor response.

5.3 XPS Analysis

This section concentrates on the XPS analysis of the GOx content in PPy/GOx films. Whilst an electrochemical assay can provide data on concentration of active enzyme, XPS can provide data on the total enzyme in the film (e_Σ). The knowledge of e_Σ would be of particular value in kinetic analysis of the electrochemical processes occurring at biosensor interfaces. Data is presented demonstrating how the GOx content can be deconvoluted from the mixed film XPS spectrum, in a manner similar to used for two non-interacting polymers. This provides a simple method of apportioning the true e_Σ *vs.* PPy ratios in a variety of films grown from solutions of different enzyme concentrations.

There have been a range of XPS analyses of protein composition and structure,[187-189] however, there has only been a single study which has used XPS for studying the interaction of GOx at a biosensor interface.[190] In that work, the authors correlated the ratios of the amide (C=O) carbons and the carbohydrate carbon (C-O) environments for GOx adsorbed directly onto bare gold for different lengths of time (with no polymer present). This information was subsequently used to infer that the biomolecular interfacial structure was ordered, such that the polypeptide portion of the enzyme, in contact with the metal, was covered by its carbohydrate shell.

5.3.1 Theory: XPS Analysis

When a solid sample in a vacuum is irradiated with photons emitted from an X-ray source, the photon energy ($E=h\upsilon$) can be absorbed by an electron in an atom of the target. This can result in the ejection of a photoelectron with energy E_k, as illustrated in figure 5.10. The kinetic energy of the emitted photoelectron will be conserved provided that it suffers no further inelastic collisions within the solid. The energy of the emitted photoelectron can be measured to high precision, and using the energy balance relation of equation 5.1, it is possible to determine the photoelectron binding energy (E_b) within the solid.

$$E_b = h\upsilon - E_k - \delta\phi \qquad (5.1)$$

Where $\delta\phi$ represents the contact potential difference between the sample and the spectrometer.

The detector counts the number of photoelectrons at each binding energy. The energy resolution is usually between 0.1-0.5eV and multiple scans together with signal averaging is used to improve signal-to-noise ratio (SNR). Particular binding energies provide a fingerprint associated with specific elements and all elements from the periodic table can be detected except hydrogen. In addition, E_k is dependent on the chemical environment of the ionised atom,

hence, charge delocalisation associated with specific bonds can also be identified. Depth profiling is another option available with XPS analysis. This technique can provide information on the variation of elemental composition up to the maximum depth of 3λ (*ca.* 8nm using an AlKα source), where λ represents the electron mean free path. The principle of the technique is illustrated in figure 5.10, where sampled depth (d or d') varies according to a sine function.

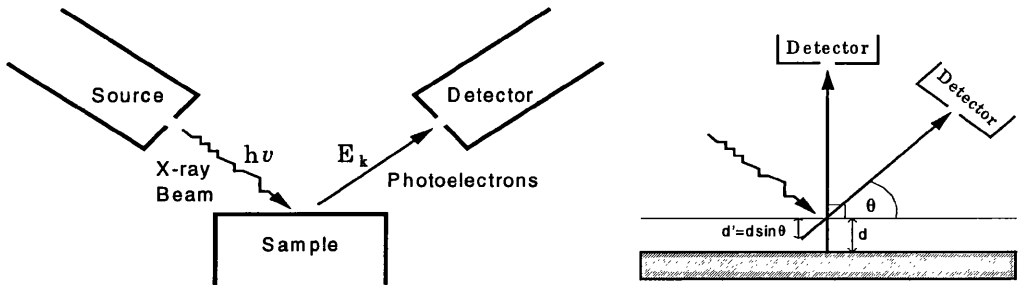

Figure 5.10: The principle of XPS and its use in the depth profiling of surfaces.

5.3.2 Methods & Materials: XPS Analysis

All spectra were collected using the high resolution Scienta ESCA300 spectrometer located at RUSTI, Daresbury Laboratories, UK. The rotating anode source provides AlKα radiation (1486.7eV), which after passing through a monochromator, is focused on the sample. C(1s), N(1s) and O(1s) spectra of the samples were collected with a take off angle (TOA) of 90°. The slit width (0.8mm) and the TOA was kept constant for all of the samples measured, to enable the analysis of the same surface area of polymer, to the same depth. Some of the data presented has been adjusted for the offset due to the floodgun charging effect on non-conducting substrates, using the first component of the C(1s) envelope (binding energy=285.0eV) as a reference.

Polymer films were prepared as described in section 5.1.2, one half of the electrode was used for the XPS analysis and the other half was used in the electrochemical assay. To minimise contamination, the films were stored in the growth buffer (50mM NaCl) during transport. Before analysis, the films were washed in buffer, blown dry and immediately loaded into the spectrometer. GOx reference films on virgin RIE cleaned evaporated gold were prepared by spin coating (2000rpm, 30s) a film from a concentrated solution of enzyme (40000μg ml^{-1}) from 50mM NaCl (pH 4.5)

5.3.2.1 Curve Fitting Methodology

Both the raw data and reference spectra data were prepared by first applying a *x*-axis shift to compensate for flood-gun charging effects, followed by a linear baseline subtraction. The fitting

of the spectra using the prepared reference PPy and GOx reference spectra was based on a least squares method. The curve fitting was performed using application routines written within MATLAB (Mathworks Inc.), which provided the environment for a stand-alone program incorporating all the necessary data processing functions.

When calculating the sum of the errors (Σd^2) most weight was given to the high energy region of the C(1s) spectrum, containing the shake-up (291.0eV) and amide regions, and to the characteristic PPy N(1s) peak at 398.0eV.[171] The low energy side of the C(1s) spectrum, corresponding to hydrocarbon centres characteristic of contaminants, received a minimal weighting. The Gaussian weighting function used in the fitting of the PPy/GOx C(1s) spectra is included in figure 5.16. In order to show that this scheme was valid, the proportion assigned to GOx or PPy used in the composite spectrum was varied by +/-2% and significantly worse fits were obtained.

5.3.2.2 Elemental Quantification- an example

Elements are distinguishable by their different core electron binding energies. The analysis of silicone adhesive, a common substrate in biomaterial research,[191] provides an excellent example of the use of XPS for elemental quantification. The experimental spectrum shown in figure 5.11 has five main peaks associated with its elemental composition (C, Si and O). The adhesive monomer $(SiO(CH_3)_2)_x$ has a simple structure with no major binding energy shifts associated with different chemical environments. Table 5.1 relates the various ratios of C(1s), Si(2p) and O(1s), calculated by analysing the relative areas of the strongest elemental peaks, in addition to adjustments to compensate for detector sensitivity.[192] The measured elemental ratios correspond well to the expected basic ratio of $Si_nO_nC_{2n}$. This illustrates the method by which XPS can be used to determine both elemental composition and their relative ratios.

Element	Sensitivity	Area(counts)	[Atom]/%	Sample Window (eV)
C(1s)	1.0	10769	48.7 (2n)	286.25 - 275.15
O(1s)	2.8	16418	26.7 (n)	533.35 - 523.30
Si(2p)	1.0	5394	24.6 (n)	104.15 - 93.25

Table 5.1: The elemental breakdown of the XPS analysis of silicon adhesive. Comparison of the atom/% ratios suggests a composition ratio of the form $Si_nO_nC_{2n}$, this is in agreement with expected values.

Examples of quantification for variations in binding energy associated with different chemical environments are provided later in section 5.3.4.

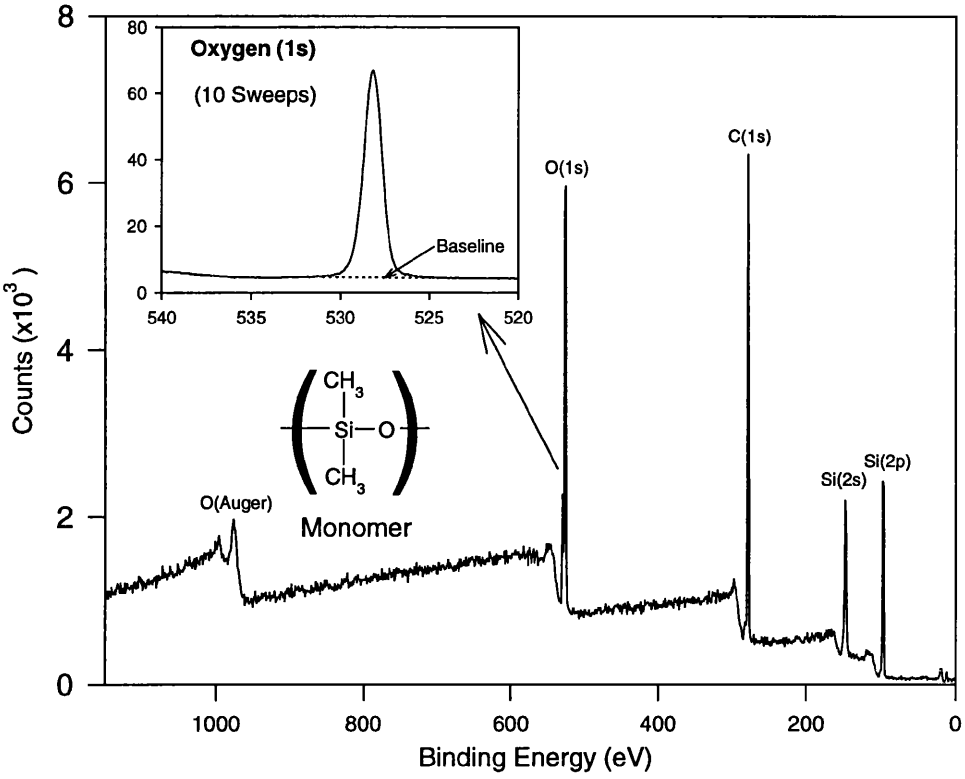

Figure 5.11: An XPS spectrum of silicon adhesive (Dow Corning RTV 3145) for a broad range of Binding Energies between 1150 and 0eV (1 sweep), TOA=90°, slit width=0.8mm, AlKα source. The C(1s), O(1s) and Si(2p) elemental peaks used for quantification are clearly visible. The inset for the O (1s) peak is an example of a high resolution analysis (10 sweeps) used for quantitative analysis, in addition, it provides an example of the linear background subtraction method used in this study. The known structure of the silicon-based monomer is also shown in inset and the quantification results (see table 5.1) correspond well with the expected $Si_nO_nC_{2n}$ ratio.

5.3.3 Results and Discussion

This section has been split into three part dealing with each of the specific aspects analysed during the course of the XPS studies: these are:

1) **Surface Contamination** - the use of XPS to monitor its contribution to recorded spectra, and also as technique to provide indication of the success in new experimental procedures developed to minimise its influence on recorded response.

2) **Gaussian Fitting Technique** - Although not used for the analysis of the PPy/GOx spectra in this study, the Gaussian fitting method is one of the standard techniques used in quantitative XPS. In this study it was used for comparing the C(1s) spectra of as-grown and over-oxidised PPy as a means of assessing the degree and nature of polymer oxidation.

3) **Deconvoluted Analysis Technique** - The analysis of the relative enzyme and polymer components of a range of PPy/GOx films grown at different solution enzyme concentrations.

5.3.3.1 Contamination

XPS is very surface sensitive and the effects of contamination can have a dramatic affect on the analytical accuracy of the technique. For example, figure 5.12a clearly demonstrates the effect of the most pernicious contamination, adsorption of adventicious hydrocarbons. The low C(1s) signal of the sputter cleaned gold sample is significantly increased by only a momentary exposure (1-2s) to the atmosphere, while acid-cleaned (cycled in 1M $HClO_4$) or RO water treated samples show similar contamination related responses. Sample storage in liquid media and minimum air-exposure-time were the practical methods adopted to reduce the effects of contamination

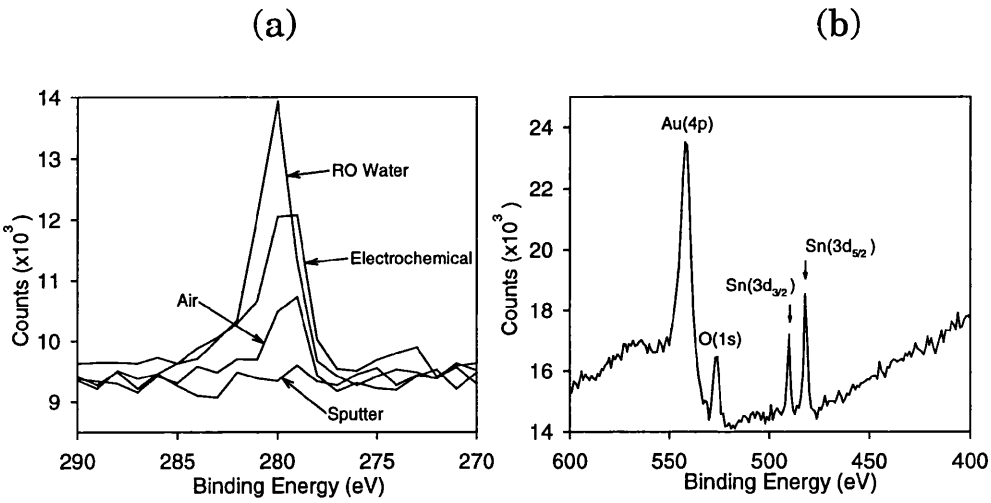

Figure 5.12: (a) The C(1s) XPS spectrum of virgin evaporated gold following the use of four different sample cleaning techniques. Various degrees of adventicious hydrocarbon contamination (spectra not compensated for sample charging) are responsible for the recorded spectra. It is apparent that spectra are very sensitive to such contamination and any exposure to the ambient laboratory environment, even for a few seconds, is likely to produce such a signal. The sputter cleaned sample maintained at a pressure of $<10^{-5}$Torr is the only sample that shows little contamination signal above the background response. (b) The fingerprint of Sn contamination on a thiol treated evaporated gold sample cleaned using RIE etching with an un-encapsulated bonding wire.

A further source of contamination was highlighted by XPS and forced the modification of the experimental procedure. Figure 5.12b also presents the spectrum of an absorbed thiol monolayer on gold, the O and Au signals are as expected, however, the two peaks at 491eV and 483eV were both unexpected. These elemental peaks were eventually identified as tin, the source being metal sputtered from the contact wires during the Reactive Ion Etch (RIE)

cleaning of the bare gold electrodes. This instance was both useful in improving experimental technique and served as an excellent illustration of the surface sensitivity of XPS spectroscopy. Subsequently, the wires used to connect the electrodes were sheathed in glass capillary, the glass being resistant to the rigours of the RIE cleaning procedure.

5.3.4 Gaussian Fitting Technique

Quantification in XPS is routinely performed by deconvolving the data spectrum into a combination Gaussian or Voigt shaped peaks associated with individual bond moieties within the sample.[193] This option was not used in the analysis of the PPy/GOx films for two reasons. Firstly, GOx is composed of 583 amino acids of 21 different types, providing a wide variety of atomic environments whose deconvolution into individual peaks would prove an unreasonably difficult task, prone to error. Secondly, such a deconvolution approach would detract from the overall simplicity of this method of analysis of the biosensor composition.

However, the Gaussian deconvolution technique was found useful in some initial studies on PPy only films, comparing the spectra of as-grown and over-oxidised PPy. Although the electrochemical analysis was performed on PPy-oox/GOx films, it was better to perform the XPS analysis on PPy+ films. A key amide marker point in the GOx occurred at close to the same binding energy as the C=O peak (288.2eV) prominent in the Carbon(1s) spectrum of PPy-oox, its use would have made the fitting procedure less precise.

The characterisation and mechanism of PPy over-oxidation has been a topic of intensive study.[182,194] In addition, its potential as a permiselective biosensor interface has received much recent attention.[183,195] The general conclusions from the literature are that the over-oxidation process is based on the formation of carbonyl pendant groups along the conducting polymer backbone. The over-oxidation process results in a dramatic decrease in film conductivity and expulsion of counterions. The changes in polymer morphology and the charged pendant groups are believed to be give PPy-oox its permiselective properties. Use of XPS and FTIR for accurate elemental analysis of PPy-oox has proved problematic due to the complex mechanism by which oxygen is incorporated into the film, and its dependence on the size and charge of the counterion.[196]

This aspect of the study focused on the differences between the Carbon(1s) spectrum of PPy+ and PPy-oox. The quantification procedure was initiated by a second derivative analysis of C(1s) spectrum to assign initial peak positions. Peaks of fixed width[197] were introduced one at a time until a good fit was obtained. At this point, the constraints on peak widths were relaxed to produce the final fit. The results suggest the existence of six peaks, the suspected sources of these peaks and associated quantification results are illustrated in figure 5.13.

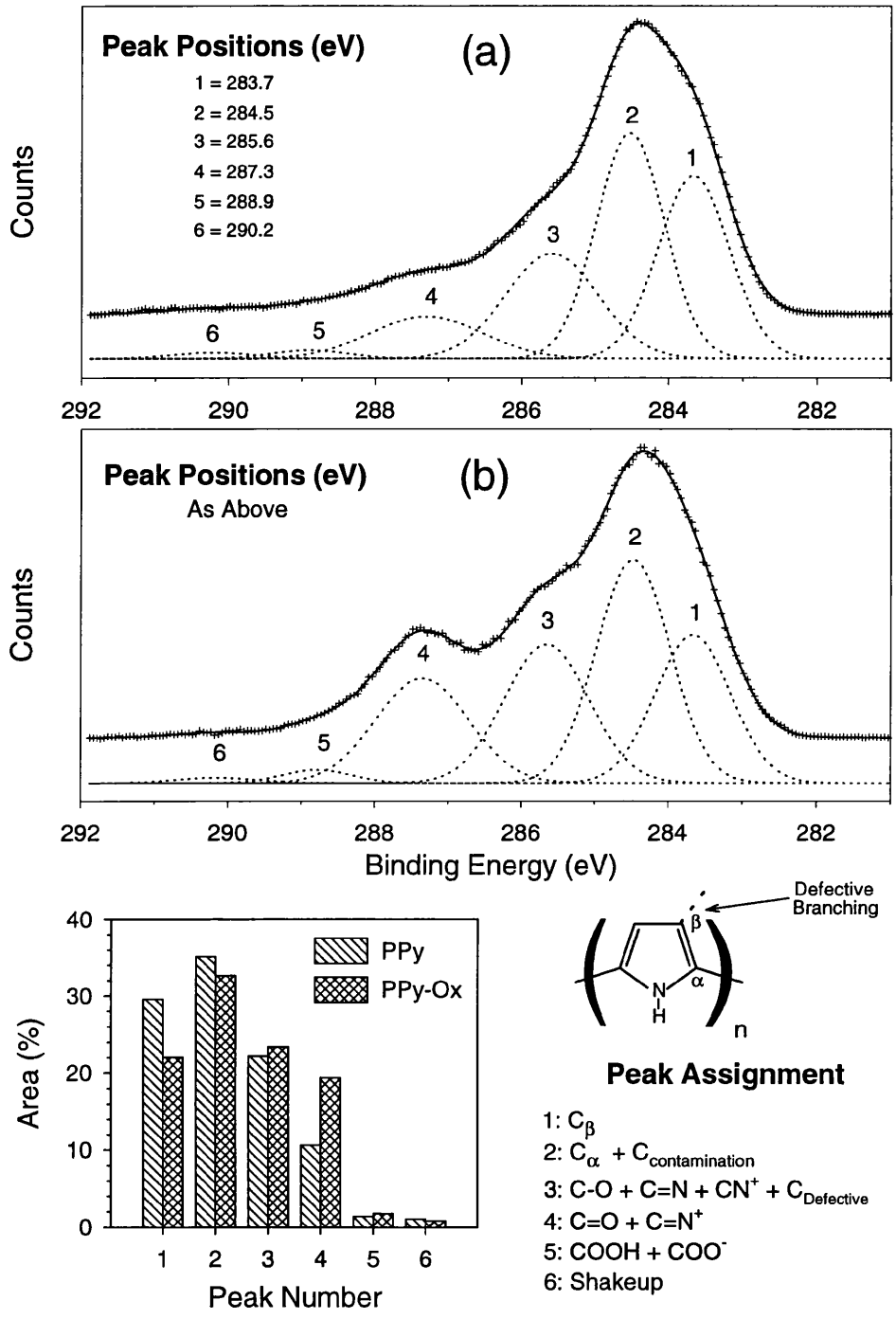

Figure 5.13: The Gaussian deconvolution fitting technique as applied to the analysis of the C(1s) spectrum of as-grown (a) and over-oxidised (b) PPy samples. The samples contained no enzyme component and were prepared as described in section 5.1.2, spectra were recorded at a TOA=90° and slit width=0.8mm using an AlKα source. Gaussian peak positions are the same for both spectra, peak assignments and comparative areas apply to the specified chemical groupings. The structural diagram of PPy highlights the β site, suspected as being the location of any defective branching during polymerisation.

There are three factors apparent from the comparison of peak areas. Firstly, the doubling in peak area 4, primarily related to the increase in C=O species in the PPy-oox. Secondly, the greater decrease in the area ratio of peak area 1 to 2, indicates that the over-oxidation mechanism is more likely to occur at the C_β location in preference to C_α. location (see the structure diagram in figure 5.13). Thirdly, the size and similarity of the magnitudes of peak area 3 in both films, suggests that a significant contribution to this particular peak area is due to defective branching during polymerisation at the β-carbon position instead of the characteristic α-carbon position. If the area of peak 3 was solely a reflection of the contribution of C-O, C=N and CN^+ groups to the Carbon(1s) signal, it should have been of a lower relative magnitude to peaks 1 & 2 and should show a more substantial increase due to the addition of oxidation products following over-oxidation.

These results agree in some part with the analysis of Palmisano *et al.*[183] who observed a similar but more dramatic decrease in the C_β content of the over-oxidised PPy but a broader increase in a range of oxidation products such as C-O, COOH and COO^-. The difference is most likely to be associated with their use of alternative over-oxidation procedure. That is, the slow over-oxidation at 0.7V for five hours, in comparison to rapid over-oxidation by repeated scanned potential of up to 1.2V used in this study. The appearance of a large number of defective branching sites within the polymer matrix agrees with the work of Pfluger *et al.*,[171,198] where they ascribe the defective sites to the locations of cross-linking and bending in the polymer chains.

Further work on the analysis of the differences between the two types of film was not performed due to limited access time to the XPS spectrometer at Daresbury. However, it is hoped that this section has provided an example of where XPS can be used to provided insight into both the elemental and chemical structure of biosensor interfaces.

5.3.4.1.1 Deconvoluted Analysis Technique

In the analysis of the XPS results, the PPy/GOx films were modelled as non-interacting co-polymers, where the two constituent components were the enzyme and the polymer. To illustrate these differences, figure 5.14 shows the C(1s), N(1s) and O(1s) XPS reference spectra for a thick film of GOx and PPy on evaporated gold, the spectrum of a GOx/PPy (420μg ml^{-1}) film is included for comparison. It was found that fit results based on spectra obtained using spin coated GOx reference films were highly reproducible, in contrast to those obtained from GOx physisorbed onto clean gold substrates. The latter spectra, although broadly similar in character, show surface contamination, particularly in the hydrocarbon region of the C(1s) spectrum (285eV).

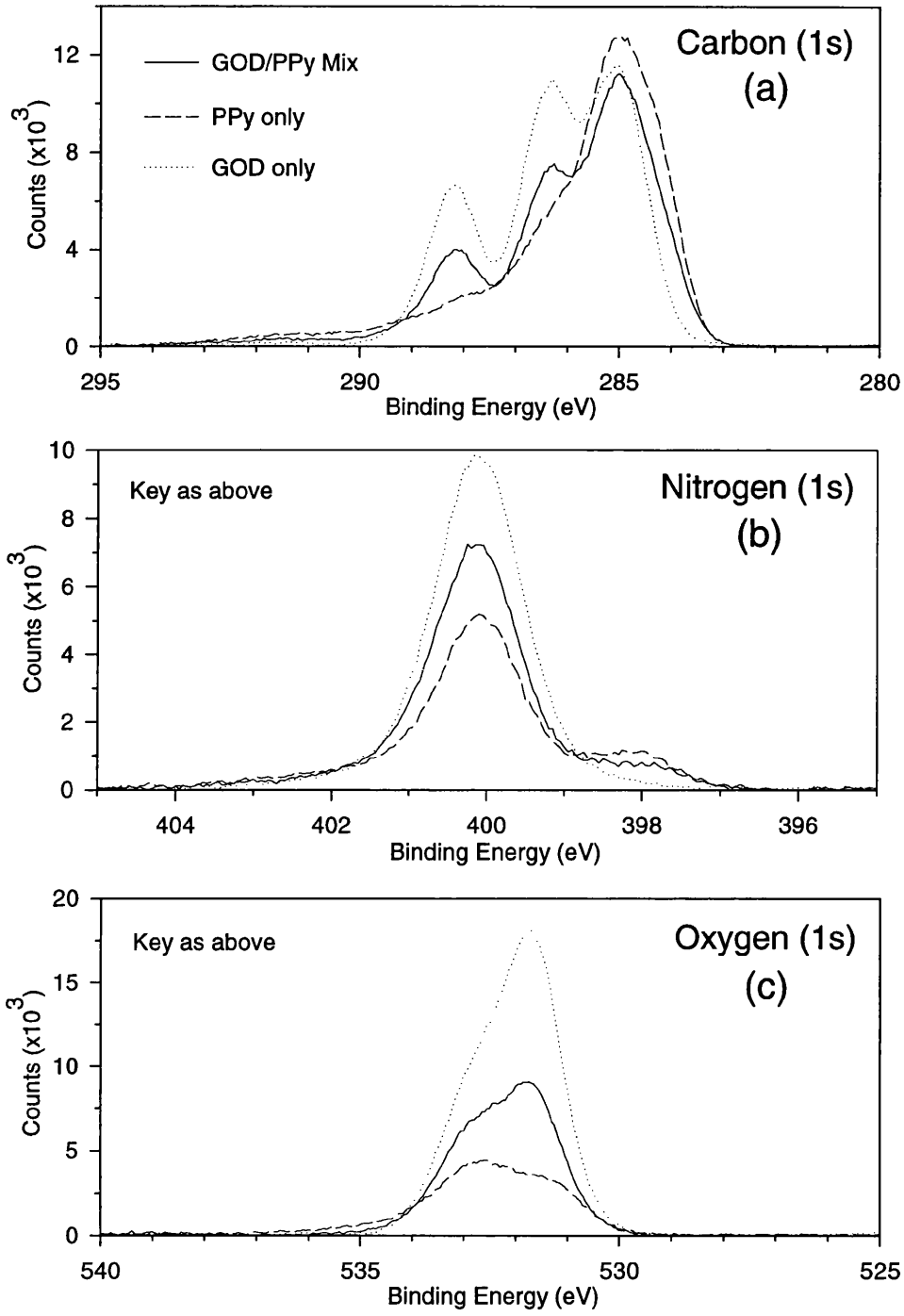

Figure 5.14: The C(1s) (a), N(1s) (b), and Oxygen(1s) (c) XPS spectra of the reference PPy and GOx films used in the deconvoluted analysis technique, the spectrum for a 420μg ml^{-1} PPy/GOx film are included for comparison. All films were prepared on RIE cleaned evaporated gold, the PPy and PPy/GOx films were grown as described in section 5.1.2, the GOx film was prepared by spin coating (2000rpm, 30s) a film of concentrated enzyme solution (40000μg ml^{-1}). Spectra were recorded at a TOA=90° and slit width=0.8mm using an AlKα source.

Comparison of the spectra in figure 5.14 suggests that the C(1s), N(1s) and O(1s) spectral components of the biosensor film may be deconvoluted into a linear combination of both GOx and PPy spectra. This provides a technique for estimating the composition and surface coverage of GOx in the polymer based biosensor. The simple apportionment of the C(1s) spectrum is aided by the characteristic amide peaks in the C(1s) spectrum of GOx at 288.2eV and 286.4eV, corresponding to the C=0 (carbonyl) and N-C-CO- groups respectively. These groups are mostly absent in the C(1s) spectrum of carefully grown PPy films. However, it was noted that if the polymer film was prepared by oxidation at potentials greater than 0.8V *vs.* SCE in aqueous solution, then the spectrum showed evidence of CO or COOH moieties associated with over-oxidation of the PPy (see section 5.1).

Other valuable spectroscopic markers in reference spectra that were helpful for deconvoluting the spectra of the biosensor films include:

1. The high energy tail of the C(1s) spectrum, which corresponds to the shake-up region associated with aromatic hydrocarbons.
2. The small peak in the N(1s) spectrum at 398.0eV, which is related to charged nitrogen species in the PPy,[171] and is completely absent in the GOx spectrum.
3. The O(1s) peak at 531.7eV primarily associated with additional signal from entrapped GOx.

These spectroscopic markers along with their variation in a range of PPy/GOx films used in this study are shown in figure 5.15.

5.3.4.1.2 Data Analysis and Discussion

Figure 5.16 shows an example fit result for the C(1s) spectrum of the PPy/GOx biosensor film prepared from a solution containing 120μg ml^{-1} enzyme. Both the weighted and un-weighted fit are shown, and it can be seen how the weighting provides a better fit to the two amide peaks and the shake-up region. Furthermore, the reduced magnitude of the fit spectrum at 285.0eV suggests that the weighted fit is a superior fit with relation to hydrocarbon contamination, while not significantly altering the overall shape of the spectrum. Figure 5.16 also provides similar examples of the fit curves for the N(1s) and O(1s) spectra of the same 120μg ml^{-1} PPy/GOx film.

A summary of the respective C(1s), N(1s) and O(1s) fit parameters of all the films analysed in this study are given in Table 5.2.

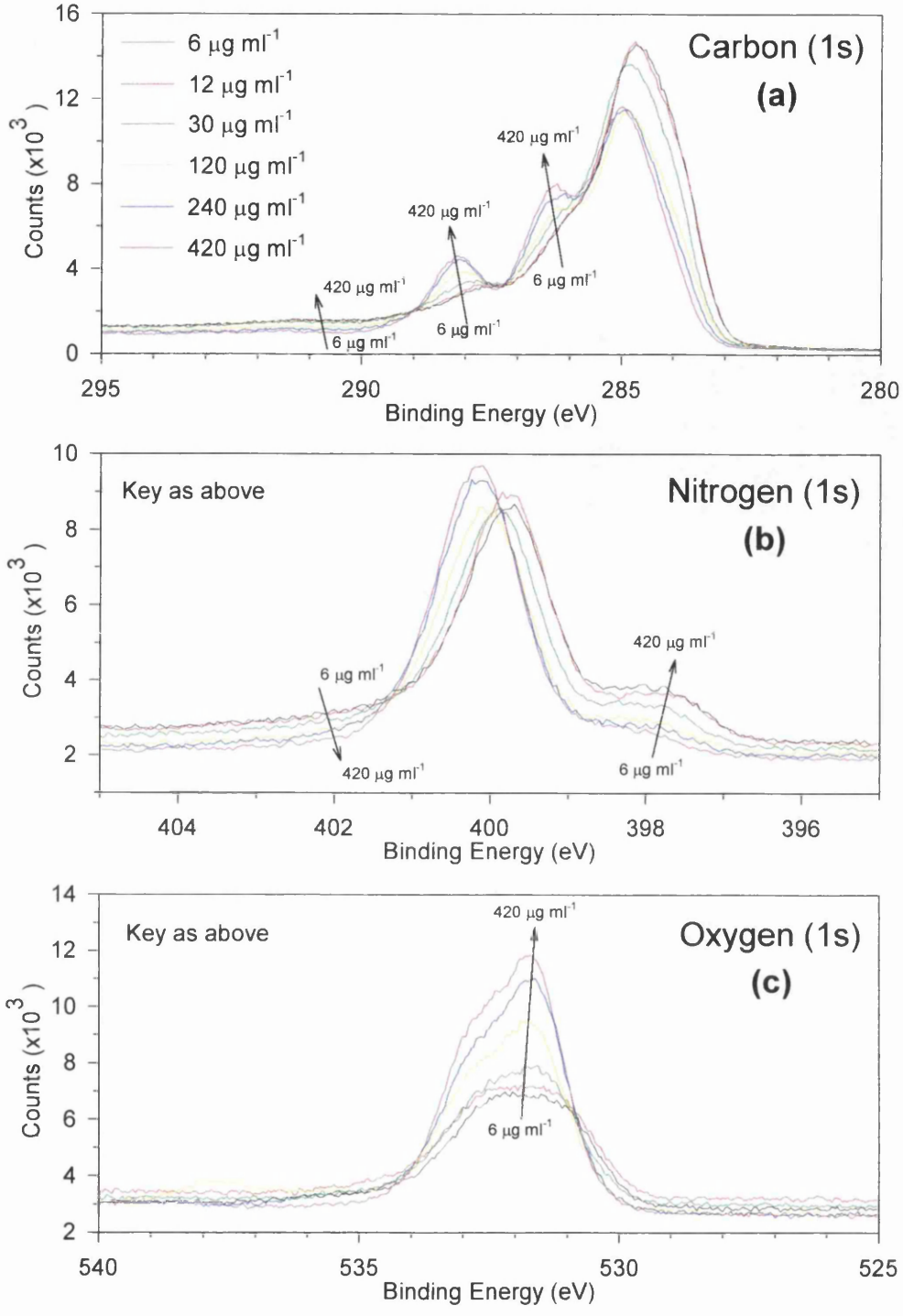

Figure 5.15: The C(1s) (a), N(1s) (b), and O(1s) (c) XPS spectra of PPy/GOx films grown from a range of solution enzyme concentrations (6-420μg ml^{-1}). Films were prepared as described in section 5.1.2, spectra were recorded at a TOA=90° and slit width=0.8mm using an AlKα source. Note the variation of the key markers (arrows) used in the fitting procedure and their change with increased enzyme concentration.

[Enzyme]	Carbon(1s)		Nitrogen(1s)		Oxygen(1s)	
($\mu g\ ml^{-1}$)	%Polymer	%Enzyme	%Polymer	%Enzyme	%Polymer	%Enzyme
6	96	3	99	2	--	--
12	93	6	95	4	--	--
30	85	12	95	12	67	13
120	65	31	75	25	58	25
240	50	41	68	39	54	34
420	39	47	61	44	51	41

Table 5.2: The relative proportions of polymer and enzyme content in a range of PPy/GOx films. The values were determined from the best-fit of a least squares fitting procedure using the percentile combination of the PPy and GOx reference spectra.

Due to the lack of a distinctive marker in the O(1s) spectrum, the lower enzyme concentration films could not be given a valid fit and are omitted in table 5.2. For example, referring to the "6$\mu g\ ml^{-1}$" film spectrum (see figure 5.15), the data does not contain the distinctive GOx related shoulder at 531.8eV and a greater than 2% variation in parameters could produce an equally valid fit.

Figure 5.17 shows the variation in enzyme percentage for the different PPy/GOx films. The variation for the different elemental spectra is associated with their relative absolute magnitudes in the GOx and PPy reference spectra, presented in table 5.3 (see also figure 5.14). The area magnitudes of the C(1s) spectra are similar, whereas there is a dramatic difference in the relative contribution of the O(1s) spectra due to the much larger oxygen content of GOx. The differences in magnitude are related to the variation in physical parameters, primarily mean free path (λ), in the reference spectra and the associated variation in the X-ray penetration depth (d).

Element	Sensitivity	Area(Counts)		[Atom]/%(C, N, & O)		Sample Window
		PPy	GOx	PPy	GOx	(eV)
C(1s)	1.00	35252	37685	76.3	62.5	282-295
N(1s)	1.73	10627	15547	13.3	14.9	396-406
O(1s)	2.80	13498	38069	10.4	22.6	527-539

Table 5.3: A comparison of the relative contributions of PPy and GOx to the corresponding C(1s), N(1s) and O(1s) signals. Note the difference in the O(1s) Atom% signal of GOx in comparison to that of PPy, this is in contrast to their almost equivalent contributions to the C(1s) and N(1s) signals.

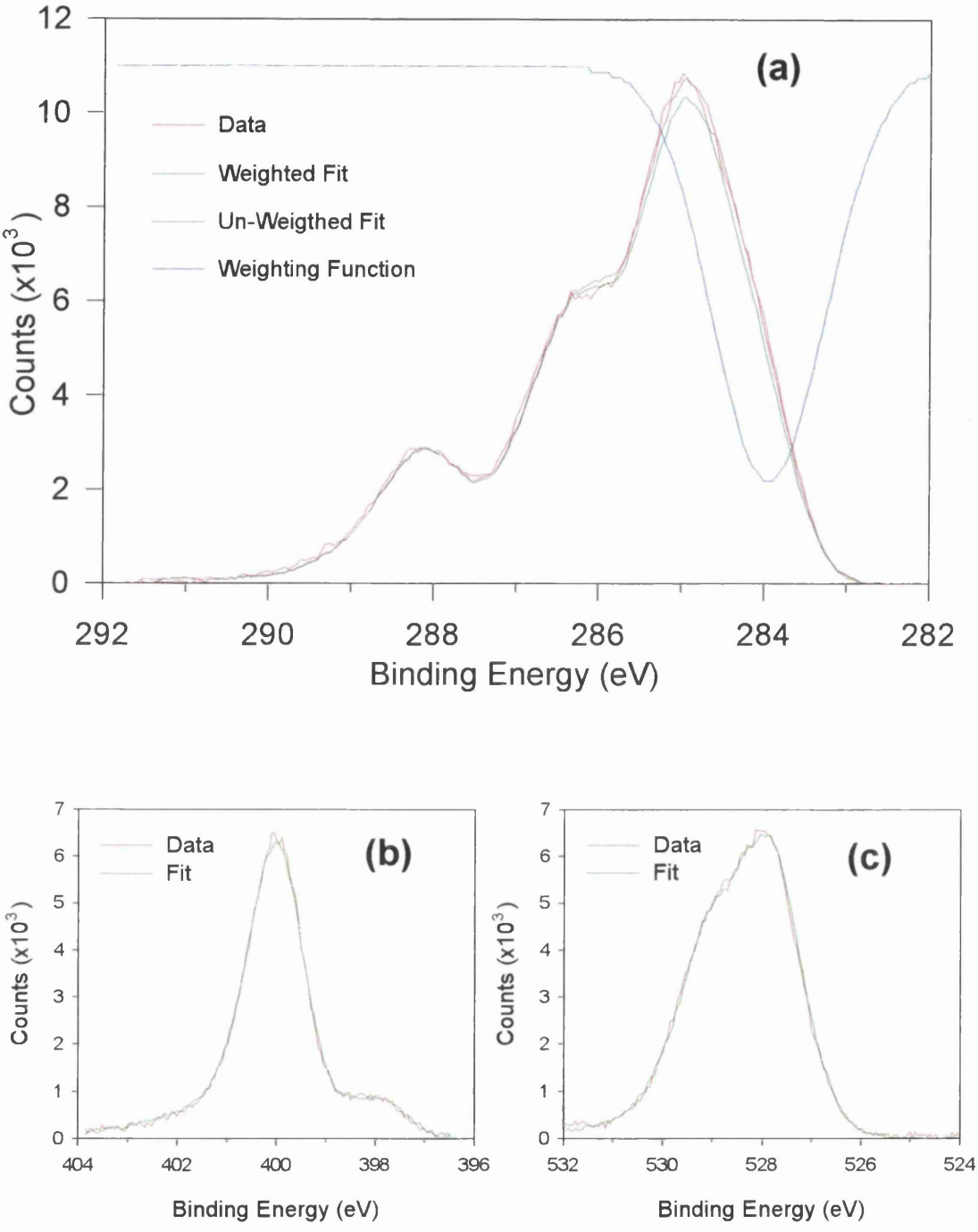

Figure 5.16: A comparison of the C(1s) (a), N(1s) (b), and O(1s) (c) data and fitted XPS spectra for a 120μg ml^{-1} PPy/GOx film. The film was prepared as described in section 5.1.2, spectra were recorded at a TOA=90° and slit width=0.8mm using an AlKα source. The C(1s) spectrum (a) includes an illustration of the weighting function used in the fitting procedure. Note the better fit to the amide markers (288.2eV and 286.4eV) provided by the weighted fit in comparison to that of the unweighted fit.

Comparison of the two reference spectra suggests that the penetration depth in GOx is greater than in PPy. Hence, the measured elemental contributions would be biased towards any signal from the enzyme. This bias would be magnified by any differences in absolute area magnitudes between the PPy and GOx reference spectra, the O(1s) spectrum would be the worst case in this instance. For this assessment, the equivalent areas, in addition to the greater number of marker points available, suggests that the fit of the C(1s) spectrum in the most reliable. Further work is required to account for the variation of penetration depth with enzyme concentration. This would add a third parameter into the above fitting mechanism that could potentially improve the accuracy of using this technique for the estimation of e_{Σ}.. Furthermore, the effects of path length variations go some way to explaining why the total percentages in table 5.2 (i.e. polymer + enzyme) do not always add up to 100%.

Finally, a degree of empirical analysis can be performed on the XPS data. It is apparent that a linear variation in enzyme concentration will not produce a linear variation in enzyme content within the film. As an illustration, consider the comparison of the fit data for the C(1s) spectrum of the 420μg ml^{-1} and the 30μg ml^{-1} PPy/GOx films. The results (table 5.2) indicate that the surface concentration of the 420μg ml^{-1} film is 47%, and the 5μg ml^{-1} film corresponds to 12%, of that in the spun cast film of GOx.

Given the diameter of GOx to be *ca.* 10nm,[199] then this would suggest that the surface coverage of enzyme within the 420μg ml^{-1} polymer film is *ca.* $7.8x10^{-13}$mol cm^{-2} and $2.0x10^{-13}$mol cm^{-2} in the 30μg ml^{1} film. Although this method of estimating the amount of GOx at the surface may seem to be crude, the value which we use for coverage in the spun GOx film ($1.66x10^{-12}$mol cm^{-2}) corresponds very closely to that experimentally obtained.[200] Interestingly, whilst the concentration of GOx in the deposition solution was decreased 14 fold between the 420μg ml^{-1} and 30μg ml^{-1} films, there was only a concomitant 4 fold decrease in the enzyme composition within the biosensor films.

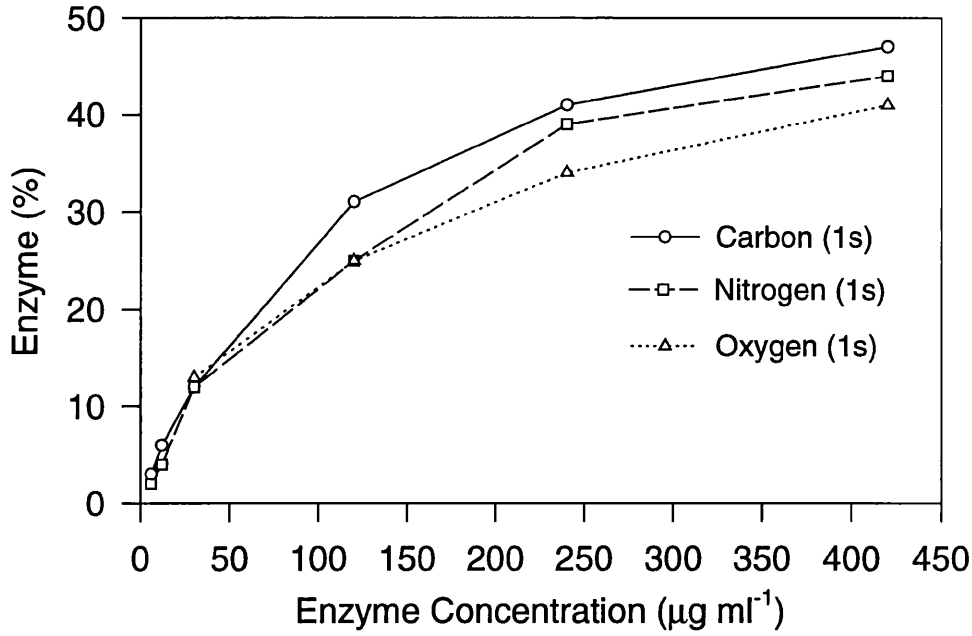

Figure 5.17: A comparison of the XPS derived enzyme content within the film *vs.* enzyme concentration in the polymerisation solution. Solution enzyme concentration was varied between 6-420μg ml^{-1} and the films were prepared as described in section 5.1.2. Note the similar non-linear variation of C, N and O data in enzyme concentration between biosensor film and growth solution.

5.4 FTIR Analysis

FTIR was the third analytical technique used in this study to investigate the loading of GOx in the PPy biosensor films. Whereas XPS is a surface analysis technique providing data primarily on elemental composition, FTIR is a bulk analysis technique providing data primarily on molecular bond composition. Both techniques, when used in conjunction with the electrochemical analysis of active GOx, provide a comprehensive picture of the concentration and activity of GOx within the PPy matrix

5.4.1 Theory: FTIR Analysis

Chemical bonds undergo a variety of perpetual movements such as stretching, twisting and rotating. The energy of most molecular vibrations corresponds to that of the infrared (IR) region of the electromagnetic spectrum. IR spectroscopy is sensitive to the vibrations that lead to changes of dipole moment within molecule.

A gas phase species has 3N degrees of freedom corresponding to three degrees of kinetic freedom, where N represents the number of atoms in the species. For a non-linear molecule, six of these vibration modes can be discounted, for they represent purely translational and

rotational motions (three of each). This leaves a possible 3N-6 modes of vibration, or 3N-5 for a linear molecule where the rotational mode along its molecular axis cannot occur. As an illustration, consider a water molecule, it will have three fundamental modes of vibration and these are shown in figure 5.18.

IR spectroscopy relies on the fact that if a rotation or vibration gives rise to a change in dipole, the electromagnetic radiation can interact with this dipole through a resonance process. Resonance with incoming radiation results in an absorbance of radiation, usually recorded as a percentage transmission. In an attempt to avoid the high frequencies (typically 10^{12}-10^{14}Hz) associated with molecular absorptions, IR spectrum absorbances are recorded relative to the associated wavenumber in the units of cm^{-1}.

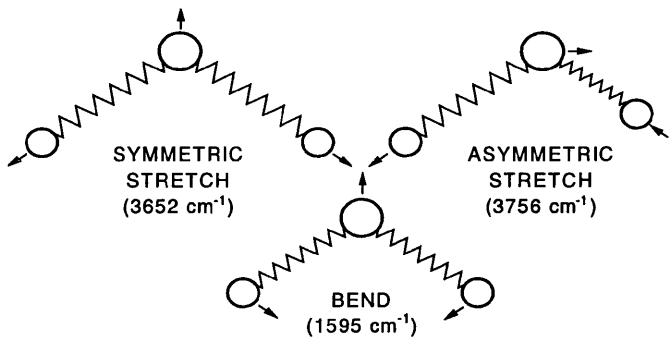

Figure 5.18: The three fundamental modes of vibration for a water molecule and their corresponding absorption wavenumber.

The advent of computerised Fourier-transform spectroscopy has led to many improvements to the original techniques of IR spectroscopy. In comparison to the dispersive IR apparatus and the stepwise collection of data, interferometric techniques permit data from the entire spectrum to be recorded simultaneously. Advantages offered by the FTIR technique include: improved resolution, sensitivity and frequency accuracy.[167,201] Practically, these are observed in the reduced experimentation time and improved SNR.

A larger molecule, such as a protein, will have many more modes of vibration than the simple water molecule shown above. Fortunately, however, many of the vibrations can be localised to specific bonds or groups. Characteristic groups of interest when analysing proteins include C=0, -COOH, C00-, O-H and S-H. Protein analysis using FTIR tends to concentrate on the modes associated with the groups of the peptide bond.[202-204] These can be grouped into three bands the amide I, II and III. The amide I (1600-1700cm^{-1}) band is principally associated with the vibration of peptide C=O group. The amide II (1400-1500cm^{-1}) band is primarily N-H bending with a contribution from C-N stretching vibrations. The amide III (1200-1300cm^{-1}) band is very weak in the vibrational IR, arising from N-H bending. The incidence of these

amide bands in GOx (experimental data) is shown in figure 5.19. The amide peak positions correspond well with those observed by Fiol *et al.*[205] during their FTIR analysis of behenic acid/GOx Langmuir-Blodgett films.

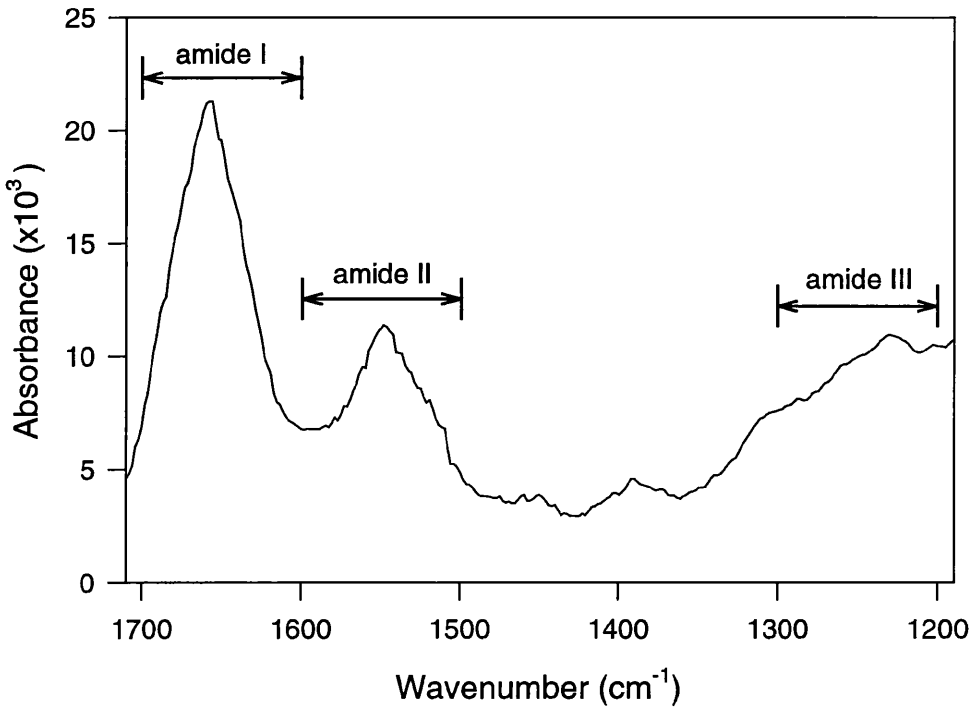

Figure 5.19: The FTIR spectrum of GOx physisorbed onto an RIE cleaned evaporated gold from a solution of 40000μg ml^{-1} enzyme in 50mM NaCl. Note the characteristic amide I, II and III regions in the spectrum associated with peptide bond absorptions within the enzyme.

The majority of FTIR research in related fields has investigated polymers and proteins separately. FTIR is used as a standard technique in polymer analysis,[206,207] and with particular relevance to this study, has been used as a means of in-situ analysis of conducting polymer growth mechanisms.[28,194] The use of FTIR in protein analysis has received much attention in the past ten years, primarily as a means of protein secondary structure analysis.[208-210] To a lesser degree, it is being used as a method of quantifying protein absorption rates.[211] There is little work on the simultaneous analysis of both polymers and protein constituents, although FTIR has found a role in biomaterial research as a means of analysing the nature and speed of protein fouling of implant materials.[212] In this study, the variation in magnitude of the amide bands in the various ratio PPy/GOx film were compared to the individual component spectra. Deconvolution of the mixed spectra provided a means of quantifying the relative amounts of enzyme in each film.

5.4.2 Methods & Materials: FTIR Analysis

The films were grown as described in section 5.1. Exactly the same PPy/GOx films were used in the FTIR experiments has been used in the XPS analysis described earlier (see section 5.3). Following the removal of the film from the XPS spectrometer, the films were immediately stored in a sealed container. Control experiments were performed to ensure that the XPS analysis resulted in no significant damage or encouraged degradation processes in the polymer films.[212]

The FTIR experiments were conducted within 48 hours of the films being analysed by XPS. A Bomem MB-102 FTIR spectrometer with a mercury cadmium telluride (MCT) detector was used to collect the spectra. The spectrometer was used in grazing-incident reflectance (GIR)[213,214] mode using p-polarised light at an incident angle of 80°. Spectra were recorded at $4cm^{-1}$ resolution with an iris aperture of 8mm. The data was processed and analysed using a PC-AT computer running Bomem-Easy (v. 1.41) software. A reference spectrum from RIE cleaned evaporated gold was collected for each sample to minimise the possible errors from contaminant (particularly water) adsorption. The data was initially recorded as transmission spectra and then numerically converted into absorption values.

In addition to the spectrum of 'spun GOx' used in the XPS analysis (see section 5.3.2), a physisorbed enzyme spectrum was also collected. The spun GOx sample was too thick (*ca.* 1μm) and provided a poor definition spectrum, due to its low transmission. The physisorbed spectrum was used for comparative work since it provided greater peak accuracy and resolution. The spectrum (see figure 5.19) was recorded from the enzyme physisorbed onto RIE cleaned evaporated gold that had been coated with GOx ($40000\mu g\ ml^{-1}$) from 50mM NaCl buffer, left to absorb for 30 minutes, and then washed in buffer and blown dry with nitrogen.

5.4.3 Results and Discussion

For the reasons highlighted earlier (section 5.4.1), it was decided to analyse the enzyme loading in the sensor films by focusing on the changes in the amide component of the films. Figure 5.20 shows the raw FTIR transmission data obtained for a range of these films as well as the spectrum for PPy alone. It is apparent that the enzyme containing films have additional absorbances corresponding to amide I and II bands. However, the amide III band is both weak (as expected) and concealed by the more dominant PPy absorptions in the range $1200\text{-}1300cm^{-1}$. These absorptions have been previously assigned to ring and C-N stretches in PPy.[194]

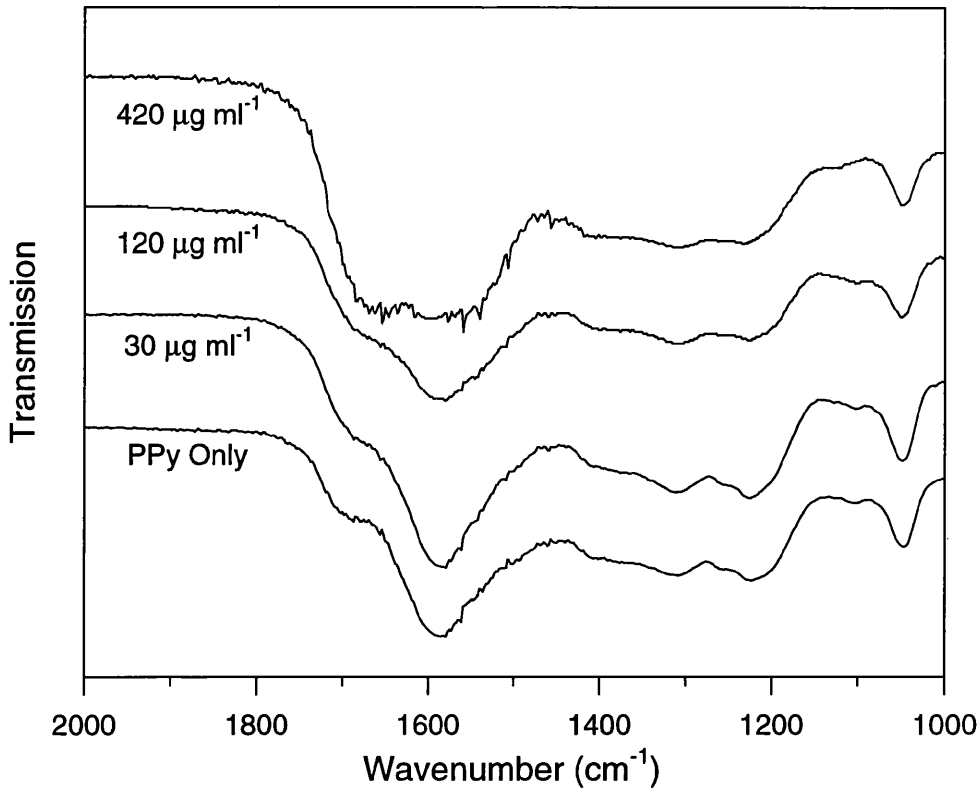

Figure 5.20: The raw FTIR transmission data covering the range of PPy/GOx films used in this study, the spectrum of solely PPy is included for comparison. Spectra were recorded using GIR FTIR on films prepared on gold substrates at an incident angle of 80°, further details on sample preparation and data acquisition are provided in sections 5.1.2 and 5.4.2, respectively. Note the reducing transmission at the amide I (1600-1700cm^{-1}) and II (1400-1500cm^{-1}) markers bands in films grown at increasing solution enzyme concentration.

To compare the relative amide absorptions, a degree of data processing was performed in three steps. The first step was data normalisation for all the transmission spectra at a non-energy-absorbing point - 2000cm^{-1} was chosen as a suitable wavenumber. The second step involved conversion of the spectra into the standard representation as logarithmic absorption values. The third and final step was the data fitting of the PPy/GOx film spectra using the separate reference spectra. This analysis produced a relative ratio of GOx component *vs.* PPy component absorption in the sensor films

The above data processing is similar to the baseline correction procedures used in many analytical techniques and used in quantitative FTIR.[215] For example, in protein absorption analysis, the background substrate signal is recorded first, and then subtracted from the combined signal once the protein has been absorbed to the substrate. The final absorption can thus be assigned to the protein and is called a 'difference spectrum'.

A similar procedure could be used for the analysis of PPy/GOx films, for instance, by treating the PPy signal as the background signal. Unfortunately, this approach is not satisfactory since the PPy component of the PPy/GOx films is a not constant and will vary with polymer thickness, surface roughness and density differences in the sensor films. Taking these differences into consideration, a direct film by film comparison of enzyme concentration could not be made. However, using the data fitting technique similar to that used in the XPS analysis (see section 5.3.2.1), a ratio of GOx/PPy content in each film could be determined that would provide a guide to the relative enzyme component in each film.

A full mathematical treatment of this data fitting procedure is given in appendix B. In summary, the ratio required for the best fit spectrum was determined by the division of the relative proportion of the reference GOx spectrum *vs.* the relative proportion of the reference PPy reference spectrum. The value of the ratio is an indicator of the relative GOx/PPy component in each film. This fitting procedure is illustrated in figure 5.21 for the 240μg ml^{-1} film and the numeric data is shown in table 5.4.

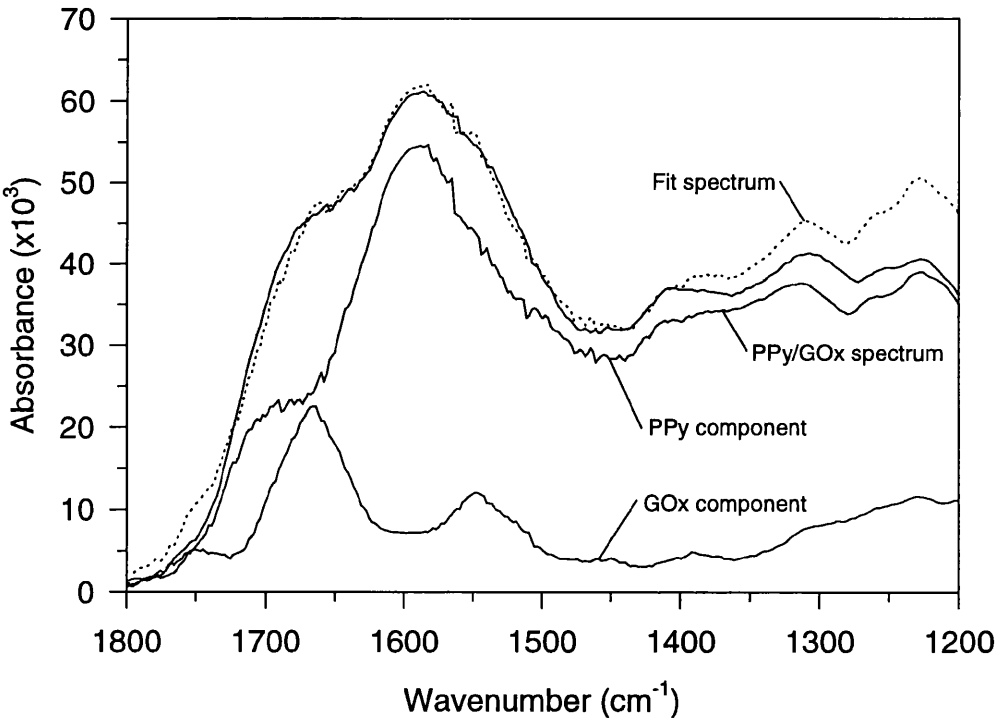

Figure 5.21: An illustration of the fitting procedure for the 240μg ml^{-1} film. The figure includes the experimental data, the fit spectrum, and the individual components of the GOx and PPy reference spectra.

[Enzyme] /μg ml^{-1}	Normalisation Factor	Data Fitting Results		
		GOx component	PPy component	GOx/PPy ratio
6	0.97	-.-	-.-	-.-
12	1.02	-.-	-.-	-.-
30	0.96	0.31	0.99	0.31
120	0.87	0.81	0.88	0.92
240	0.97	1.10	0.83	1.33
420	1.19	1.40	0.79	1.77
PPy ref.	0.90	0.0	1.0	-.-
GOx ref.	1.06	1.0	0.0	-.-

Table 5.4: The data fitting results for the FTIR analysis of the PPy/GOx films. The increasing GOx/PPy ratio reflects the increasing enzyme content in the sensor films. The variation of the ratio with solution enzyme concentration is illustrated in figure 5.22.

There is a clear non-linear variation between enzyme concentration in the preparation solution and bulk enzyme concentration within the film (see figure 5.22). However, unlike the XPS analysis (see section 5.3.3), a comparison of enzyme content in each of sensor films is more difficult as the technique does not provide a direct measure of the GOx or PPy content. Only the GOx/PPy ratio can be determined, so providing an indicator of the relative enzyme composition of each film.

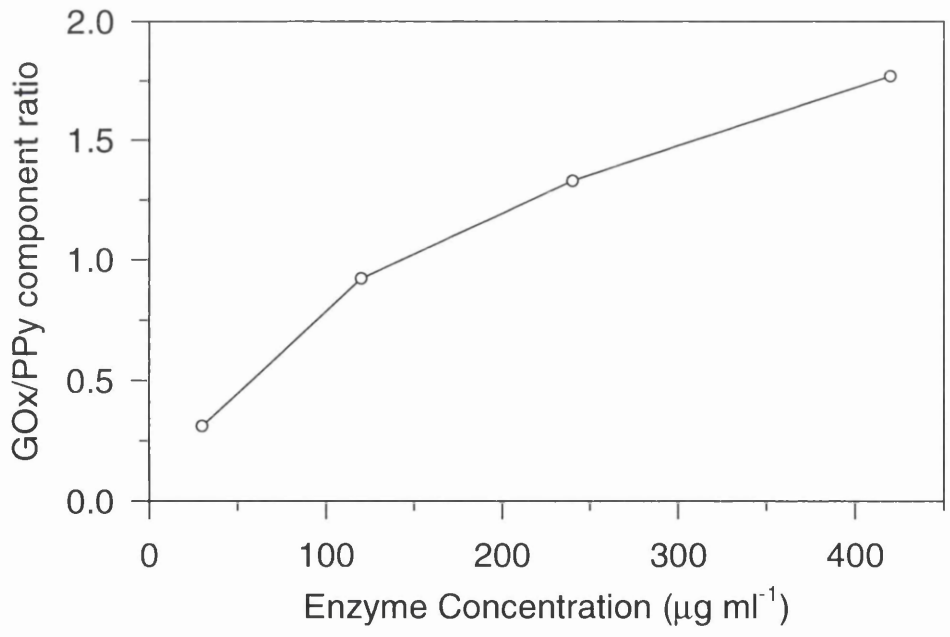

Figure 5.22: A comparison of the GIR FTIR derived GOx/PPy ratio within the film *vs.* enzyme concentration in the polymerisation solution. Further details on sample preparation and data acquisition are provided in sections 5.1.2 and 5.4.2 , respectively. Note the non-linear variation of enzyme concentration within the sensor film with increasing enzyme concentration in the polymerisation solution.

Satisfactory data analysis on the low enzyme concentration films was not possible since a greater than +/-2% variation in PPy or GOx components produced equally valid fits. The fitting of the higher enzyme concentration films focused on the region between 1400-1800cm^{-1}, the region that included the distinctive enzyme amide I and II bands not apparent in PPy only films. The removal of the non-linear MCT detector function would undoubtedly aid the analysis process. It has also been suggested that the collection and analysis of a s-polarised light spectrum could be used to eliminated the non-linear background.[201] Unlike the p-polarised radiation used in this study, s-polarised radiation would not be absorbed by the film, the signal providing data solely on the reflective properties of the sample.

Increasing the SNR of the recorded signal would also improve the sensitivity of the analysis technique. A common method of improving SNR used in IR protein studies is attenuated total reflection (ATR) FTIR, which uses the accumulation of response from multiple reflections to significantly improve the SNR. Unfortunately, the technique is not easily applicable to conducting polymer studies due the need for a transmitting non-metallic substrate. Further studies are recommended to concentrate on improving the experimental technique and reducing experimental error. For example, theoretical work has demonstrated that SNR is dependent on grazing angle, substrate metal and accurate focusing of the IR beam.[213] In addition, experimental apparatus to maintain a fixed path length would reduce any errors associated with the normalisation procedure. A larger sample size would also be an advantage in reducing alignment errors. Measurements in an evacuated inert atmosphere would reduce the effect of contaminate absorptions, to this end, a glove box to enclose the sample chamber is under construction.

For reducing experimental errors, the control of film morphology is the chief concern. For each film, the nature of the nucleated PPy growth mechanism[169] makes the film thickness and topography dependent on both current density and chemical conditions.[158,216] As a result, films can become thicker at the electrode edges due to field non-uniformity, and rougher as increasing enzyme concentrations foul/block the polymerisation electrochemistry.[175] Edge effects could be reduced by enclosing the electrode edges in an inert compound such as silicone rubber. Whilst novel methods of growing "smoother" PPy by the use thiol-pyrrole monolayers[217] provide interesting pathways for further research. Finally, apart from the minimisation of experimental errors, a greater depth of mathematical analysis to compensate for the errors associated with Specular/Fresnel reflection (i.e. Krammers-Kronnig correction[218]) and diffuse reflection (i.e. Kubelka-Monk correction[201]) are likely to prove worthwhile.

5.5 Summary

While XPS has been used to study the interaction of biological molecules at bare and at polymer surfaces, the result of a literature search suggests that this is the first time that it has been used to investigate the interaction between entrapped proteins and polymers at a biosensor interface. The use of a parallel electrochemical assays to determine active enzyme concentration and FTIR analysis of the enzyme concentration in the bulk of the film provides further corroborative evidence to the major conclusion of this study - that the concentration of enzyme in the polymerisation solution is a poor guide to the concentration of enzyme entrapped in the polymer matrix.

All three techniques demonstrated a similar non-linear variation of enzyme concentration, and a comparison of the results is shown in figure 5.23. Other studies have observed similar variations in enzyme concentration,[166,173] based solely on electrochemical assay results, but have either failed to fully address the issue or have explained the non-linear response in terms of diffusion limitation within the biosensor film. It is hoped that this study has provided conclusive evidence that any assumptions made regarding the enzyme content of PPy/GOx biosensor films and solution enzyme concentration should be treated with great caution.

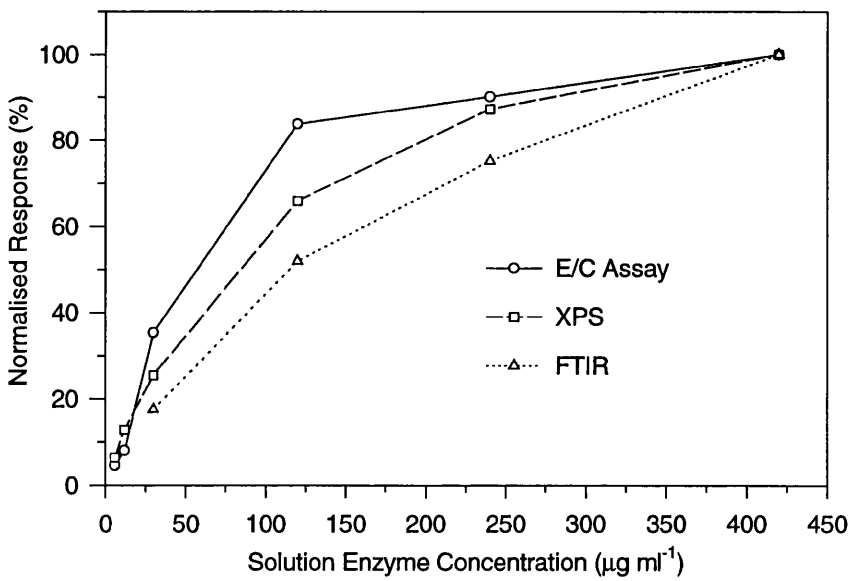

Figure 5.23: A comparison of the non-linear variations of the measured enzyme concentration within the PPy/GOx films *vs.* the variation of enzyme concentration (6-420µg ml^{-1}) in the polymerisation solution for the three analysis techniques used in this study. The *y* axis values have been normalised to the response of the highest enzyme concentration (420µg ml^{-1}).

The results from this study provides significant scope for further similar work on biosensor interfaces, both on alternative polymer/enzyme systems and in terms of improving the accuracy of the current methods. For example, the use of this methodology is currently under investigation as a means of analysing enzyme content in poly(o-phenylenediamine)/GOx films. Whilst, further investigation into the characterisation of PPy/GOx films and reduction of noise in the FTIR spectra provide two clear examples of areas where any improvements would benefit the accuracy of this analysis methodology.

6. Conclusion

This project has explored a variety of aspects within biosensor technology. Initially, the issues of biosensor fabrication were investigated, and in the later stages, the work progressed towards the issues of biosensor sensitisation and characterisation. The investigation of the phenomenon of dielectrophoresis to position cells for electrochemical analysis provided an opportunity to explore the dual function of the two markedly different techniques. It was disappointing that the detection of the superoxide release from single cells was hindered by factors such as insulator adhesion and the preparation of an effective electrochemical surface. However, the three components of the superoxide sensor (dielectrophoretic particle positioning, electrochemical superoxide assay, and microfabrication) were successfully demonstrated in their own right, the difficulties only becoming apparent when the components were combined.

The techniques of photolithography and e-beam lithography for biosensor fabrication were developed during the project. The problem of poor sensor reliability due to poor adhesion was identified and methods are suggested for overcoming this problem. For example, the use of a titanium 'overlayer' to improve metal to insulator adhesion presents significant promise for future work. Fabrication of 'gold-only' structures using MPS as an adhesion promoter will permit the elimination of interfering currents caused by the diffusion of underlayer metals (e.g. Ti or Cr) into gold working electrodes. The success of this fabrication protocol using photoresist treated substrates makes the procedure even more inviting for use in biosensor fabrication

An unachieved goal of the project was the development of an effective procedure for the covalent immobilisation cytochrome *c* on a microfabricated electrode for superoxide detection. The procedure was successful for macro-sized electrode prepared using standard polishing techniques. Unfortunately, these techniques are not feasible for planar microfabricated biosensors. However, the effectiveness of the Ar/O_2 RIE cleaning protocol, developed during the project, was demonstrated as an alternative preparation procedure for the observation of solution-phase cytochrome *c* electrochemistry. Furthermore, the cleaning protocol proved invaluable during the preparation of clean gold surfaces necessary for the uniform electopolymerisation of pyrrole in the work on PPy/GOx biosensor interfaces.

The use of dielectrophoresis for particle positioning and manipulation proved very successful. Electrode designs and experimental procedures for confining a range of particles were developed and tested. This work was able to integrate effectively with the sensing procedures,

not only as a means of particle positioning but also as a method for detecting the physical processes that occur following the chemotactic stimulation of human neutrophils. The electrorotation experiments highlighted physical changes occurring within the cell wall and cytoplasm. Potential mechanisms were identified and modelled in terms of the changing electrical parameters of the cellular elements. The choice of neutrophils for the electrorotation work presented a unique opportunity to observe the dynamic physical changes (over a period of *ca.* 30 min) within the cell and their rapid variation upon activation. Related work in this field has only focused on longer term effects, such as the chemically induced differentiation of breast cancer cells over a period of days.[152]

Finally, following the work on the analysis of biosensor interfaces, a successful procedure has been developed for the analysis of enzyme content entrapped within biosensor films. The use of the three analytical techniques (amperometry, XPS and FTIR) provided comparable results - each demonstrating the non-linear relationship between enzyme concentration in solution and its concentration within the polymerised film. This technique has applications in other fields of biotechnology, for example, the characterisation of biomaterials for medical implantation.[219,220]

6.1 Recommendations for Future Work

Solving the problems of insulator adhesion would be of immense benefit in the future development of reliable biosensors. When successful, complex structures such as the Y-electrode fabricated for TWD will have the opportunity to be fully tested in aqueous solution. The most promising method of tackling this issue is the proposed use of a combination of first anisotropic dry etching to define the insulator pattern, followed by a brief isotropic wet etch to eliminate the possibility of etch residue deposition. If successful, this method would provide a clear way forward for the fabrication of a range of novel microelectrode structures.

The work on biosensor interfaces has demonstrated the application of parallel amperometric, XPS and FTIR techniques to the characterisation of biosensor interfaces. Whilst the fitting routines used were successful, it was felt that in future studies the quality of the XPS analysis could be further improved in a number of ways, including: (i) increasing counting times to reduce the noise level on the low level features of the poly(pyrrole) C(1s) and N(1s) spectra and (ii) by using non-linear baselines (e.g. Shirley baselines, to compensate for inelastic scattering effects). Further work is necessary to better characterise the distribution of the enzyme with respect to the *z*-axis (normal to the electrode surface) and to accurately determine the influence of adsorption effects. The accuracy of the FTIR study could be improved by developing a precise method to account for the non-linear background of the MCT detector. Any improvement in SNR can only aid the accuracy of the data analysis. Furthermore, future work on polymer matrices will require more precise data on film thickness, roughness and porosity.

6.2 Publications and Conference Contributions Arising from this Work

- Probing enzyme polymer biosensors using X-ray photoelectron spectroscopy: Determination of glucose oxidase in electropolymerised films. A. Griffith *et al*, Biosensors & Bioelectronics, Vol. 11, No. 6/7, 625-631, 1996.

- Two and three dimensional characterisation of the biomolecular composition of an enzyme-polymer biosensing electrode. A. Griffith *et al*, Journal of Physical Chemistry, submitted Sept. 1996.

- Characterisation of electron transfer reactions of redox peptides assembled at thiol monolayers on gold. L. Jiang *et al.*, Biosensors & Bioelectronics, submitted July 1996.

- An electrorotation study of activated human neutrophils. Biochimica et Biophysica Acta, in preparation.

- Immobilisation of microperoxidase (MP-11) through self-assembly at modified gold surfaces. Conference, American Vacuum Society, Minneapolis, Oct. 1995.

- The characterisation of biomolecular constructs at self-assembled monolayers using XPS, J. Cooper *et al*; p.27-29 The Research Unit for Surface Transforms and Interfaces Annual Report 1994-95.

- A microfabricated superoxide sensor. Conference, American Engineering Foundation: Nanofabrication and Biosystems - frontiers and challenges, Hawaii, May 1994.

- Nanostructures for bioelectronics and their application in cell signalling. Conference, Nanotechnology in medicine and the biosciencies, London, March 1993.

Appendix A

A1.1 Electrorotational Models

The electrical modelling of cells was initiated by Höber[221] and later enhanced by Fricke.[222] Concentrating on erythrocytes, a single shell model was developed that was used to deduce a value of 0.81μF cm^{-2} for the membrane capacitance and 3.3nm for membrane thickness. Subsequent papers have proposed alternatives such as the double shell[223] and smeared-out shell[224] models. These new models could explain the nature of the electrorotational spectra for a wider range of cell types. At high frequencies, it is easier for the electric field to penetrate into the non-homogeneous cellular interior and influence the recorded spectra.

A1.1.1 Neutrophils

The analysis of the electrorotational spectra the of neutrophils provide an opportunity to compare the double and single shell models defined by Asami *et al*[131].

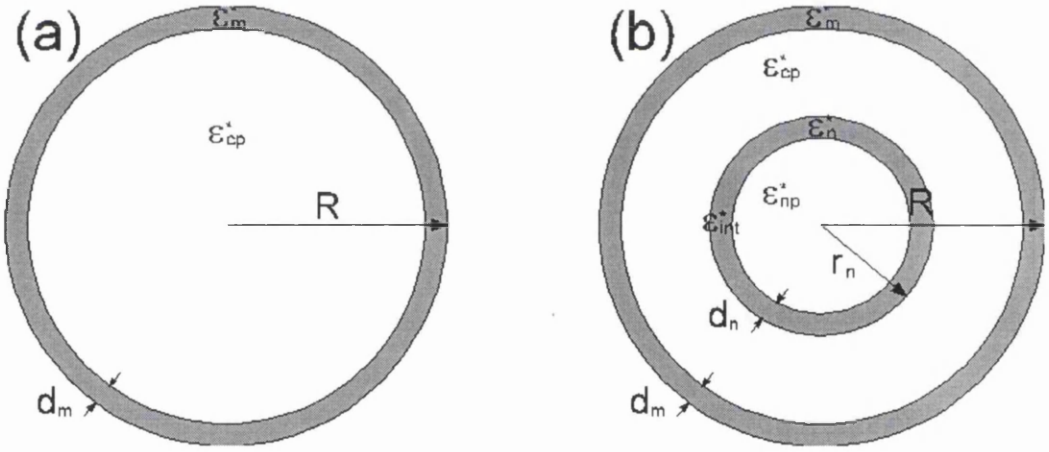

Figure A1 The components of the single (a) and double (b) shell models of a cell.

The analysis is based upon determining the effective complex permittivity of the whole cell (ε^*_c). From the double-shelled structure of figure A1, ε^*_c can be determined from:

$$\varepsilon^*_c = \varepsilon^*_m \frac{2(1-r_1)+(1+2r_1)\mathrm{E}_1}{(2+r_1)+(1-r_1)\mathrm{E}_1} \qquad (A.1)$$

with $r_1 = (1 - d_m/R)^3$, ε_m^* is the complex membrane permittivity, d_m is the membrane thickness, R is the cell radius and E_1 is an intermediate parameter, given by:

$$E_1 = \frac{\varepsilon_{cp}^*}{\varepsilon_m^*} \cdot \frac{2(1-r_2)+(1+2r_2)E_2}{(2+r_2)+(1-r_2)E_2} \tag{A.2}$$

with $r_2 = (r_n/(R - d_m)^3$. ε_{cp}^* is the complex permittivity of the cytoplasm and r_n is the radius of the nucleus. Similarly, the parameter E_2 is given by:

$$E_2 = \frac{\varepsilon_{np}^*}{\varepsilon_n^*} \cdot \frac{2(1-r_3)+(1+2r_3)E_3}{(2+r_3)+(1-r_3)E_3} \tag{A.3}$$

with $r_3 = (1 - d_n/r_n)^3$. ε_n^* and ε_{np}^* are the complex permittivities of the nuclear membrane and nuceoplasm, respectively; d_n is thickness of the nuclear membrane. Finally, the parameter E_3 is given by:

$$E_3 = \frac{\varepsilon_{np}^*}{\varepsilon_n^*} \tag{A.4}$$

Simulations using this model were made using a MATLAB (Mathworks Inc.) subroutine. The modelling output defined the frequency dependent variation of real and imaginary components of the Clausius-Mossotti factor. The single shell discussed above is a simpler version of the theory which does not take into consideration the possible influence of the cytoplasm contents.

A1.1.2 Polystyrene Beads

The theoretical analysis of the bead rotation has been described previously[37,126,127] and this section provides a summary of that work. In contrast to a cell, a polystyrene bead has a homogeneous solid interior, and the nature of electrorotation is dominated by the effects of its surface conductance (K_s), such that:

$$\sigma_p = \sigma_b + 2\frac{K_s}{r} \tag{A.5}$$

where σ_p and σ_b are the effective and bulk material conductivities of the polystyrene bead, and r is the bead radius. A previous analysis[37] has shown that K_s is about 1-2nS. Using a typical bead radius of 3μm and assuming a negligible polystyrene conductivity, the effective

conductivity of approximately 10μS cm^{-1}. Examination of equation A.5 provides a guide for the frequency dependent torque ($\Gamma(\omega)$) acting on the particle in a particular medium.

$$\Gamma(\omega) = -12\pi r^3 \omega \varepsilon_m \left[\frac{\varepsilon_p \sigma_m - \varepsilon_m \sigma_p}{(\sigma_p + 2\sigma_m) + \omega^2 (\varepsilon_p + 2\varepsilon_m)^2} \right] E^2 \qquad \text{(A.6)}$$

Where σ_m and ε_m are the medium conductivity and permittivity, with respective values of 500μS cm^{-1} and $79\varepsilon_0$. ε_p is the particle permittivity having an estimated value of $3.5\varepsilon_0$. Using the above estimate for σ_p and inserting these values into equation A.6, it is concluded that the beads will only exhibit co-field rotation since the numerator term ($\varepsilon_p \sigma_m - \varepsilon_m \sigma_p$) will always be negative for the experimental conditions used in this study.

Appendix B

B1.1 Determination of FTIR PPy/GOx Ratio

The Beer-Lamberts law[206] states that sample incident radiation:

$$E = E_i R_{Au} A \exp(-kAt\rho) \tag{B.1}$$

where E is the energy at the detector and E_i is the incident energy, R_{Au} is the reflectivity of the gold slide, k is the molar absorption coefficient (mol^{-1}), A and t are the sample areas and thickness respectively, and ρ is the number of moles of chromophores per unit volume. The similar subscript identification is used throughout this analysis, for example, A_r, A_{GOx}, A_{PPy} and A_{comp} represent the areas of the reference gold, PPy, GOx and composite sample slides respectively

Considering the energy of each component of the sample in turn:

$$E_{Au} = E_i R_{Au} A_{Au} \tag{B.2}$$

$$E_{GOx} = E_i R_{Au} A_{GOx} \exp(-k_{GOx} A_{GOx} t_{GOx} \rho_{GOx}) \tag{B.3}$$

$$E_{PPy} = E_i R_{Au} A_{PPy} \exp(-k_{PPy} A_{PPy} t_{PPy} \rho_{PPy}) \tag{B.4}$$

and assuming that PPy and GOx absorptions are non-interacting, which is valid if we are examining the amide I and II bands. The equation for the composite sample can be determined:

$$E_{comp} = E_i R_{Au} A_{comp} \exp(-k_{GOx} A_{comp} t_{comp} \rho_{GOx,comp}) \exp(-k_{PPy} A_{comp} t_{comp} \rho_{PPy,comp}) \tag{B.5}$$

We wish to find the value of the $\rho_{GOx,comp}/\rho_{PPy,comp}$ factor in order to determine the relative ratios of GOx and PPy in the composite samples.

By normalising the spectra at a wavenumber where no absorbances occur ($2000cm^{-1}$ in this study) the molar absorbance coefficient is the same for all samples. Then, by using logarithms, equations B.2, B.3 and B.4 can be combined using

$$a_{PPy} = A_{PPy}/A_{Au}, \; a_{GOx} = A_{GOx}/A_{Au}, \; a_{comp} = A_{comp}/A_{Au} \tag{B.6}$$

where a_{GOx}, a_{PPy}, and a_{comp} are the respective normalised absorbance values. The respective absorption responses can be equated as follows:

$$Ab_{GOx} = a_{GOx} - k_{GOx}a_{GOx}t_{GOx}\rho_{GOx} \quad \text{(B.7)}$$

$$Ab_{PPy} = a_{PPy} - k_{PPy}a_{PPy}t_{PPy}\rho_{PPy} \quad \text{(B.8)}$$

$$Ab_{comp} = a_{comp} - k_{GOx}a_{comp}A_{Au}t_{comp}\rho_{PPy,comp} - k_{PPy}a_{comp}A_{Au}t_{comp}\rho_{PPy,comp} \quad \text{(B.9)}$$

Analysis of the composite sample can be described as follows:

$$\alpha(Ab_{GOx} - a_{GOx}) + \beta(Ab_{PPy} - a_{PPy}) = (Ab_{comp} - a_{comp}) \quad \text{(B.10)}$$

where α and β represent the respective enzyme and polymer components of the composite sample.

Comparing equations B.7, B.8 and B.9 to B.10; the following equations for the α and β components are apparent:

$$\alpha(a_{GOx}A_{Au}t_{GOx}\rho_{GOx}) = a_{comp}A_{Au}t_{comp}\rho_{GOx,comp} \quad \text{(B.11)}$$

$$\beta(a_{PPy}A_{Au}t_{PPy}\rho_{PPy}) = a_{comp}A_{Au}t_{comp}\rho_{PPy,comp} \quad \text{(B.12)}$$

The determination of α and β directly is not possible due to the large number of unknowns, however, determination of the ratio α/β does provide information on the relative proportions of GOx and PPy in the films:

$$\alpha/\beta = \left[\frac{\rho_{GOx,comp}}{\rho_{PPy,comp}}\right]\left(\frac{a_{PPy}t_{PPy}\rho_{PPy}}{a_{GOx}t_{GOx}\rho_{GOx}}\right) \quad \text{(B.13)}$$

In equation B.13, the term in curved brackets is constant providing that the same reference GOx and PPy spectra are used. Hence, the α/β ratio represents a measure of the relative number of GOx *vs.* PPy chromophores in each composite sample.

References

(1) Lambrechts M.; Sansen W. "Biosensors: Microelectrochemical devices", Institute of Physics Publishing Ltd. New York, 1992.

(2) Wilkins E.; Atanasov P.; Muggenburg B. A. "Integrated implantable device for long-term glucose monitoring". *Biosensors & Bioelectronics* **1995,** *10,* 485-494.

(3) Strohben W. E.; Smith D. K.; Evans D. H. "Characterisation of arrays of microelectrodes for fast voltammetry". *Anal. Chem.* **1990,** *62,* 1709-1712.

(4) Kovacs G. T. A.; Peterson K.; Albin M. "Silicon micromachining: sensors to systems". *Anal. Chem.* **1996,** *68,* 13, 407A-412A.

(5) Gopel W. "Controlled signal-transduction across interfaces of intelligent molecular-systems". *Biosensors & Bioelectronics* **1995,** *10,* 35-59.

(6) Arquint P.; Koudelkahep M.; Derooij N. F.; Buhler H.; Morf W. E. "Organic membranes for miniaturized electrochemical sensors - fabrication of a combined p[O_2], p[CO_2] and pH sensor". *J. Electroanal. Chem.* **1994,** *378,* 177-183.

(7) Rojas E.; Stokes C. L.; Mears D.; Atwater I. "Single-microelectrode voltage-clamp measurements of pancreatic beta-cell membrane ionic currents in-situ". *J. Membrane Biol.* **1995,** *143,* 65-77.

(8) Collinson M.; Bowden E. F.; Tarlov M. J. "Voltammetry of covalently immobilized cytochrome-c on self-assembled monolayer electrodes". *Langmuir* **1992,** *8,* 1247-1250.

(9) Schuhmann W. "Electron-transfer pathways in amperometric biosensors -ferrocene-modified enzymes entrapped in conducting-polymer layers". *Biosensors & Bioelectronics* **1995,** *10,* 181-193.

(10) Koopal C. G. J.; Bos A. A. C. M.; Nolte R. J. M. "Third-generation glucose biosensor incorporated in a conducting printing ink". *Sensors and Actuators B.* **1994,** *18,* 166-170.

(11) Ballarin B.; Brumlik C. J.; Lawson D. R.; Liang W. B.; Vandyke L. S.; Martin C. R. "Chemical sensors based on ultrathin-film composite membranes - a new concept in sensor design". *Anal. Chem.* **1992,** *64,* 2647-2651.

(12) Hall E. A. H. "Biosensors", Open University Press: Milton Keynes, UK, 1990.

(13) Klebanoff S. F. "Iodation of Bacteria. A bactericidal mechanism.". *J. Exp. Med.* **1967,** *126,* 1063-1029.

(14) Lunec J. "Free radicals: Their involvement in disease processes". *Ann. Clin. Biochem.* **1990,** *27,* 173-182.

(15) Maly F. E. "The B lymphocyte: A newly recognized source of reactive oxygen species with immunoregulatory potential". *Free Rad. Res. Comms.* **1989,** *8-3,* 143-148.

(16) Saran M.; Bors W. "Oxygen radicals acting as chemical messengers - a hypothesis". *Free Rad. Res. Comms.* **1989,** *7,* 213, 220

(17) Hamilton T. A.; Adams D. O. "Molecular mechanisms of signal transduction in macrophages". *Immun. Today* **1994,** *8,* 151-158.

(18) Takashashi R.; Edashige K.; Sato E. F.; Inoue M.; Matsuno T.; Utsumi K. "Luminol chemiluminescence and active oxygen generation by activated neutrophils". *Arch. Biochem. Biophys.* **1991,** *285,* 2, 325-330.

(19) Sigma Diagnostics "Nitroblue Tetrazolium (NBT) Reduction - Histochemical demonstration in neutrophils. Procedure No. 840", **1990.**

(20) Sanders S. P.; Sylvester J. T.; Harrison S. J.; Zweier J. L. "Comparison of the sensitivity of free-radical measurement by EPR spin trapping and cytochrome-c reduction techniques". *Faseb J.* **1993,** *7,* 657

(21) Sekiguchi T.; Nagamine T. "Inhibition of free radical generation by biotin". *Biochem. Pharmacol.* **1994,** *47,* 594-596.

(22) McNeil C. J.; Smith K. A.; Bellavite P.; Bannister J. V. "Application of the electrochemistry of cytochrome c to the measurement of superoxide radical production". *Free Rad. Res. Comms.* **1989,** *7,* 89-96.

(23) Clark L. C.; Lyons C. L. "Electrode systems for continious monitoring in cardiovascular surgery". *Ann. NY. Acad. Sci.* **1962,** *102,* 29

(24) Foulds N. C.; Lowe C. R. "Immobilisation of glucose oxidase in ferrocene-modified pyrrole polymers". *Anal. Chem.* **1988,** *60,* 2473-2478.

(25) Keilin D.; Hartree E. F. "The use of glucose oxidase (notatin) for the determination of glucose in biological material and for the study of glucose-producing systems by manometric methods". *Biochem. J.* **1948,** *42,* 221-231.

(26) Bartlett P. N.; Tebbutt P.; Tyrrell C. H. "Electrochemical immobilization of enzymes .3. Immobilization of glucose oxidase in thin films of electrochemically polymerized phenols". *Anal. Chem.* **1992,** *64,* 138-142.

(27) Bartlett P. N.; Ali Z.; Eastwickfield V. "Electrochemical immobilization of enzymes .4. Co-immobilization of glucose oxidase and ferro-ferricyanide in poly(normal-methylpyrrole) films". *J. Chem. Soc. , Faraday Trans. 1* **1992,** *88,* 2677-2683.

(28) Higgins S. J.; Hamnett A. "In-situ ellipsometric study of the growth and electrochemical cycling of polypyrrole films on platinum". *Electrochimica Acta* **1991,** *36,* 2123-2134.

(29) Daniels P. B.; Deacon J. K.; Eddowes M. J.; Pedley D. G. "Surface-plasmon resonance applied to immunosensing". *Sensors and Actuators A.* **1988,** *15,* 11-18.

(30) Schneider T. W.; Buttry D. A. "Electrochemical quartz crystal microbalance studies of adsorption and desorption of self-assembled monolayers of alkyl thiols on gold". *J. Am. Chem. Soc.* **1993,** *115,* 12391-12397.

(31) Wang J. H.; Ruddock L. W.; Cass A. E. G. "Microscopic investigations of the interaction of proteins with surfaces". *Biosensors & Bioelectronics* **1994,** *9,* 647-655.

(32) Huang Y.; Wang X.; Tame J. A.; Pethig R. "Electrokinetic behavior of colloidal particles in travelling electric fields: studies using yeast cells". *J. Phys. D: Appl. Phys.* **1993,** *26,* 1528-1535.

(33) Becker F. F.; Wang X. B.; Huang Y.; Pethig R.; Vykoukal J.; Gascoyne P. R. C. "The removal of human leukemia cells from blood using interdigitated microelectrodes". *J. Phys. D: Appl. Phys.* **1994,** *27,* 2659-2662.

(34) Dimitrov D. S.; Zhelev D. V. "Dielectrophoresis of individual cells experimental methods and results". *Bioelectrochem. Bioenerg.* **1987,** *17,* 549-557.

(35) Gascoyne P. R. C.; Pethig R.; Burt J. P. H.; Becker F. F. "Membrane changes accompanying the induced differentiation of Friend murine erythroleukemia cells studied by dielectrophoresis". *Biochim. Biophys. Acta* **1993,** *1149,* 119-126.

(36) Fuhr G.; Voigt A.; Muller T.; Wagner B.; Reimer K.; Lisec T. "Electric-field-mediated inhibition of cell and microparticle adhesion: a new way to create bio-repellent surfaces". *Sensors and Actuators B.* **1995,** *27,* 468-470.

(37) Zhou X. F.; Markx G. H.; Pethig R.; Eastwood I. M. "Differentiation of viable and non-viable bacterial biofilms using electrorotation". *Biochim. Biophys. Acta* **1995,** *1245,* 85-93.

(38) Pohl H. A. "The motion and precipitation of suspensions in divergent electric fields". *J.Appl.Phys.* **1951,** *22,* 869-871.

(39) Fuhr G.; Arnold W. M.; Hagedorn R.; Muller T.; Benecke W.; Wagner B.; Zimmermann U. "Levitation, holding, and rotation of cells within traps made by high-frequency fields". *Biochim. Biophys. Acta* **1992,** *1108,* 215-223.

(40) Huang Y.; Holzel R.; Pethig R.; Wang X. B. "Differences in the AC electrodynamics of viable and non-viable yeast cells determined through combined dielectrophoresis and electrorotation studies". *Phys. Med. Biol.* **1992,** *37,* 7, 1499-1517.

(41) Arnold W. M.; Schmutzler R. K.; Alhasani S.; Krebs D.; Zimmermann U. "Differences in membrane properties between unfertilized and fertilized single rabbit oocytes demonstrated by electro-rotation. Comparison with cells from early embryos". *Biochim. Biophys. Acta* **1989,** *979,* 142-146.

(42) Anderson R. "The activated neutrophil - formidable forces unleashed". *South African Medical Journal* **1995,** *85,* 1024-1028.

(43) Maly F. E.; Schurermaly C. C. "How and why cells make superoxide: The "phagocytic" NADPH oxidase". *News In Physiological Sciences* **1995,** *10,* 233-238.

(44) Morel F.; Doussiere J.; Vignais P. V. "The superoxide-generating oxidase of phagocytic cells - physiological, molecular and pathological aspects". *Eur. J. Biochem.* **1991,** *201,* 523-546.

(45) Hill H. A. O.; Tew D. G.; Walton N. J. "An opsonised microelectrode - Observation of the respiratory burst of a single human neutrophil". *FEBS Lett.* **1985,** *191,* 257-263.

(46) Yoshaiki M. "The mechanism of overhang formation in diazide/novolak photoresist film by chlorobenzene soak process". *J. Vac. Sci. Technol. B* **1986,** *4,* 1, 15-21.

(47) Makogon Y. N.; Sidorenko S. I.; Bazarnyi Y. A.; Voltovets N. S.; Litvinova T. V.; Tkachenko V. L. "Diffusion in thin-films of Au/Pd/Ti and Au/Pd/Cr/Ti on silicon". *Inorganic Materials* **1990,** *26,* 2116-2121.

(48) Munitz A.; Komem Y. "Structural and resistivity changes in heat-treated chromium-gold films". *Thin Solid Films* **1995,** *20,* 171-179.

(49) Vogt K. W.; Kohl P. A.; Carter W. B.; Bell R. A.; Bottomley L. A. "Characterization of thin titanium oxide adhesion layers on gold - resistivity, morphology, and composition". *Surface Science* **1994,** *301,* 203-213.

(50) Creager S. E.; Hockett L. A.; Rowe G. K. "Consequences of microscopic surface roughness for molecular self-assembly". *Langmuir* **1992,** *8,* 854-861.

(51) Sharp D. J. "Corrosion inhibition in sputter-deposited thin-film systems using an intermediary layer of palladium". *J. Vac. Sci. Technol.* **1979,** *16:2,* 204-207.

(52) Goss C. A.; Charych D. H.; Majda M. "Application of (3-Mercaptopropyl)trimethoxysilane as a molecular adhesive in the fabrication of vapor-deposited gold electrodes on glass substrates". *Anal. Chem.* **1991,** *63,* 85-88.

(53) Prasad K.; Perfecto E. "Multilevel thin-film packaging: Applications and processes for high performance systems". *IEEE Trans.Comp.Packag.Man.Tech.Part B-Adv.Packag.* **1994,** *17,* 38-49.

(54) Schammler G. k. h.; Glaw V.; Chimel G. "Comparison of the metallisation of chemically ans laser-etched structures in BPDA-PDA polyimide". *IEEE Trans.Comp., Hybrids, Manuf.Technol.* **1993,** *16,* 7, 720-723.

(55) Isobe A.; Shinohara M.; Hiraki M.; Hoshino A. "Via hole failure study". *NEC Res. & Develop.* **1993,** *34,* 1, 77-83.

(56) Reimer K.; Kohler C.; Lisec T.; Schnakenberg U.; Fuhr G.; Hintsche R.; Wagner B. "Fabrication of electrode arrays in the quarter micron regime for biotechnological applications". *Sensors and Actuators A.* **1995,** *46,* 66-70.

(57) Shih D. Y.; Yeh H. L.; Paraszczak J.; Lewis J.; Graham W.; Nunes S.; Narayan C.; Mcgouey R.; Galligan E.; Cataldo J., et al. "Factors affecting the interconnection resistance and yield in multilayer polyimide copper structures". *IEEE Trans.Comp., Hybrids, Manuf.Technol.* **1993,** *16,* 74-88.

(58) White G.; Perfecto E.; Mcherron D.; Demercurio T.; Redmond T.; Norcott M. "Large-format fabrication - a practical approach to low-cost MCM-D". *IEEE Trans.Comp.Packag.Man.Tech.Part B-Adv.Packag.* **1995,** *18,* 37-41.

(59) Hicks S. "For reduced stress metal films use a Ni/Ti multilayer film. This procedure has been proven during a collaborative research project with engineers at the British Telecom research labs in Ipswich, UK",.*Personal Communication,* **1995**.

(60) Breckenridge L. J.; Wilson R. J. A.; Connnolly P.; Curtis A. S. G.; Dow J. A. T.; Blacksaw S. E.; Wilkinson C. D. W. "Advantages of using microfabricated extracellular electrodes for in vitro neuronal recording". *J. Neurosci. Research* **1995,** *42,* 266-276.

(61) Bard S. L.; Feger C.; Glenning J. J.; Hougham G. G.; Molis S. E.; Pawlowski W. P.; Ritsko J. J.; Slota P.; Snyder R. W. IBM Corporation, A., N.Y. assignee. "Wet etching of thermally or chemically cured polyimide", New York/USA. 4846929. **1989,** *218384,*

(62) Pang S. W.; Sung K. T.; Ko K. K. "Etching of photoresist using oxygen plasma generated by a multipolar electron-cyclotron resonance source". *J. Vac. Sci. Technol. B* **1992,** *10,* 1118-1123.

(63) Wu S. Y.; Desouzamachado R.; Denton D. D. "Dielectric and chemical modifications in polyimide films etched in O_2/CF_4 plasmas". *J.Vac.Sci.Technol.A* **1993,** *11,* 1337-1345.

(64) Egitto F. D.; Matienzo L. J.; Blackwell K. J.; Knoll A. R. "Oxygen plasma modification of polyimide webs - effect of ion-bombardment on metal adhesion". *J.Adhesion Sci.Technol.* **1994,** *8,* 411-433.

(65) Shimoto T.; Matsui K.; Utsumi K. "Cu photosensitive-BCB thin-film multilayer technology for high-performance multichip modules". *IEEE Trans.Comp.Packag.Man.Tech.Part B-Adv.Packag.* **1995,** *18,* 18-22.

(66) Joubert O.; Pelletier J.; Fiori C.; Nguyen Tan T. A. "Surface mechanisms in O_2 and SF_6 microwave plasma etching of polymers". *J.Appl.Phys.* **1990,** *67,* 9,.4291-4296.

(67) Suzuki H.; Sekine H.; Koibuchi S.; Sato H.; Makino D. "Patterning of fine via holes in polyimide by an oxygen reactive ion etching". *ACS Symposium Series* **1987,** 547-556.

(68) Shih D. Y.; Klymko N.; Flitsch R.; Paraszczak J.; Nunes S. "Oxygen induced adhesion degradation at metal polyimide interface". *J.Vac.Sci.Technol.A* **1991,** *9,* 2963-2974.

(69) Xue G.; Wang Y. X.; Chen Y. U.; Tsai S. S.; Jiang L. H. "Adhesion promotion at high-temperature for epoxy-resin or polyimide onto metal by a 2-component coupling system of polybenzimidazole and 4-aminophenyl disulfide". *J.Appl.Polym.Sci.* **1995,** *58,* 2221-2227.

(70) Cloud T. A.; Houston M. R.; Kohl P. A.; Bidstrup S. A. "Processing and performance of gold MCM's". *IEEE Trans.Comp., Hybrids, Manuf.Technol.* **1993,** *16,* 724-730.

(71) Osada K.; Zaitsu Y.; Matsumoto S.; Yoshida M.; Arai E.; Abe T. "Effect of stress in the deposited silicon-nitride films on boron-diffusion of silicon". *J.Electrochem.Soc.* **1995,** *142,* 202-206.

(72) Alexandrov S. E.; Hitchman M. L.; Shamlian S. H. "Remote plasma-enhanced vapour deposition of silicon nitride films: The effect of diluting nitrogen with helium". *J. Mater. Chem.* **1995,** *5,* 3, 457-460.

(73) Kissinger P. T.; Heineman W. R. "Laboratory techniques in electroanalytical chemistry", Marcel Dekker Inc. New York, 1984.

(74) Bard A. J.; Faulkner L. R. "Electrochemical methods - fundamentals and application", John Wiley & Sons: New York, 1980.

(75) Abdelhamid I.; Atanasov P.; Wilkins E. "Needle-type glucose biosensor with an electrochemically codeposited enzyme in a platinum black matrix". *Electroanalysis* **1995,** *7,* 738-741.

(76) Frew J. E.; Foulds N. C.; Wilshere J. M.; Forrow N. J.; Green M. J. "Measurement of alkaline phosphatase activity by electrochemical detection of phosphate esters". *J. Electroanal. Chem.* **1989,** *266,* 309-316.

(77) Van Benschoten J. J.; Lewis J. Y.; Heineman W. R.; Roston D. A.; Kissinger P. T. "Cyclic voltammetry experiment". *J. Chem. Educ.* **1983,** *60,* 772-776.

(78) Kissinger P. T.; Heineman W. R. "Cyclic voltammetry". *J. Chem. Educ.* **1983,** *60,* 702-706.

(79) Cooper J. M.; Greenough K. R.; McNeil C. J. "Direct electron transfer reactions between immobilized cytochrome c and modified gold electrodes". *J. Electroanal. Chem.* **1993,** *347,* 267-275.

(80) Nicholson R. S. "Theory and application of cyclic voltammetry for measurement of electrode reaction kinetics". *Anal. Chem.* **1965,** *37,* 1351-1355.

(81) Beriet C.; Pletcher D. "A microelectrode study of the mechanism and kinetics of the ferro/ferricyanide couple in aqueous-media: the influence of the electrolyte and its concentration". *J. Electroanal. Chem.* **1993,** *361,* 93-101.

(82) Wightman R. M. "Microvoltammetric electrodes". *Anal. Chem.* **1981,** *9,* 1125A-1134A.

(83) Wightman R. M.; Wipf D. O. "Voltammetry at ultramicroelectrodes". *Electroanalytical Chemistry* **1989,** *15,* 267-353.

(84) Pons S.; Fleischmann M. "The behavior of microelectrodes". *Anal. Chem.* **1987,** *59,*

(85) Heinze J. "Ultramicroelectrodes in electrochemistry". *Angew. Chem. Int. Ed. Engl.* **1993,** *32,* 1268-1288.

(86) Mastrototaro J. J.; Massoud H. Z.; Pilkington T. C.; Ideker R. E. "Rigid and flexible thin-film multielectrode arrays for transmural cardiac recording". *IEEE Trans.Biomed.Eng.* **1992,** *39,* 271-279.

(87) Zhao G.; Giolando D. M.; Kirchhoff J. R. "Fabrication of silica-coated carbon-fiber ultramicroelectrodes by chemical-vapor-deposition". *J. Electroanal. Chem.* **1994,** *379,* 505-508.

(88) Wrighton M. S.; Thackery J. W.; Natan M. J.; Smith D. K.; Lane G. A.; Belanger D. "Modification of microelectrode arrays: new microelectrochemical devices for sensor applications". *Phil. Trans. R. Soc. Lond. B* **1987,** *316,* 13-30.

(89) Paeschke M.; Wollenberger U.; Kohler C.; Lisec T.; Schnakenberg U.; Hintsche R. "Properties of interdigitated electrode arrays with different geometries". *Anal. Chim. Acta.* **1995,** *305,* 126-136.

(90) Shea T. V.; Bard A. J. "Digital simulation of homogeneous chemical reactions coupled to heterogeneous electron transfer and applications at platinum/mica/platinum microelectrodes". *Anal. Chem.* **1987,** *59,* 2101-2111.

(91) Aoki K.; Morita M.; Niwa O.; Tabei H. "Quantitative-analysis of reversible diffusion-controlled currents of redox soluble species at interdigitated array electrodes under steady-state conditions". *J. Electroanal. Chem.* **1988,** *256,* 269-282.

(92) Moressi M. B.; Fernandez H. "The use of ultramicroelectrodes for the determination of diffusion-coefficients". *J. Electroanal. Chem.* **1994,** *369,* 153-159.

(93) Aoki K. "Theory of ultramicroelectrodes". *Electroanalysis* **1993,** *5,* 627-639.

(94) BIOCHEMIST'S HANDBOOK "CHEMICAL DATA: Preparation of constant ionic strength buffers", [Unpublished] **1994.**

(95) McNeil C. J.; Greenough K. R.; Weeks P. A.; Self C. H.; Cooper J. M. "Electrochemical sensors for direct reagentless measurement of superoxide production by human neutrophils". *Free Rad. Res. Comms.* **1992,** *17,* 399-406.

(96) Manning P. "1st Year PhD report: Superoxide detection in biological systems", Newcastle upon Tyne, *Unpublished,* **1995.**

(97) Goldstein E. L.; VanDeMark M. R. "Electrode cleaning and anion effects on ks for K3Fe(CN)6 couple". *Bioelectrochimica Acta* **1982,** *27,* 1079-1085.

(98) Chialvo A. C.; Triaca W. E.; Arvia A. J. "Changes in the polycrystalline gold electrode surface produced by square wave potential perturbations". *J. Electroanal. Chem.* **1984,** *171,* 303-316.

(99) Weisshaar D. E.; Walczak M. M.; Porter M. D. "Electrochemically induced transformations of monolayers formed by self-assembly of mercaptoethanol at gold". *Langmuir* **1993,** *9,* 323-329.

(100) Bard A. J.; Crayston J. A.; Kittlesen G. P.; Shea T. V.; Wrigthton M. S. "Digital simulation of the measured electrochemical response of reversible redox couples at microelectrode arrays: consequences arising from closely spaced ultramicroelectrodes". *Anal. Chem.* **1986,** *58,* 2321-2331.

(101) Cha C. S.; Chen J.; Liu P. F. "Improvement of the adhesion of a Nafion(r) modifying layer on electrodes". *J. Electroanal. Chem.* **1993,** *345,* 463-467.

(102) Oesch U.; Janata J. "Electrochemical study of gold electrodes with anodic films - I. Formation and reduction behavior of anodic oxides on gold". *Electrochimica Acta* **1983,** *28,* 9, 1237-1246.

(103) Eddowes M. J.; Hill H. A. O. "Electrochemistry of horse heart cytochrome c". *J. Am. Chem. Soc.* **1979,** *101,* 16, 4461-4464.

(104) Willit J. L.; Bowden E. F. "Adsorption and redox thermodynamics of strongly adsorbed cytochrome c on tin oxide electrodes". *J. Phys. Chem.* **1990,** *94,* 8241-8246.

(105) Daido T.; Akaike T. "Electrochemistry of cytochrome c: Influence of coulombic attraction with indium tin oxide electrode". *J. Electroanal. Chem.* **1993,** *344,* 91-106.

(106) Reed D. E.; Hawkridge F. M. "Direct electron transfer reactions of cytochrome c at silver electrodes". *Anal. Chem.* **1987,** *59,* 2334-2339.

(107) Digleria K.; Hill H. A. O.; Lowe V. J.; Page D. J. "Direct electrochemistry of horse-heart cytochrome c at amino acid-modified gold electrodes". *J. Electroanal. Chem.* **1986,** *213,* 333-338.

(108) Allen P. M.; Hill H. A. O.; Walton N. J. "Surface modifiers for the promotion of direct electrochemistry of cytochrome c". *J. Electroanal. Chem.* **1984,** *178,* 69-86.

(109) Santucci R.; Faraoni A.; Campanella L.; Tranchida G.; Brunori M. "Use of solid-state promoters in the electrochemistry of cytochrome-c at a gold electrode". *Biochem. J.* **1991,** *273,* 783-786.

(110) Santucci R.; Brunori M.; Campanella L.; Tranchida G. "Electrochemical behavior of horse heart cytochrome c and microperoxidase at a gold electrode chemically modified with sulphur-containing compounds". *Bioelectrochem. Bioenerg.* **1992,** *29,* 177-184.

(111) Song S.; Clark R. A.; Bowden E. F.; Tarlov M. J. "Characterization of cytochrome-c alkanethiolate structures prepared by self-assembly on gold". *J. Phys. Chem.* **1993,** *97,* 6564-6572.

(112) Lotzbeyer T.; Schuhmann W.; Katz E.; Falter J.; Schmidt H. "Direct electron transfer between the covalently immobilized enzyme microperoxidase MP-11 and a cystamine-modified gold electrode". *J. Electroanal. Chem.* **1994,** *377,* 291-294.

(113) Weisshaar D. E.; Lamp B. D.; Porter M. D. "Thermodynamically controlled electrochemical formation of thiolate monolayers at gold: characterization and comparison to self-assembled analogs". *J. Am. Chem. Soc.* **1992,** *114,* 5860-5862.

(114) Kim E.; Kumar A.; Whitesides G. M. "Combining patterned self-assembled monolayers of alkanethiolates on gold with anisotropic etching of silicon to generate controlled surface morphologies". *J.Electrochem.Soc.* **1995,** *142,* 628-633.

(115) McLendon G. "Similar observation of thiol electrochemistry at low positive potentials (.3V)". *Personal Communication,* **1996.**

(116) Rongen H. A. H.; Hoetelmans R. M. W.; Bult A.; Vanbennekom W. P. "Chemiluminescence and immunoassays". *Journal Of Pharmaceutical And Biomedical Analysis* **1994,** *12,* 433-462.

(117) Daval J. L.; Ghersiegea J. F.; Oillet J.; Koziel V. "A simple method for evaluation of superoxide radical production in neural cells under various culture conditions - application to hypoxia". *J. Cereb. Blood Flow Metab.* **1995,** *15,* 71-77.

(118) Babior B. M.; Kipnes R. S.; Curnutte J. T. "Biological Defense Mechanisms: The production of leukocytes of superoxide - a potential bactericidal agent". *J. Clin. Invest.* **1973,** *52,* 741-744.

(119) Tauber A. I. "Protein kinase C and the activation of the human neutrophil NADPH-oxidase". *Blood* **1987,** *69,* 3, 711-720.

(120) Nathan C. F. "Neutrophil activation on biological surfaces - massive secretion of hydrogen peroxide in response to products of macrophages and lymphocytes". *J. Clin. Invest.* **1987,** *80,* 1550-1560.

(121) Turgiev A.; Kubatiev A. "Rabbit-blood neutrophils are more responsive to aggregation inducers and inhibitors than their human counterparts". *Int.J.Immunotherapy* **1990,** *6,* 119-129.

(122) Fleischmann M.; Pons S. "The behaviour of microdisk and microring electrodes". *J. Electroanal. Chem.* **1987,** *222,* 107-115.

(123) Green M. J.; Hill H. A. O.; Tew D. G.; Walton N. J. "An opsonised electrode: The direct electrochemical detection of superoxide generated by human neutrophils". *FEBS Lett.* **1984,** *170,* 69-72.

(124) Bratten C. D. T.; Cobbold P.H.; Cooper J.M. "Micromachinig sensors for electrochemicakl measurement in sub-nanolitre volumes". *In Preparation,* **1996.**

(125) Pethig R.; Huang Y.; Wang X. B.; Burt J. P. "Positive and negative dielectrophoretic collection of colloidal particles using interdigitated castellated microelectrodes". *J. Phys. D: Appl. Phys.* **1992,** *25,* 881-888.

(126) Foster K. R.; Sauer F. A.; Schwan H. P. "Electrorotation and levitation of cells and colloidal particles". *Biophys. J.* **1992,** *63,* 180-190.

(127) Arnold W. M.; Schwan H. P.; Zimmermann U. "Surface conductance and other properties of latex particles measured by electrorotation". *J. Phys. Chem.* **1987,** *91,* 5093-5098.

(128) Pethig R. "Dielectric properties of biological materials", Wiley: Chichester, UK, 1979.

(129) Wang X. B.; Huang Y.; Gascoyne P. R. C.; Becker F. F.; Holzel R.; Pethig R. "Changes in friend murine erythroleukemia cell membranes during induced differentiation determined by electrorotation". *Biochim. Biophys. Acta* **1994,** *1193,* 330-344.

(130) Ziervogel H.; Glaser R.; Schadow D.; Heymann S. "Electrorotation of lymphocytes - the influence of membrane events and nucleus". *Biosci. Rep.* **1986,** *6,* 973-982.

(131) Asami K.; Takahashi Y.; Takashima S. "Dielectric properties of mouse lymphocytes and erythrocytes". *Biochim. Biophys. Acta* **1989,** *1010,* 49-55.

(132) Schwan H. P. "Physical techniques in biological research", Academic Press: New York, 1966.

(133) Sato N.; Kashima K.; Shimizu H.; Uehara Y.; Shimomura Y.; Mori M. "Hypertonic glucose inhibits the production of oxygen-derived free radicals by rat neutrophils". *Life Sci.* **1993,** *52,* 1481-1486.

(134) O'Flaherty J. T.; Dechatlet L. R.; McCall C. E.; Bass D. A. "Neutrophil aggregation: Evidence for a different mechanism of action by Phorbol Myristate Acetate (40962)". *Proc.Soc.Exp.Biol.Med.* **1980,** *165,* 225-232.

(135) Huang Y.; Pethig R. "Electrode design for negative dielectrophoresis". *Meas. Sci. Technol.* **1991,** *2,* 1142-1146.

(136) Hughes M. P.; Wang X. B.; Becker F. F.; Gascoyne P. R. C.; Pethig R. "Computer-aided analyses of electric-fields used in electrorotation studies". *J. Phys. D: Appl. Phys.* **1994,** *27,* 1564-1570.

(137) Chettibi S.; Lawrence A. J.; Stevenson R. D.; Young J. D. "Effect of lysophosphatidic acid on motility, polarization and metabolic burst of human neutrophils". *FEMS Immunology And Medical Microbiology* **1994,** *8,* 271-281.

(138) Lippi U.; Bellavite P.; Schinella M.; Nicoli M.; Lippi G. "Assessment of neutrophil aggregation by coulter(r) STKR and STKS hematological analyzers". *Clin. Lab. Haemat.* **1994,** *16,* 43-55.

(139) Sigma Diagnostics "Trypan blue procedure", **1996.**

(140) Lundqvist H.; Kricka L. J.; Stott R. A.; Thorpe G. H. G.; Dahlgren C. "Influence of different luminols on the characteristics of the chemiluminescence reaction in human neutrophils". *J.Biolumin.Chemilumin.* **1995,** *10,* 353-359.

(141) Arnold W. M.; Gessner A. G.; Zimmermann U. "Dielectric measurements on electro-manipulation media". *Biochim. Biophys. Acta* **1993,** *1157,* 32-44.

(142) Gimsa J.; Schnelle T.; Zechel G.; Glaser R. "Dielectric spectroscopy of human erythrocytes: Investigations under the influence of nystatin". *Biophys. J.* **1994,** *66,* 1244-1253.

(143) Davis B. H.; Walter R. J.; Pearson C. B.; Becker E. L.; Oliver J. M. "Membrane activity and topography of F-Met-Leu-Phe-treated polymorphonuclear leukocytes -acute and sustained responses to chemotactic peptide". *Am. J. Pathol.* **1982,** *108,* 206-216.

(144) Fuhr G.; Schnelle T.; Hagedorn R.; Shirley S. G. "Dielectrophoretic field cages: technique for cell, virus and macromolecule handling". *Cellular Engineering* **1995,** *1,* 47-57.

(145) Muller T.; Gerardino A.; Schnelle T.; Shirley S. G.; Bordoni F.; Degasperis G.; Leoni R.; Fuhr G. "Trapping of micrometer and submicrometer particles by high-frequency electric-fields and hydrodynamic-forces". *J. Phys. D: Appl. Phys.* **1996,** *29,* 340-349.

(146) Fuhr G.; Glasser H.; Muller T.; Schnelle T. "Cell manipulation and cultivation under A.C. electric field influence in highly conductive culture media". *Biochim. Biophys. Acta* **1994,** *1201,* 353-360.

(147) Hu X.; Arnold W. M.; Zimmermann U. "Alterations in the electrical properties of T and B lymphocyte membranes induced by mitogenic stimulation. Activation monitored by electro-rotation of single cells". *Biochim. Biophys. Acta* **1990,** *1021,* 191-200.

(148) Grinstein S.; Furuya W.; Cragoe E. J. "Volume changes in activated human-neutrophils: The role of Na^+/H^+ exchange". *J. Cell. Physiol.* **1986,** *128,* 33-40.

(149) Watts R. G.; Crispens M. A.; Howard T. H. "A quantitative study of the role of f-actin in producing neutrophil shape". *Cell Motil.* **1991,** *19,* 159-168.

(150) Coates T. D.; Watts R. G.; Hartman R.; Howard T. H. "Relationship of F-actin distribution to development of polar shape in human polymorphonuclear neutrophils". *J. Cell Biol.* **1992,** *117,* 765-774.

(151) Sukhorukov V. L.; Arnold W. M.; Zimmermann U. "Hypotonically induced changes in the plasma membrane of cultured mammalian cells". *J. Membrane Biol.* **1993,** *132,* 27-40.

(152) Becker F. F.; Wang X.; Huang Y.; Pethig R.; Vykoukal J.; Gascoyne P. R. C. "Separation of human breast cancer cells from blood by differential dielectric affinity". *Proc.Natl.Acad.Sci.USA* **1995,** *92,* 860-864.

(153) Masuda S.; Washizu M.; Kawabata I. "Movement of blood cells in liquid by nonuniform traveling field". *IEEE Trans. Ind. Appl.* **1988,** *24:2,* 217-222.

(154) Hagedorn R.; Fuhr G.; Muller T.; Gimsa J. "Traveling-wave dielectrophoresis of microparticles". *Electrophoresis* **1992,** *13,* 49-54.

(155) Wang X. B.; Huang Y.; Hughes M. P.; Pethig R.; Gascoyne P. R. C.; Becker F. F. "Separation of biological cells using traveling electric-fields". *Biophys. J.* **1994,** *66,* 281

(156) Hughes M. P.; Pethig R.; Wang X. B. "Dielectrophoretic forces on particles in traveling electric-fields". *J. Phys. D: Appl. Phys.* **1996,** *29,* 474-482.

(157) Chandler G. K.; Pletcher D. "The electrochemistry of conducting polymers". *Electrochemistry* **1985,** *10,* 117-124.

(158) Qian R.; Qiu J. "Electrochemically prepared polypyrroles from aqueous solution". *Polymer J.* **1987,** *19,* 157-172.

(159) Diaz A. F.; Kanazawa K. K.; Gardini G. P. "Electrochemical polymerisation of pyrrole". *J. Chem. Soc., Chem. Commun.* **1979,** 635

(160) Foulds N. C.; Lowe C. R. "Enzyme entrapment in electrically conducting polymers". *J. Chem. Soc., Faraday Trans. 1* **1986,** *82,* 1259-1264.

(161) Ammon H. P. T.; Ege W.; Oppermann M.; Gopel W.; Eisele S. "Improvement in the long-term stability of an amperometric glucose sensor system by introducing a cellulose membrane of bacterial origin". *Anal. Chem.* **1995,** *67,* 466-471.

(162) Fortier G.; Belanger D. "Characterization of the biochemical behavior of glucose oxidase entrapped in a polypyrrole film". *Biotechnol.Bioeng.* **1991,** *37,* 854-858.

(163) Chen C. C.; Bose C. S.; Rajeshwar K. "The reduction of dioxygen and the oxidation of hydrogen at polypyrrole film electrodes containing nanodispersed platinum particles". *J. Electroanal. Chem.* **1993,** *350,* 161-176.

(164) Scharifker B. R.; Fermin D. J. "The role of intermediates in solution in the initial-stages of electrodeposition of polypyrrole". *J. Electroanal. Chem.* **1994,** *365,* 35-39.

(165) Fortier G.; Brassard E.; Belanger D. "Optimisation of a polypyrrole glucose oxidase biosensor". *Biosensors & Bioelectronics* **1990,** *5,* 473-490.

(166) Gros P.; Bergel A. "Improved model of a polypyrrole glucose-oxidase modified electrode". *J. Electroanal. Chem.* **1995,** *386,* 65-73.

(167) Allara D. L. "A summary of critical issues for application of IR spectroscopy to characterization of surface processing". *Critical Reviews in Surface Chemistry* **1993,** *2,* 1.2, 91-110.

(168) Pei Q.; Qian R. "Electrochemical polymerization of pyrrole in aqueous buffer solutions". *J. Electroanal. Chem.* **1992,** *322,* 153-166.

(169) Asavapiriyanont S.; Chandler G. K.; Gunawardena G. A.; Pletcher D. "The electrodeposition of polypyrrole films from aqueous solutions". *J. Electroanal. Chem.* **1984,** *177,* 229-244.

(170) Wilson R.; Turner A. P. F. "Glucose oxidase: an ideal enzyme". *Biosensors & Bioelectronics* **1992,** *7,* 165-185.

(171) Pfluger P.; Krounbi M.; Street G. B.; Weiser G. "The chemical and physical properties of pyrrole-based conducting polymers: The oxidation of neutral polypyrrole". *J.Chem.Phys.* **1983,** *78,* 3212-3218.

(172) Frommer J. "Scanning tunnelling microscopy and atomic force microscopy in organic chemistry". *Angew. Chem. Int. Ed. Engl.* **1992,** *31,* 1298-1328.

(173) Belanger D.; Nadreau J.; Fortier G. "Electrochemistry of the polypyrrole glucose oxidase electrode". *J. Electroanal. Chem.* **1989,** *274,* 143-155.

(174) Ramanathan K.; Sundaresan N. S.; Malhotra B. D. "Ion-exchanged polypyrrole-based glucose biosensor - enhanced loading and response". *Electroanalysis* **1995,** *7,* 579-582.

(175) Rishpon J.; Gottesfeld S. "Investigation of polypyrrole glucose-oxidase electrodes by ellipsometric, microgravimetric and electrochemical measurements". *Biosensors & Bioelectronics* **1991,** *6,* 143-149.

(176) Cui C. Q.; Ong L. H.; Tan T. C.; Lee J. Y. "Origin of the difference between potentiostatic and cyclic potential sweep depositions of polyaniline". *J. Electroanal. Chem.* **1993,** *346,* 477-482.

(177) Sabatani E.; Redondo A.; Rishpon J.; Rudge A.; Rubinstein I.; Gottesfeld S. "Morphology control in electrochemically grown conducting polymer films .2. Effects of cathodic bias on anodically grown films studied by spectroscopic ellipsometry and quartz-crystal microbalance". *J. Chem. Soc. , Faraday Trans. 1* **1993,** *89,* 287-294.

(178) Yabuki S.; Shinohara H.; Aizawa M. "Electro-conductive enzyme membrane". *J. Chem. Soc. , Chem. Commun.* **1989,** 945-946.

(179) Rishpon J.; Gottesfeld S.; Campbell C.; Davey J.; Zawodzinski T. A. "Amperometric glucose sensors based on glucose-oxidase immobilized in nafion". *Electroanalysis* **1994,** *6,* 17-21.

(180) Wang J.; Liu J.; Chen L.; Lu F. "Highly selective membrane-free, mediator-free glucose biosensor". *Anal. Chem.* **1994,** *66,* 3600-3603.

(181) Centonze D.; Guerrieri A.; Malitesta F.; Palmisano F.; Zambonin P. G. "Interference-free glucose sensor based on glucose-oxidase immobilized in an overoxidised non-conducting polypyrrole film". *Fresenius J.Anal Chem.* **1992,** *342,* 729-733.

(182) Christensen P. A.; Hamnett A. "In situ spectroscopic investigations of the growth, electrochemical cycling and overoxidation of polypyrrole in aqueous solution". *Electrochimica Acta* **1991,** *36,* 1263-1286.

(183) Palmisano F.; Malitesta C.; Centonze D.; Zambonin P. G. "Correlation between permselectivity and chemical structure of overoxidized polypyrrole membranes used in electroproduced enzyme biosensors". *Anal. Chem.* **1995,** *67,* 2207-2211.

(184) Palmisano F.; Guerrieri A.; Quinto M.; Zambonin P. G. "Electrosynthesized bilayer polymeric membrane for effective elimination of electroactive interferents in amperometric biosensors". *Anal. Chem.* **1995,** *67,* 1005-1009.

(185) Witkowski A.; Freund M. S.; Brajtertoth A. "Effect of electrode substrate on the morphology and selectivity of overoxidized polypyrrole films". *Anal. Chem.* **1991,** *63,* 622-626.

(186) Chang R. "Physical chemistry with applications to biological systems", Macmillan Publishing Co., Inc. New York, 1981.

(187) Subirade M.; Lebugle A. "Organization of a globular protein film on solid-surfaces: an X-ray photoelectron-spectroscopy study". *Thin Solid Films* **1994,** *243,* 442-445.

(188) Fitzpatrick H.; Luckham P. F.; Eriksen S.; Hammond K. "Use of X-ray photoelectron spectroscopy to study protein adsorption to mica surfaces". *J.Colloid Interface Sci.* **1992,** *149,* 1-9.

(189) Clark D. T.; Peeling J.; Colling L. "An experimental and theoretical investigation of the core level spectra of a series of amino acids, dipeptides and polypeptides". *Biochim. Biophys. Acta* **1976,** *507,* 533-545.

(190) De Benedetto G. E.; Malitesta C.; Zambonin C. G. "Electroanalytical/X-ray photoelectron spectroscopy investigation on glucose oxidase adsorbed on platinum". *J. Chem. Soc. , Faraday Trans. 1* **1994,** *90,* 11, 1495-1499.

(191) Ratner B. D. "Advances in the analysis of surfaces of biomedical interest". *Surf.Interface Anal.* **1995,** *23,* 521-528.

(192) Beamson G.; Briggs D.; Davies S. F.; Fletcher I. W.; Clark D. T.; Howard J.; Gelius U.; Wannberg B.; Balzer P. "Performance and application of the Scienta ESCA300 spectrometer". *Surf.Interface Anal.* **1990,** *15,* 541-549.

(193) Ghosh P. K. "Introduction to photoelectron spectroscopy", Wiley: New York, 1983.

(194) Schlenoff J. B.; Xu H. "Evolution of physical and electrochemical properties of polypyrrole during extended oxidation". *J.Electrochem.Soc.* **1992,** *139,* 2397-2401.

(195) Witkowski A.; Brajtertoth A. "Overoxidized polypyrrole films: A model for the design of permselective electrodes". *Anal. Chem.* **1992,** *64,* 635-641.

(196) Chesher D. A.; Christensen P. A.; Hamnett A. "Anion movement and carrier type in polypyrrole/dodecyl-sulfate". *J. Chem. Soc. , Faraday Trans. 1* **1993,** *89,* 303-309.

(197) Moulder J. F.; Stickle W. F.; Sobol P. E.; Bomben K. D. "Handbook of X-ray photoelectron spectroscopy", Perkin Elmer Corp. Eden Praire, 1992.

(198) Pfluger P.; Street G. B. "Chemical, electronic, and structural properties of conducting heterocyclic polymers: A view by XPS". *J.Chem.Phys.* **1984,** *80,* 544-553.

(199) Hecht H. J.; Kalisz H. M.; Hendle J.; Schmid R. D.; Schomburg D. "Crystal structure of Glucose Oxidase from *Aspergillus Niger* refined at 2.3 Angstrom resolution". *J.Mol.Biol.* **1993,** *229,* 153-172.

(200) Szucs A.; Hitchens G. D.; Bockris J. O. "On the adsorption of Glucose Oxidase at a gold electrode". *J.Electrochem.Soc.* **1989,** *136,* 3748-3755.

(201) Hayden B. E. "Vibrational spectroscopy of molecules on surfaces", Plenum Press: New York, 1987.

(202) Haris P. I.; Chapman D. "Does Fourier-transform infrared spectroscopy provide useful information on protein structures?". *TIBS* **1992,** *17,* 328-333.

(203) Susi H.; Byler D. M. "Resolution enhanced Fourier transform infrared spectroscopy of enzymes". *Methods Enzymol.* **1986,** *130,* 290-311.

(204) Singh B. R.; Fuller M. P. "FT-IR in combination with the attenuated total reflectance technique: A very sensitive method for the structural analysis of polypeptides". *Appl. Spectrosc.* **1991,** *45,* 1017-1021.

(205) Fiol C.; Alexandre S.; Dubreuil N.; Valleton J. M. "Characterization of behenic acid/glucose-oxidase Langmuir-Blodgett films by spectrophotometry: a tentative model of their organization". *Thin Solid Films* **1995,** *261,* 287-295.

(206) Porter M. D. "IR external reflection spectroscopy: A probe for chemically modified surfaces". *Anal. Chem.* **1988,** *60,* 20, 1143A-1155A.

(207) Surewicz W. K.; Mantsch H. H. "New insight into protein secondary structure from resolution-enhanced infrared spectra". *Biochim. Biophys. Acta* **1988,** *952,* 115-130.

(208) Williams R. W. "Protein secondary structure-analysis using Raman amide I and amide III spectra". *Methods Enzymol.* **1986,** *130,* 311-331.

(209) Fu F. N.; Deoliveira D. B.; Trumble W. R.; Sarkar H. K.; Singh B. R. "Secondary structure estimation of proteins using the amide III region of Fourier transform infrared spectroscopy: Application to analyse calcium binding induced structural changes in calsequestrin". *Appl. Spectrosc.* **1994,** *48,* 1432-1441.

(210) Jeon J. S.; Sperline R. P.; Raghavan S. "Quantitative analysis of adsorbed serum albumin on segmented polyurethane using FT-IR/ATR spectroscopy". *Appl. Spectrosc.* **1992,** *46,* 1644-1648.

(211) Schubert M. A.; Wiggins M. J.; Schaefer M. P.; Hiltner A.; Anderson J. M. "Oxidative biodegradation mechanisms of biaxially strained poly(etherurethane urea) elastomers". *J.Biomed.Mater.Res.* **1995,** *29,* 337-347.

(212) Rabolt J. F.; Jurich M.; Swalen J. D. "Infrared reflection-absorption studies of thin-films at grazing-incidence". *Appl. Spectrosc.* **1985,** *39,* 269-272.

(213) Brendel R. "Quantitative infrared study of ultrathin MIS sturctures by grazing internal reflection". *Appl. Phys. A* **1990,** *50,* 587-593.

(214) Singh B. R.; Fuller M. P.; Dasgupta B. R. "Botulinum neurotoxin type A: Structure and interaction with the micellar concentration of SDS determined by FT-IR spectroscopy". *J.Protein Chem.* **1991,** *10,* 637-649.

(215) Shimidzu T.; Ohtani A.; Iyoda T.; Honda K. "Charge-controllable polypyrrole/polyelectrolyte composite membranes .2. Effect of incorporated anion size on the electrochemical oxidation-reduction process". *J. Electroanal. Chem.* **1987,** *224,* 123-135.

(216) Willicut R. J.; Mccarley R. L. "Surface-confined monomers on electrode surface 1. Electrochemical and microscopic characterization of omega-(n-pyrrolyl)alkanethiol self-assembled monolayers on Au". *Langmuir* **1995,** *11,* 296-301.

(217) Reffner J. A.; Wihlborg W. T. "Microanalysis by reflectance FTIR microscopy". *International Laboratory* **1990,** *July/August,* 19-26.

(218) Moussy F.; Harrison D. J. "Prevention of he rapid degradation ofsubcutaneously implanted Ag/AgCl reference electrodes using polymer coatings". *Anal. Chem.* **1994**, *66*, 674-679.

(219) Csoregi E.; Schmidtke D. W.; Heller A. "Design and optimization of a selective subcutaneously implantable glucose electrode based on "wired" glucose-oxidase". *Anal. Chem.* **1995,** *67,* 1240-1244.

(220) Hober R. "Messungen der inneren Leitfahigkeit von Zellen". *Pfl Physiol Archiv Mensch Tiere* **1913,** *150,* 15-45.

(221) Fricke H. "The electric capacity of suspensions of red corpuscels of a dog". *Phys Rev* **1925,** *26,* 682-687.

(222) Kakutani T.; Shibatani S.; Senda M. "Electrorotation of barley mesophyll protoplasts". *Bioelectrochem. Bioenerg.* **1993,** *31,* 85-97.

(223) Huang Y.; Wang X. B.; Holzel R.; Becker F. F.; Gascoyne P. R. C. "Electrorotational studies of the cytoplasmic dielectric-properties of friend murine erythroleukemia-cells". *Phys. Med. Biol.* **1995,** *40,* 1789-1806.

(224) Porter M. D. "IR external reflection spectroscopy: A probe for chemically modified surfaces". *Anal. Chem.* **1988,** *60,* 20, 1143A-1155A.

List of Abbreviations

AFM	Atomic Force Microscopy
ATR	Attenuated Total Reflection
BAS	Bioanalytical Instruments Inc.
BHK	Baby Hamster Kidney
CVD	Chemical Vapour Deposition
DMSO	Dimethyl Sulfoxide
DTSSP	3,3'-Dithiobis (sulfosuccinimidylpropionate)
e-beam	Electron-Beam
EDC	1-ethyl-3-(3-dimethylaminopropyl) carbodiimide
FAD	Flavin Adenine Dinucleotide
FMLP	Formyl Methionine [F-Met-Leu-Phe]
FTIR	Fourier Transform Infra-Red Spectroscopy
GIR	Grazing Incident Reflectance
GOx	Glucose Oxidase
HP	Hewlett Packard
IPA	Isopropyl Alcohol
IR	Infra Red
MCT	Mercury Cadmium Telluride
MIBK	Methyl Isobutyl Ketone
MPS	[3-Mercaptopropyl] trimethoxysilane
NAC	N-Acetyl Cysteine
PBS	Phosphate Buffered Saline
PECVD	Plasma Enhanced Chemical Vapour Deposition
PMA	Phorbol 12-Myrisitate 13-Acetate
PMMA	Poly(methyl methacrylate)
PPy	Polypyrrole
PPy+	Oxidised Polypyrrole
PPy-oox	Polypyrrole - Over-oxidised
RIE	Reactive Ion Etch
RO	Reverse Osmosis
ROS	Reactive Oxygen Species
RUSTI	Research Unit for Surface Transforms and Interfaces
sccm	Standard Cubic Centimeters per Minute
SNR	Signal to Noise Ratio
SOD	Superoxide Dismutase
TOA	Take-Off Angle
TWD	Travelling-Wave Dielectrophoresis
XOx	Xanthine Oxidase
XPS	X-ray Photoelectron Spectroscopy

GLASGOW UNIVERSITY LIBRARY